Title
Computational Methods in Slender Structures and Soft Robots

Permalink
https://escholarship.org/uc/item/9tt232hr

Author
Huang, Weicheng

Publication Date
2021

Peer reviewed|Thesis/dissertation

UNIVERSITY OF CALIFORNIA
Los Angeles

Computational Methods in Slender Structures and Soft Robots

A dissertation submitted in partial satisfaction
of the requirements for the degree
Doctor of Philosophy in Mechanical Engineering

by

Weicheng Huang

2021

2021

ABSTRACT OF THE DISSERTATION

Computational Methods in Slender Structures and Soft Robots

by

Weicheng Huang
Doctor of Philosophy in Mechanical Engineering
University of California, Los Angeles, 2021
Professor Mohammed Khalid Jawed, Chair

Slender structures, existing in both natural environments (tendrils) and man-made systems (soft robots), often undergo geometrically nonlinear deformations and dramatic topological changes when subjected to simple boundary conditions or moderate external actuations, which pose extensive challenges to the traditional numerical and analytical methods. This dissertation focuses on the Discrete Differential Geometry (DDG)-based numerical frameworks for simulating the mechanical response in slender structures and soft robots, and makes four major contributions:

First, we use a planar rod theory and incorporate Coulomb frictional contact, elastic/inelastic collision with ground, and inertial effects in a physically accurate manner, to simulate the dynamics of shape memory alloy (SMA)-powered soft robots. Our simulations show quantitative agreement when compared against with experiments, suggesting that our numerical approach represents a promising step toward the ultimate goal of a computational framework for soft robotic engineering. We then combine the same planar rod framework with a naive fluid-structure interaction model to perform the swimming of a seastar-inspired soft robot in water.

Secondly, we numerically explore the propulsion of bacteria flagella in a low Reynolds fluid. We study the locomotion of a bacteria-inspired soft robot. Our numerical framework uses (i) Discrete Elastic Rods (DER) method to account for the elasticity of soft filament, (ii) Lighthill's Slender Body Theory (LSBT) for the long term hydrodynamic flow by helical flagellum, and (iii) Higdon's model for the hydrodynamics from spherical head. A data-driven approach is later employed to develop a control algorithm such that our flagella-inspired robot can follow a prescribed trajectory only by changing its rotation frequency. Then, to investigate the bundling behavior between two soft helical rods rotating side by side in a viscous fluid, we implement a coupled DER and Regularized Stokeslet Segment (RSS) framework. The contact between two rods is also considered in our numerical tool. A novel bundling behavior between two nearby helical rods is uncovered, whereby the filaments come across each other above a critical angular velocity.

Our third contribution is to present a numerical method for both forward physics-based simulations and inverse form-finding problems in elastic gridshells. Our numerical framework on elastic gridshell first decomposes this special structure into multiple one dimensional rods and linkers, which can be performed by the well-established Discrete Elastic Rods (DER) algorithm. A stiffed spring between rods and linkages is later introduced to ensure the bending and twisting coupling at joint area. The inverse form finding problem – compute the initial planar pattern from a given 3D configuration – is directly solved by a contact-based procedure, without using any the conventional optimization-based algorithms. Several examples are used to show the effectiveness of the inverse design process.

Finally, we compare Kirchhoff rod model, Sadowsky ribbon model, and Föppl-von Kármán plate equations, to systematically characterize a group of slender structures, from narrow strip to wide plate. We consider a pre-buckled band under lateral end translation and quantity its supercritical pitchfork bifurcation. The one dimensional anisotropic rod can give a reasonable prediction when the strip is narrow, while fails to capture its width effect. A two dimensional plate approach, on the other hand, accurately anticipates the nonlinear deformations and the critical supercritical pitchfork points for both narrow and wide plates. We finally discuss in detail the issues of traditional one dimensional ribbon models at the inflection points, and then use an extensible ribbon model to bridge the gap between the Kirchhoff rod model and the classical Sadowsky ribbon model.

The dissertation of Weicheng Huang is approved.

Vinay Kumar Goyal

Jeffrey D Eldredge

Veronica Santos

Lihua Jin

Mohammed Khalid Jawed, Committee Chair

University of California, Los Angeles

2021

TABLE OF CONTENTS

LIST OF FIGURES

ACKNOWLEDGMENTS

First and foremost, I would like to bring my heartiest gratitude to my PhD advisor and mentor, Professor Mohammed Khalid Jawed, for his support throughout my research career. His guidance is always helpful and inspiring. Without his help and encouragement, this dissertation could not have been finished.

I next want to thank my committee members, Professor Lihua Jin, Professor Veronica Santos, Professor Vinay Kumar Goyal, and Professor Jeffrey D Eldredge, for their advice during my study and research.

I also want to thank Dr. Xiaonan Huang, Professor Carmel Majidi, Dr. Mojtaba Forghani, Professor Basile Audoly, Dr. Andy Borum, Dr. Changyeob Baek, Dr. Tian Yu, and all the members in SCI Lab, for their continued supports.

Last but not least, I would like to offer my special thanks to my families and friends, for their unconditional love, deep care, constant supports, and tremendous understandings.

VITA

2013–2017 B. Eng. in Engineering Mechanics, Tongji University, China.

PUBLICATIONS

[1] **Weicheng Huang** and Mohammed Khalid Jawed. "Newmark-Beta Method in Discrete Elastic Rods Algorithm to Avoid Energy Dissipation." *Journal of Applied Mechanics*.

[2] **Weicheng Huang** and Mohammed Khalid Jawed. "Numerical Exploration on Buckling Instability for Directional Control in Flagellar Propulsion." *Soft Matter*.

[3] **Weicheng Huang**[1], Xuanhe Li[1], and Mohammed Khalid Jawed. "A Discrete Differential Geometry-based Approach to Numerical Simulation of Timoshenko Beam." *Extreme Mechanics Letters*.

[4] **Weicheng Huang**[1], Xiaonan Huang[1], Carmel Majidi, and Mohammed Khalid Jawed. "Dynamic Simulation of Articulated Soft Robots." *Nature communications*.

[5] **Weicheng Huang**[1], Xuanhe Li[1], and Mohammed Khalid Jawed. "Discrete Elasto-Plastic Rods." *Extreme Mechanics Letters*.

[6] **Weicheng Huang**[1], Longhui Qin[1], Yayun Du, Luocheng Zheng, and Mohammed Khalid Jawed. "Genetic Algorithm-based Inverse Design of Elastic Gridshells." *Structural and Multidisciplinary Optimization*.

[7] **Weicheng Huang**, Yunbo Wang, Xuanhe Li, and Mohammed Khalid Jawed. “Shear Induced Supercritical Pitchfork Bifurcation of Pre-buckled Bands, from Narrow Strips to Wide Plates.” *Journal of the Mechanics and Physics of Solids*.

[8] **Weicheng Huang**, Zachary Patterson, Carmel Majidi, and Mohammed Khalid Jawed. “Modeling Soft Swimming Robots using Discrete Elastic Rod Method.” *Bioinspired Sensing, Actuation, and Control in Underwater Soft Robotic Systems.* Springer, Cham.

[9] **Weicheng Huang**[1], Longhui Qin[1], and Mohammed Khalid Jawed. “Numerical Method for Direct Solution to Form-finding Problem in Convex Gridshell.” *Journal of Applied Mechanics*.

[10] **Weicheng Huang**[1], Xiaonan Huang[1], Zachary Patterson[1], Zhijian Ren, Mohammed Khalid Jawed, and Carmel Majidi. “Numerical Simulation of an Untethered Omni-Directional Star-Shaped Swimming Robot.” *2021 IEEE International Conference on Robotics and Automation (ICRA)*.

[11] Mojtaba Forghani, **Weicheng Huang**, and Mohammed Khalid Jawed. “Control of Uniflagellar Soft Robots at Low Reynolds Number using Buckling Instability.” *Journal of Dynamic Systems, Measurement, and Control*.

[12] **Weicheng Huang** and Mohammed Khalid Jawed. “Numerical Simulation of Bundling of Helical Elastic Rods in a Viscous Fluid.” Under review.

CHAPTER 1

Introduction

Thin elastic structures are three dimensional objects with at least one dimension much larger than the others, e.g., one dimensional rods (length $\gg$ width $\sim$ thickness) and two dimensional plates (length $\sim$ width $\gg$ thickness) [1]. Due to their special geometric properties, these structures usually undergo geometrically nonlinear deformations when subjected to moderate external actuations or simple boundary conditions. Also, the mechanical instabilities in those objects often lead to functionality rather than failure [2], which brings them to numerous attentions and applications in biophysics and engineering science, such as bacterial locomotion [3], metamaterials [4], and robotic systems [5], and as a result, raising the need for a comprehensive numerical framework to predict their complex mechanical behaviors.

Some man-made systems, e.g., soft robots, are composed of deformable slender materials, such that they can achieve mechanically robust maneuvers that are not typically possible with conventional rigid robotic systems [6]. However, to realize the full potential of soft robots and achieve the ultimate goal of autonomous locomotion through challenging environments, it is necessary to develop a robust, accurate, and real-time computational framework. Previous efforts to simulate soft robots have focused on Finite Element Method [7] and voxel-based discretization [8]. Thanks to the slenderness in those man-made systems, we propose a 1D rod-based numerical framework to simulate the soft robotic dynamics by considering the geometrically nonlinear elasticity, inertia, viscoelastic behavior, and frictional contact with ground. This framework is later incorporated with a naive fluid-structure interaction model to study the underwater behavior of a star-shaped soft robot.

Rod-like structures also existing in some natural environments, e.g., bacteria usually rely on their helical flagellar for locomotion in a low Reynolds environment [9]. This leads to a complex interaction between the geometrically nonlinear deformation in the soft flagellum and the hydrodynamics from the low Reynolds flow, such as tumbling [10], turning [11], and bundling [12]. Recently, there has been significant progress in understanding flagellar propulsion – particularly from a single flagellum – through experiments [11], computation [13], and theory [14]. The models used for this fluid-structure interaction problem are: Resistive Force Theory (RFT) [15], Lighthill's Slender Body Theory (LSBT) [15], and Regularized Stokeslet Segments (RSS) method [16] We use DER-LSBT framework to show that bacteria can exploit buckling in flagellum to precisely control their swimming direction, and then consider DER-RSS theory to perform the bundling behavior between multiple filaments.

The fundamental mechanics of thin structures is another key component of this thesis. The elastic gridshells that described by a two dimensional surface but comprised of multiple one dimensional rods are of interests. An initially two dimensional grid of elastic rods may be actuated into a three dimensional shell-like structure through buckling instability when its footprints are constrained to a shrinking boundary [17]. Moreover, the mechanical response of this hollow surface usually perform the nonlocal property [18], which is totally different from the localization phenomenon in a continuum shell model. We program a novel numerical tool to study both forward mechanical response and inverse form-finding problem for this special grid-like object. On the other hand, in contrast to the traditional rod model (length $\gg$ width $\sim$ thickness) and plate model (length $\sim$ width $\gg$ thickness), ribbon is an elastic structure whose three dimensions are all very different (length $\gg$ width $\gg$ thickness), such that the elastic ribbons lie halfway between the 1D case of thin rods and the 2D case of thin elastic plates [19]. Various models and theories have been developed to study the complex mechanical responses in thin elastic structures, such as Kirchhoff rod model [20], Sadowsky ribbon model[21], Wunderlich ribbon model[22], and Föppl-von Kármán plate equations [23, 24]. We combine three different models: Kirchhoff rod model, Sadowsky ribbon model, and Föppl-von Kármán

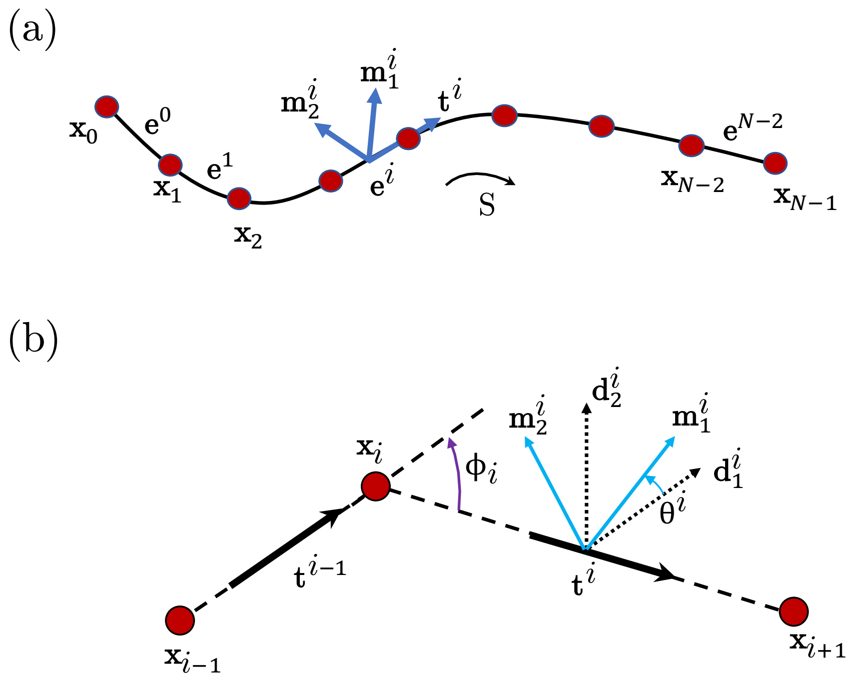

Figure 1.1: (a) Discrete schematic diagram of a rod. (b) Notations used in our discrete model.

plate equations, and desktop experiments, to study the supercritical pitchfork bifurcation of a pre-buckled strip.

1.1 Numerical Method: Discrete Elastic Rods

Rod theory can date back to 18th century, during which Euler and Bernoulli proposed a simple one dimensional beam model [25]. Their work was later generalized by Kirchhoff and Cosserat in 19th century [20, 26]. Recently, researchers in computer graphics community developed a fast numerical framework – Discrete Elastic Rods method – to perform the nonlinear dynamics of elastic rods [27, 28]. Here, we briefly review the core formulation of this physically-based simulation for one dimensional objects.

A continuous rod is discretized into N nodes: $\mathbf{x}_0, ..., \mathbf{x}_{N-1}$, which correspond to $N-1$ edge vectors: $\mathbf{e}^0, ..., \mathbf{e}^{N-2}$ such that $\mathbf{e}^i = \mathbf{x}_{i+1} - \mathbf{x}_i$ and $i = 0, \ldots, N-2.$, shown schematically in Fig. 1.1(a). Hereafter, we use subscripts to denote quantities associated with the nodes, e.g., $\mathbf{x}_i$, and superscripts when associated with edges, e.g., $\mathbf{e}^i$. Each edge, $\mathbf{e}^i$, has an orthonormal adapted reference frame $\{\mathbf{d}_1^i, \mathbf{d}_2^i, \mathbf{t}^i\}$ and a material frame $\{\mathbf{m}_1^i, \mathbf{m}_2^i, \mathbf{t}^i\}$; both the frames share the tangent $\mathbf{t}^i = \mathbf{e}^i/|\mathbf{e}^i|$ as one of the directors. The reference frame is updated at each time step through parallel transport in time, and, referring to Fig. 1.1(b), the material frame can be obtained from a scalar twist angle θ^i. See Ref. [29] for a detailed exposition of the DER algorithm. Node positions together with twist angles constitute the $4N-1$ sized degrees of freedom (DOF) vector, $\mathbf{q} = \left[\mathbf{x}_0, \theta^0, \mathbf{x}_1, ..., \mathbf{x}_{N-2}, \theta^{N-2}, \mathbf{x}_{N-1}\right]$, of the discrete rod. Based on this kinematic representation, in the remainder of this section, we discuss the formulation of elastic energies, elastic forces, and the time stepping procedure of the rod solver.

An elastic rod is modeled as a mass-spring system, with a lumped mass (and angular mass) at each node (and edge), and associated discrete stretching, bending, and twisting energies. For a rod with Young's modulus E, shear modulus G, and isotropic circular cross section, the elastic energies – stretching, bending, and twisting – are given by [27, 28]

$$E_s = \frac{1}{2}\sum_{i=0}^{N-2} EA(\epsilon^i)^2|\bar{\mathbf{e}}^i| \tag{1.1a}$$

$$E_b = \frac{1}{2}\sum_{i=0}^{N-1} \frac{EI}{\Delta l_i}\left[(\kappa_i^{(1)} - \bar{\kappa}_i^{(1)})^2 + (\kappa_i^{(2)} - \bar{\kappa}_i^{(2)})^2\right] \tag{1.1b}$$

$$E_t = \frac{1}{2}\sum_{i=0}^{N-1} \frac{GJ}{\Delta l_i}(\tau_i)^2, \tag{1.1c}$$

where A is the area of cross-section, I is the area moment of inertia, J is the polar moment of inertia, ϵ^i is the stretching strain associated with the i-th edge, $\bar{\mathbf{e}}^i$ is its undeformed length, $\kappa_i^{(1)}$ and $\kappa_i^{(2)}$ are the bending curvatures at the i-th node ($\bar{\kappa}_i^{(1)}$ and $\bar{\kappa}_i^{(2)}$ are the curvatures in the undeformed configuration), τ_i is the twist at the i-th node, and $\Delta l_i = \left(|\mathbf{e}^i| + |\mathbf{e}^{i+1}|\right)/2$ is its Voronoi length. The strain measures, i.e., ϵ^i, $\kappa_i^{(1)}$, $\kappa_i^{(2)}$, and τ_i, can be expressed in terms of $\mathbf{q}$ (specifically, $\mathbf{x}_{i-1}, \theta^{i-1}, \mathbf{x}_i, \theta^i, \mathbf{x}_{i+1}$). The case of non-circular cross-section can be included in the above formulation with minor changes [27, 28].

At each degree of freedom q_j, the elastic forces (associated with nodal positions) and elastic moments (associated with the twist angles) are

$$F_j^{\text{int}} = -\frac{\partial}{\partial q_j}\left(E_s + E_b + E_t\right), \tag{1.2}$$

where j is an integer between 0 to $4N-2$.

Implicit Euler integration is used to solve the following $4N-1$ equation of motions and update the DOF vector $\mathbf{q}$ and its velocity (time derivative of DOF) $\mathbf{v} = \dot{\mathbf{q}}$ from time step t_k to $t_{k+1} = t_k + h$ (h is the time step size):

$$\mathbf{M}\Delta\mathbf{q}_{k+1} - h\mathbf{M}\mathbf{v}_k - h^2\left(\mathbf{F}^{\text{int}}_{k+1} + \mathbf{F}^{\text{ext}}_{k+1}\right) = \mathbf{0} \tag{1.3a}$$

$$\mathbf{q}_{k+1} = \mathbf{q}_k + \Delta\mathbf{q}_{k+1} \tag{1.3b}$$

$$\mathbf{v}_{k+1} = \frac{1}{h}\Delta\mathbf{q}_{k+1}, \tag{1.3c}$$

where $\mathbf{F}^{\text{ext}}$ is the external force vector (e.g., gravity and damping force), $\mathbf{M}$ is the diagonal mass matrix comprised of the lumped masses, and $\dot{()}$ represents derivative with respect to time. The superscript $k+1$ (and k) denotes evaluation of the quantity at time t_{k+1} (and t_k). Newton's method is used to iteratively solve the $4N-1$ sized equation of motions.

In summary, DER is formulated based on the classical Kirchhoff theory, e.g., the elastic energies are given by the curvatures of rod centerline, and the internal elastic forces required by equations of motion are derived from the energies in a discrete format. Our researches start from the well-established DER simulation and move forward: in Ch. 2, we discuss the difference between the first order Euler method and the second order Newmark-beta Method in a dynamic rod system; in Ch. 3, we use rod simulation, with the consideration of frictional contact and collision with ground, to perform the dynamics of a star-shaped soft rolling robot; in Ch. 4, a naive hydrodynamic force is incorporated with rod simulation to simulate the swimming of soft underwater robot; in Ch. 5, we employ Lighthill's Slender Body Theory (LSBT) to formulate the external forces experienced by a flagella-inspired soft robot moving in a viscous fluid; in Ch. 6, we replace LSBT by Regularized Stokeslet Segments (RSS) method, with the consideration of contact between multiple filaments, to simulate the bundling behavior of two elastic helical rods rotating side by side in a low Reynolds environment; in Ch. 7, we investigate the structure comprised of multiple rods and propose a contact-based method to solve the inverse form-finding problem in elastic gridshells; finally, in Ch. 8, we combine Kirchhoff rod theory, Sadowsky ribbon model, and Föppl-von Kármán (FvK) plate framework, to systematically study the mechanics of thin bands.

1.2 Outline of the Thesis

This chapter introduces the well-established numerical tool for simulating the mechanics of rods that serve as a foundation for this Thesis. Subsequent chapters present some extensions of DER method for the investigations of the dynamics in soft robots and the mechanics in slender structures. The primary contributions of this thesis are as follows:

Ch. 2 studies the time integration process in DER algorithm. Traditional DER method using a first order implicit Euler method for time integration would suffer from artificial energy loss; we consider a second order symplectic Newmark-beta integration to overcome this numerical issue. The modified approach shows better convergence with time step size when damping force is trivial in a dynamic system, which is an essential step to perform the dynamics in soft robots, as the inertia of which is predominant.

Ch. 3 investigates the dynamics of soft rolling robot. We incorporates an implicit treatment of the elasticity of limbs, elastic/inelastic collision between a soft body and rigid surface, and unilateral contact and Coulombic friction with an uneven surface, to simulate a shape memory alloy (SMA)-powered soft robot. The computational efficiency of the numerical method enables it to run faster than real-time on a desktop processor, which makes it ideally suited for algorithms that iterate over a wide variety of parameters in order to select a robot design or locomotion strategy. Together with the soft rolling robot, a jumper robot and a rolling ribbon are also performed to validate the correctness of our numerical framework.

Ch. 4 studies the swimming of a soft underwater robot. We again start with a nonlinear rod theory, model the drag force as an external force in the discrete simulation, to mimetic a star-shaped soft robot swimming in a liquid environment. This numerical framework can still run faster than real-time on a single thread of a desktop processor. This framework can potentially be used for the optimized design and trajectory control for the soft underwater robots.

Ch. 5 considers a control strategy for a bacteria-inspired soft robot. We use the DER algorithm to capture the geometrically nonlinear deformation in the flagellum, LSBT to simulate the hydrodynamics, and Higdon's model for the spherical head in motion within a viscous fluid, to build a dynamic model of a flagella-inspired robot. The flagellated system follows a straight path if the angular velocity of the flagellum is below a critical threshold, while buckling ensues in the flagellum beyond this threshold angular velocity and the system takes a nonlinear trajectory. We consider the angular velocity as the control parameter and solve the inverse problem of computing the angular velocity, that varies with time, given a desired nonlinear trajectory, by a data-driven approach. Our results indicate that bacteria can exploit buckling in flagellum to precisely control their swimming direction.

Ch. 6 replaces the LSBT model by Regularized Stokeslet Segments (RSS) theory to perform the bundling behavior between multiple helical rods rotating side by side in a low Reynolds fluid. The non-penetration contact between two rod segments are also included into the numerical tool. In contrast with LSBT, RSS treats the local term and nonlocal term as ones to avoid numerical difficulties when two rod segments becomes closer and get into physical contact. We found that two helical rods rotating side by side can attract each other and become closer because of their hydrodynamic interplay in a viscous fluid, and depending on their initial distance and rotational frequency, the two filaments can come in physical contact. This finding may shed light on the physics of the bio-locomotion of microorganisms and inspire the design of novel biomimetic soft robots.

Ch. 7 analyzes the mechanics of elastic gridshell. Elastic gridshell is a class of net-like structures formed by an ensemble of elastically deforming rods coupled through joints. We use a special geometric decomposition and several constraints to simulate the mechanics of elastic gridshell through the well-established DER method. For the inverse problem associated with form-finding process (3D to 2D), we introduce a contact-based algorithm between the elastic gridshell and a rigid 3D surface, where the rigid surface describes the target shape of the gridshell upon actuation. This technique removes the need of several forward simulations associated with conventional optimization algorithms and provides a direct solution to the inverse problem. Our results and methodology can instigate future work on buckling induced mechanically guided assembly in physical systems from macro scale to micro scale.

Ch. 8 studies the shear induced supercritical pitchfork bifurcation of pre-buckled bands, from narrow to wide. Together with desktop experiments, we combine three different models – Kirchhoff rod model, Sadowsky ribbon model, and Föppl-von Kármán (FvK) plate model – to systematically investigate a group of thin elastic structures. A pre-compressed elastic strip would experience bifurcation when the transverse shear goes beyond a threshold, and the critical shear is related to the length to width ratio. Both one dimensional rod model and two dimensional plate framework can capture this phenomenon; the strip model with developable constraints, surprisingly, fails to forecast the deformed patterns observed in experiments, and gives a singular prediction at the inflection point. Our study provides guidelines on the choice of the appropriate structural model - rod vs. ribbon vs. plate - in simulation of thin elastic structures.

Finally, in Ch. 9, we summarize all the findings presented in this dissertation thesis.

CHAPTER 2

Newmark-beta Method in Discrete Elastic Rods to Avoid Energy Dissipation

Discrete Elastic Rods (DER) algorithm presents a computationally efficient means of simulating the geometrically nonlinear dynamics of elastic rods. However, it can suffer from artificial energy loss during the time integration step. Our approach extends the existing Discrete Elastic Rods (DER) technique by using a different time integration scheme – we consider a second order, implicit Newmark-beta method to avoid energy dissipation. This treatment shows better convergence with time step size, specially when the damping forces are negligible and the structure undergoes a vibratory motion. Two demonstrations – a cantilever beam and a helical rod hanging under gravity – are used to show the effectiveness of the modified Discrete Elastic Rods simulator.

The underlying motivation is in § 2.1. The time marching step is detailed in § 2.2. Next, we discuss the results and conclusions in § 2.3 and § 2.4. The content of this chapter has appeared in Ref. [30].

2.1 Motivation

Recent activities in the field of discrete differential geometry (DDG) have fueled the development of simple, robust, and efficient tools for physics-based simulations of slender elastic structures in the computer graphics community [31]. The DDG-based simulations begin with a physical model that is discretized from the ground up such that the key geometric structures representing the actual smooth physical system of preserved. One of the important applications of DDG in physics-based modeling is Discrete Elastic Rods (DER) method [27, 28] for capturing the geometrically nonlinear deformation of thin elastic rods, e.g., curly hairs. Their deformations are characterized by stretching, bending, and twisting on the basis of Kirchhoff's rod theory [1]. Stretching and bending are captured by the deformation of a curve called the centerline, while twisting is formulated by the rotation of a material frame associated with each segment on the centerline [27]. Recently, DER has been embraced by the mechanics community and excellent agreement has been found between DER-based simulations and physical experiments [32, 3, 17].

However, the first order Euler integration (implicit on elastic and explicit on external forces) used in original DER algorithm is not physically accurate when simulating structural dynamics in low damping environment, because of the energy dissipation induced by this non-symplectic time integration. This issue was not observed in previous DER-based investigations. Some of these studies focused on static [17] or quasi-static deformations [32] and ignored the inertial dynamics. In other studies, the damping force was predominant and vibratory motions were absent [3]. As a result, the energy loss of Euler integration was negligible. However, when studying the fast dynamic response of slender structures, e.g., shape memory alloy-based actuator in soft robotics engineering [33], inertial dynamics is prominent and the numerical error caused by artificial energy dissipation is no longer acceptable. This inspires us to consider a different time marching technique based on the second order Newmark-beta method to maintain energy conservation [34].

In this chapter, we augment DER simulation by a second order time integration method – Newmark-beta method – to better capture the geometrically nonlinear dynamics of elastic rods. Whereas the previous studies focused on simulating the static/quasi-static deformations and damping-dominated dynamics, here, we focus on structural dynamics where inertia is preponderant and environmental damping is absent. We use two examples – a cantilever beam and a naturally helical rod hanging under gravity – to demonstrate the advancements of this Newmark-beta based DER algorithm over the original formulation.

2.2 Time Marching Step

For a single rod system with degrees of freedom (DOF) vector $\mathbf{q}$, its equations of motion is

$$\mathbf{M}\ddot{\mathbf{q}} = \mathbf{F}^{\text{int}} + \mathbf{F}^{\text{ext}}, \tag{2.1}$$

where $\mathbf{F}^{\text{int}}$ is the internal elastic force, $\mathbf{F}^{\text{ext}}$ is the external force vector (e.g., gravity and damping force), $\mathbf{M}$ is the diagonal mass matrix comprised of the lumped masses, and $\dot{()}$ represents derivative with respect to time. In the discrete time stepping scheme of the original DER method, implicit Euler integration is used to solve the following $4N-1$ equation of motions and update the DOF vector $\mathbf{q}$ and its velocity (time derivative of DOF) $\mathbf{v} = \dot{\mathbf{q}}$ from time step t_k to $t_{k+1} = t_k + h$ (h is the time step size):

$$\mathbf{M}\Delta\mathbf{q}_{k+1} - h\mathbf{M}\mathbf{v}_k - h^2\left(\mathbf{F}^{\text{int}}_{k+1} + \mathbf{F}^{\text{ext}}_{k+1}\right) = \mathbf{0} \tag{2.2a}$$

$$\mathbf{q}_{k+1} = \mathbf{q}_k + \Delta\mathbf{q}_{k+1} \tag{2.2b}$$

$$\mathbf{v}_{k+1} = \frac{1}{h}\Delta\mathbf{q}_{k+1}, \tag{2.2c}$$

where superscript $k+1$ (and k) denotes evaluation of the quantity at time t_{k+1} (and t_k). The Jacobian associated with Eq. (2.2a) is necessary for Newton's iteration and can be expressed as

$$\mathbb{J}_{ij} = m_i\delta_{ij} - h^2\left[-\frac{\partial^2\left(E_s + E_b + E_t\right)}{\partial q_i \partial q_j} + \frac{\partial F^{\text{ext}}_i}{\partial q_j}\right], \tag{2.3}$$

where i and j are integers between 0 to $4N-2$, the mass (or angular mass) associated with the i-th DOF is m_i, the energies (E_s, E_b, E_t) are evaluated at $t = t_{k+1}$, and F^{ext}_i is the i-th element of the vector $\mathbf{F}^{\text{ext}}_{k+1}$. If the gradient of the external force vector ($\partial F^{\text{ext}}_i / \partial q_j$) cannot be analytically evaluated, this term is often neglected, i.e., external forces are treated explicitly. Importantly, the Jacobian $\mathbb{J}$ is a banded matrix and the time complexity of this algorithm is $O(N)$, i.e., the computational time linearly scales with the number of nodes [28]. This computational efficiency has motivated its application in the animation industry (e.g., hair simulation for movies) as well as its adoption in mechanical engineering.

This first order time integration can cause energy dissipation in long-time dynamic simulations, because the time stepping from t_k to t_{k+1} is treated as a constant speed process and the effect of acceleration is partially ignored. Here, we modify the time integrating algorithm by a second order, implicit Newmark-beta update [35] such that

$$\mathbf{M}\Delta\mathbf{q}_{k+1} - h\mathbf{M}\mathbf{v}_k - h^2\beta^2\left(\mathbf{F}_{k+1}^{\text{int}} + \mathbf{F}_{k+1}^{\text{ext}}\right) - h^2\beta(1-\beta)\left(\mathbf{F}_k^{\text{int}} + \mathbf{F}_k^{\text{ext}}\right) = \mathbf{0} \tag{2.4a}$$

$$\mathbf{q}_{k+1} = \mathbf{q}_k + \Delta\mathbf{q}_{k+1} \tag{2.4b}$$

$$\mathbf{v}_{k+1} = \frac{1}{h\beta}\Delta\mathbf{q}_{k+1} - \frac{1-\beta}{\beta}\mathbf{v}_k, \tag{2.4c}$$

where β is a parameter between 0.5 and 1.0. At $\beta = 0.5$, the acceleration of the DOFs at the current time step, $t = t_{k+1}$, is computed based on the mean of applied forces (elastic and external) evaluated at $t = t_k$ and $t = t_{k+1}$. We expect the numerical energy dissipation to disappear at this value of β, as evidenced in the next section. Also note that when $\beta = 1.0$, Eqs. (2.4) reduce to Eqs. (2.2). The Jacobian matrix of Eqs. (2.4) is

$$\mathbb{J}_{ij} = m_i\delta_{ij} - h^2\beta^2\left[-\frac{\partial^2\left(E_s + E_b + E_t\right)}{\partial q_i \partial q_j} + \frac{\partial F_i^{\text{ext}}}{\partial q_j}\right], \tag{2.5}$$

such that Eqs. (2.4) can be solved using Newton's iterations, similar to Eqs. (2.2). The banded nature of the Jacobian matrix as well as the $O(N)$ time complexity are maintained.

2.3 Results

In this section, we compare the original DER algorithm (Euler integration) and the updated method (Newmark-beta update) using two examples. We specifically focus on the energy dissipation and the dependence of the solution on the time step size, h. In the first example shown in Fig. 2.1(a), we consider a cantilever beam hanging under gravity with the following physical parameters: rod length $L = 0.5$m, cross-section radius $r_0 = 0.5$cm, (with moment of inertia $I = \pi r_0^4/4$ and cross sectional area $A = \pi r_0^2$), Young's modulus $E = 0.1$ GPa, shear modulus $G = E/3$ (i.e., incompressible material with Poisson's ratio $\nu = 0.5$), density $\rho = 1273.52\text{kg/m}^3$, and acceleration due to gravity, $g = 9.8$ m/s^2; the density and

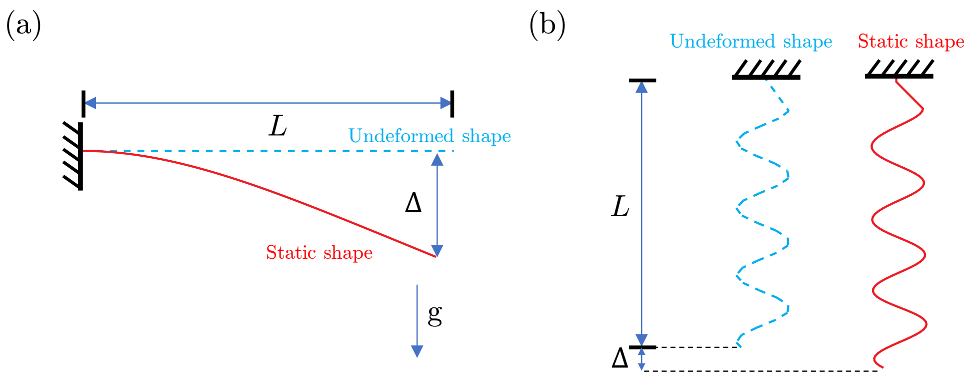

Figure 2.1: Shape of the rod in two demonstrations: (a) cantilever beam and (b) helical rod.

elastic moduli are similar to the experimental rods used in Ref. [32]. Fig. 2.2(a1) shows the normalized tip deflection Δ/L as a function of time using the original DER method (Eqs. (2.2)). The beam undergoes a vibratory motion and the amplitude of the deflection decreases with the time step size h. At $h = 5$ms, the amplitude reduces to one-third of the initial amplitude within 5 seconds. Eventually, the amplitude reduces to zero and the final static configuration has $\Delta/L \approx 0.3$. At smaller values of h, the decay time is larger; nonetheless, after sufficiently long time, the final configuration is static regardless of h and is shown in Fig. 2.1(a) using a solid line. This is a direct result of the energy dissipation caused by the time stepping procedure. Since there is no damping force present in the example, the beam should maintain a pendulum-like periodic motion for infinite time.

In order to remedy this issue, we consider Newmark-beta based modified DER (Eqs. 2.4) in Figs. 2.2 (a2) and (a3) and plot the tip deflection with time. The energy dissipation is reduced at $\beta = 0.75$, and the motion is periodic without noticeable decay in amplitude for $\beta = 0.5$. We verified that the sum of kinetic and potential (elastic and gravitational) energies remains unchanged with time in all the cases considered in Fig. 2.2 (a3). For a direct comparison between the two methods, Fig. 2.2(a4) shows the minimum tip deflection in the first cycle, Δ_m, (i.e., deflection at $t = t_m$ where t_m is shown in Figs. 2.2(a2-a3)) as a function of h. While Δ_m increases almost linearly with h for $\beta = 1$ (used in the original DER method) and $\beta = 0.75$. However, the amount of dissipation is reduced by changing β from 1.0 to 0.75. When $\beta = 0.5$, the modified method shows no dependence on h as

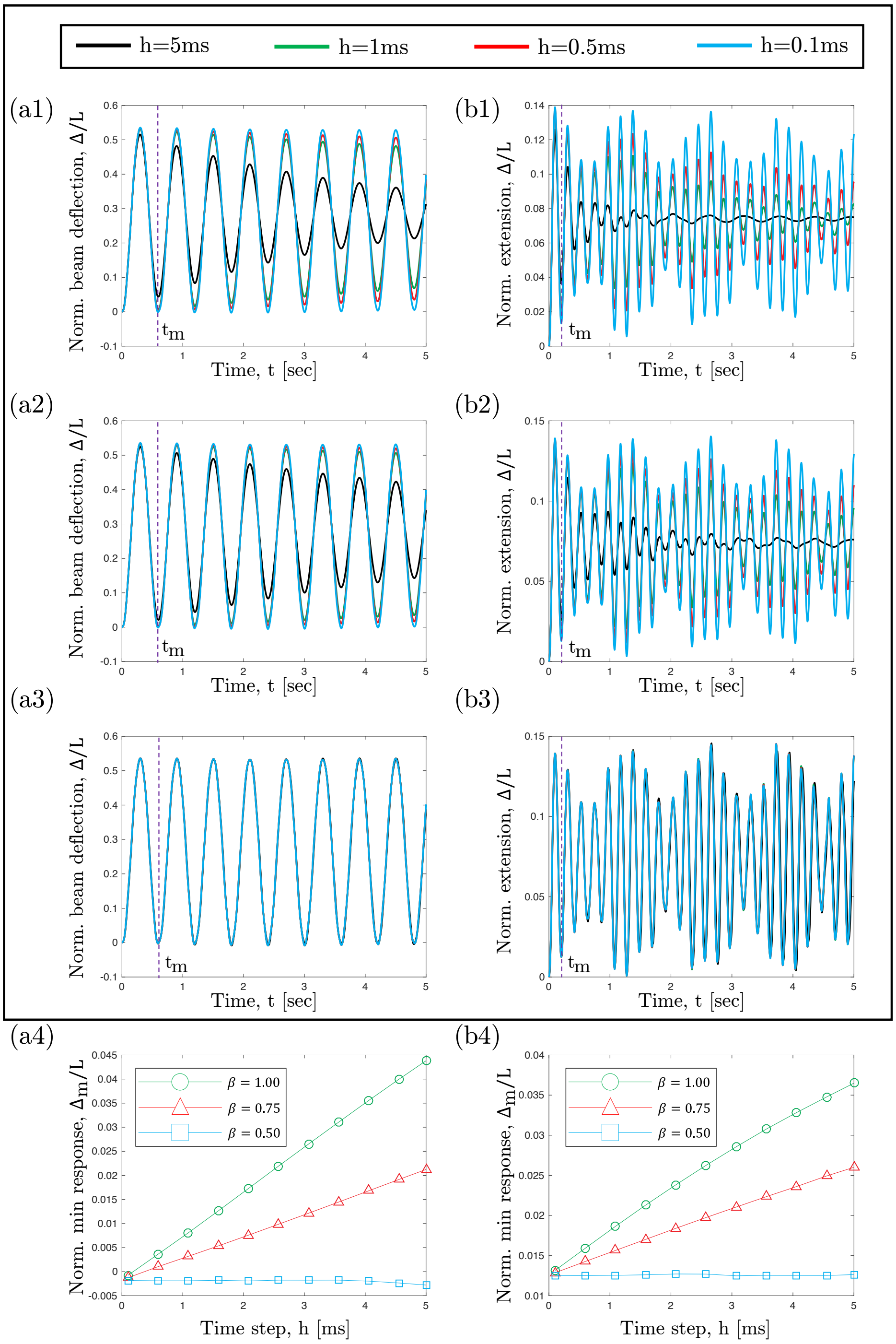

Figure 2.2: Comparison between Euler method and Newmark-beta method for (a) a cantilever beam and (b) a helix. From (1) to (4), (1) Euler method ($\beta = 1.0$); (2) Newmark–beta method with $\beta = 0.75$; and (3) Newmark-beta method with $\beta = 0.5$; (4) normalized minimum deflection, Δ_m/L, in the first cycle as a function of time step size, h. Here, Δ_m is the first local minimum displacement (at time $t = t_m$) for $t > 0$.

long as $h \lesssim 3$ ms. In summary, the modified algorithm resolves the issue with energy loss, allows larger time step size while retaining the physics of the system, and, therefore, improves computation time.

In the second demonstration shown schematically in Fig. 2.1(b), a naturally helical rod is hanging under gravity, with helix radius $R = 2$cm, pitch $\lambda = 5$cm, contour length $s = 0.5$m (resulting in an axial length $L \approx 0.185$m), and Young's modulus $E = 10$ MPa. The other parameters (ρ, g, ν) remain unchanged from the previous cantilever beam example. Figs. 2.2(b1-b3) show the normalized tip extension, Δ/L, (see Fig. 2.1(b) for a schematic of Δ) with time at different values of h using the original DER method and the modified one. In this example, we again notice that the original method sees energy dissipation (and a decay in the amplitude of the motion) as well as strong dependence on the time step size. The modified approach with $\beta = 0.5$, on the other hand, again remedies both of these two issues. Fig. 2.2(b4) presents the normalized minimum extension in the first cycle, Δ_m/L, vs. the time step size, h, for different values of β, and affirms that the Newmark-beta based DER shows better convergence with time step size.

We should note that, despite the lack of accuracy in capturing the physics of the problems, the Euler method-based DER, aided by artificial energy dissipation, can stably take larger time step size [36]. In both the model cases presented above, this method runs into numerical instability in Newton's iterations at $h \gtrsim 100$ms. However, the second-order integration method in DER necessitates $h \lesssim 10$ ms for stable simulation. This difference in the maximum stable step size decreases when damping, e.g., an external force proportional and opposite to velocity, is introduced. As damping resists velocity, such force prevents large changes in nodal coordinates within a single time step and thus typically improves the numerical stability of the algorithm. In short, if fast and stable simulation is the primary concern and the accurate description of the physics is not essential, the original DER formulation with large time step size should be chosen. On the other hand, if accurate dynamics is the focus, the modified Newmark-beta based DER algorithm should be chosen.

2.4 Summary and Outlook

We showed the artificial energy dissipation, using two examples, in the original DER method based on Euler integration and demonstrated that a second order time integration method can solve this issue. Moreover, the modified method shows superior performance when considering the simulation result with time step size. In future, other high order time integration methods, e.g., Range-Kutta method, can be considered. It will be of value to study the implication of the choice of integration method on the accuracy and stability of the DER method. Since our ultimate goal is to resolve the artificial energy dissipation (e.g., for simulation of dynamics of soft robots), we are satisfied with this second order, Newmark-Beta method with $\beta = 0.5$. This extension can now allow DER to seamlessly capture inertia-dominated dynamic processes.

CHAPTER 3

Dynamic Simulation of Soft Robots

Soft robots are primarily composed of soft materials that can allow for mechanically robust maneuvers that are not typically possible with conventional rigid robotic systems. However, owing to the current limitations in simulation, design and control of soft robots often involve a painstaking trial. With the ultimate goal of a computational framework for soft robotic engineering, here we introduce a numerical tool for limbed soft robots that draws inspiration from discrete differential geometry (DDG)-based simulation of slender structures. The simulation incorporates an implicit treatment of the elasticity of limbs, inelastic collision between a soft body and rigid surface, and unilateral contact and Coulombic friction with an uneven surface. The computational efficiency of the numerical method enables it to run faster than real-time on a desktop processor. Our experiments and simulations show quantitative agreement and indicate the potential role of predictive simulations for soft robot design.

We introduce the motivation and relevant literatures in § 3.1. The numerical simulation procedure is detailed in § 3.2, and then we discuss the results in § 3.3. The summary and potential directions for future research are concluded in § 3.4. The content of this chapter has appeared in Ref. [37].

3.1 Motivation

Robots composed of soft and elastically deformable materials can be engineered to squeeze through confined spaces [38], sustain large impacts [39], execute rapid and dramatic shape change [40], and exhibit other robust mechanical properties that are often difficult to achieve with more conventional, piece-wise rigid robots [41]. These platforms not only exhibit unique and versatile mobility for applications in biologically-inspired field robotics, but can also serve as a testbed for understanding the locomotion of soft biological organisms. However, due to the current limitations with simulating the dynamics of soft material systems, design and control of soft robots often involve a painstaking trial and error process, and it can be difficult to relate qualitative observations to underlying principles of kinematics, mechanics, and tribology. Progress, therefore, depends on a computational framework for deterministic soft robot modeling that can aid in design, control, and experimental analysis.

Previous efforts to simulate soft robots have focused on Finite Element Method [7, 42], voxel-based discretization [8, 43], and modeling of slender soft robot appendages using Cosserat rod theory [44, 45]. Drawing inspiration from simulation techniques based on Discrete Differential Geometry (DDG) that are widely used in the computer graphics community [31], we introduce a DDG-based numerical simulation tool for examining the locomotion of limbed soft robots. The DDG approach starts with discretization of the smooth system into a mass-spring-type system, while preserving the key geometric properties of actual physical objects; this type of simulation tool is naturally suited to account for contact and collision [46]. In particular, we treat the robot as being composed of multiple slender actuators that can be modeled using elastic rod theories [29]. In order to achieve rapid simulation runtimes, we adapt fast and efficient physically-based computational techniques that have gained traction within the computer graphics community to model slender structures, e.g., rods [27, 28], ribbons [47], plates [48], shells [49], viscous threads [50], and viscous sheets [51]. Despite the visual realism in these simulation methods, these prior works do not comprehensively capture all the physical ingredients for a physically accurate simulation of fast moving articulated soft robots. Our numerical method integrates these ingredients – frictional contact, material damping, and inertial effect – into a discrete simulation framework to achieve quantitative agreement with experiments. Recently, a DDG-based formulation was used to model a caterpillar-inspired soft robot in which the individual segments of the robot were treated as curved elastic rod elements [52]. Although promising, this formulation could not accurately capture inertial effects – a key feature of fast moving robots – and did not incorporate the necessary contact and friction laws required to achieve quantitative agreement with experimental measurements.

Here, we employ a discrete representation of a soft robot and incorporate Coulomb frictional contact, inelastic collision with ground, and inertial effects in a physically accurate manner. The mechanical deformation of the robot is associated with local elastic (stretching and bending) energies at each discrete node. We formulate these discrete elastic energies and, subsequently, the discrete equations of motion representing the balance of forces using principles from classical elastic rod theories [29]. Coulomb frictional contact with uneven surface is integrated into the formulation using the modified mass method [48], such that a group of constrained equations of motion can be implicitly updated through a second order, symplectic Newmark-beta time integration scheme. Since this integration scheme is momentum preserving, it does not suffer from artificial energy loss – a well-known attribute of first order Euler integration used in prior works with discrete rod simulations [29] – and can capture the essential inertial effects during the dynamic simulation of soft robots. The elastic/inelastic collision between the soft robot and rigid ground can be captured by the rate-dependent viscoelastic behavior of the soft material, i.e., the damping coefficient in Rayleigh's damping matrix is used to precisely control the recovery factor during collision and rebound [35]. Finally, the experimentally measured data of a single actuator during one actuating-cooling cycle is fed into our numerical framework for the investigation of soft robotic dynamics. The result is a robust simulation tool that can run faster than real-time on a single thread of a desktop processor. The reliability of this simulation tool for making quantitative predictions is systematically examined using three test cases. First, we demonstrate that three empirically-observed motion patterns of a deformable rolling ribbon [53] on a declined surface can be captured by our simulator. Next, we build two types of soft robots made of SMA-based limb: a star-shaped rolling robot composed of seven radially oriented limbs and a jumper robot with a single limb. The SMA-based robots were selected because of the ability to achieve rapid dynamic motions in which both material deformation and inertia have a governing role [33, 54]. In order to examine the influence of friction and ground topology, locomotion experiments were performed on flat, inclined/declined, and wavy/undulating surfaces. In all cases, we found reasonable quantitative agreement between experiments and simulations.

3.2 Numerical Framework

In this section, we review the numerical framework that incorporates elasticity, contact with uneven surface, friction, and inelastic collision for a comprehensive soft robot simulator. Since the motion of the robot remains in 2D, we do not include a twisting energy of the rod, although this can be readily integrated into our framework [29]. Starting from the discrete representation of elastic energies, we formulate equations of motion at each node and update the configuration of the structure (i.e., position of the nodes) in time.

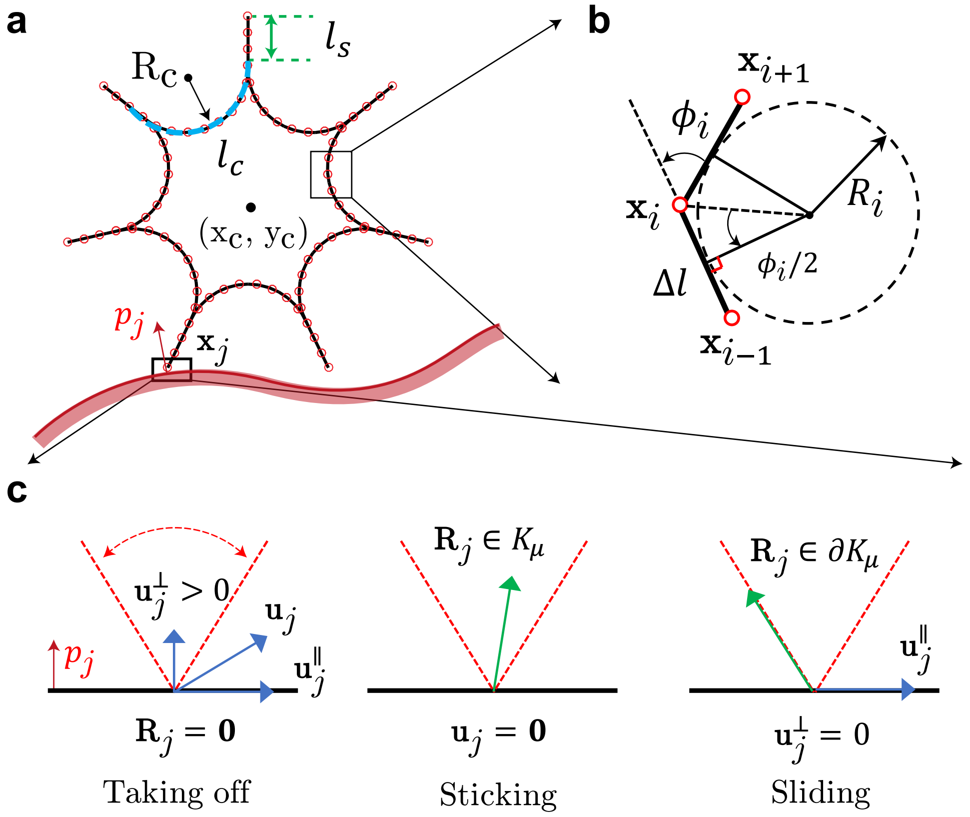

Figure 3.1: (a) Geometric discretization of a soft rolling robot. (b) The bending curvature at i-th node is $\kappa_i = 1/R_i = 2\tan(\phi_i/2)/\Delta l$. (c) Coulomb law for frictional contact.

The rod segment between two consecutive nodes is an edge that can stretch as the robot deforms – analogous to a linear spring. The turning angle ϕ_i (see Fig. 3.1 (b)) at node $\mathbf{x}_i$ between two consecutive edges can change – similar to a torsional spring. The elastic energy from the strains in the robot can be represented by the linear sum of two components: stretching energy of each edge and bending energy associated with variation in the turning angle at the nodes. The discrete stretching energy at the edge connecting $\mathbf{x}_i$ and $\mathbf{x}_{i+1}$ is $E_i^s = \frac{1}{2} EA \varepsilon_i^2 \Delta l$, where EA is the stretching stiffness (calculated as the product of the material elastic modulus E and actuator cross-sectional area A) and $\varepsilon_i = |\mathbf{x}_{i+1} - \mathbf{x}_i|/\Delta l - 1$ is the axial stretch. Associated with each turning angle ϕ_i is the discrete bending energy $E_i^b = \frac{1}{2} EI \left(\kappa_i - \bar{\kappa}_i\right)^2 \Delta l$, where EI is the bending stiffness, $\kappa_i = 2\tan(\phi_i/2)/\Delta l$ is the curvature [Fig. 3.1 (b)], and $\bar{\kappa}_i$ is the natural curvature (i.e., curvature evaluated in undeformed configuration). In the special case of a joint node where three edges meet, the bending energy is comprised of two components: one corresponding to the turning angle between the first and second edges and the second one arises from the turning angle between the second and third edges. The total stretching energy of the robot can be obtained simply by summing over all the edges, i.e., $E^s = \sum_i E_i^s$, and, similarly, the total bending energy is $E^b = \sum_i E_i^b$. In both experiments and simulations, we observe that the structure is nearly inextensible and the prominent mode of deformation is bending. We evaluated the bending stiffness by quantifying the shape of an actuator under vertical load.

The elastic stretching (and bending) forces acting on a node $\mathbf{x}_i$ can be obtained from the gradient of the energies, i.e., $-\left[\frac{\partial E^s}{\partial x_i}, \frac{\partial E^s}{\partial y_i}\right]^T$ (and $-\left[\frac{\partial E^b}{\partial x_i}, \frac{\partial E^b}{\partial y_i}\right]^T$). An implicit treatment of the elastic forces requires calculation of the $2N \times 2N$ Hessian matrix of the elastic energies. Other than the seven joint nodes that are connected with three other nodes, a node $\mathbf{x}_i$ is only coupled with the adjacent nodes $\mathbf{x}_{i-1}$ and $\mathbf{x}_{i+1}$ in the discrete energy formulation. This results in a banded Hessian matrix with 6×6 blocks of non-zero entries along the diagonal. The only off-diagonal non-zero entries correspond to the seven joint nodes. The analytical expressions for the gradient and Hessian of the elastic energies can be found in Refs. [28, 29].

Besides the internal elastic forces, $\mathbf{F}^\mathrm{s}$ and $\mathbf{F}^\mathrm{b}$, the structure would also experience internal damping forces during deformation. We use the Rayleigh damping matrix to formulate the viscoelastic behavior of soft robots, such that the damping force vector is given by [35]

$$\mathbf{F}^{\mathrm{d}} = -\left(\alpha\mathbb{M} + \beta\mathbb{K}\right)\mathbf{v}, \tag{3.1}$$

where $\alpha, \beta \in \mathbb{R}^{+}$ are damping coefficients, $\mathbb{K} = -\frac{\partial}{\partial \mathbf{q}}(\mathbf{F}^{\mathrm{s}}+\mathbf{F}^{\mathrm{b}})$ is the tangent stiffness matrix, and $\mathbf{v}$ is the velocity vector (time derivative of DOF). Also, the external gravity forces are denoted by $\mathbf{F}^{\mathrm{g}}$, as well as the external contact forces, $\mathbf{F}^{\mathrm{r}}$. The gradients of these force vectors can be analytically formulated in a manner similar to those of the elastic forces. The sparse nature of the Jacobian matrix is critical for computational efficiency during the solution of the equations of motion, described next.

The DOF vector can be updated from current time step (t_k) to the next ($t_{k+1} = t_k + h$), $\mathbf{q}^{k+1} = \mathbf{q}^{k} + \Delta\mathbf{q}^{k+1}$, by a second-order, implicit Newmark-beta time integration [35],

$$\begin{aligned}
\Delta\mathbf{q}^{k+1} - h\mathbf{v}^{k} &= \frac{h^2}{4}\mathbb{M}^{-1}\Big(\mathbf{F}^{k+1} + \mathbf{F}^{k}\Big) \\
\Delta\mathbf{q}^{k+1} &= \frac{h}{2}\left(\mathbf{v}^{k+1} + \mathbf{v}^{k}\right) \\
\Delta\mathbf{v}^{k+1} &= \mathbf{v}^{k+1} - \mathbf{v}^{k},
\end{aligned} \tag{3.2}$$

where the velocity vector (time derivative of DOF) is $\mathbf{v}$, superscript $k+1$ (and k) denotes evaluation of the quantity at time t_{k+1} (and t_k), $\mathbb{M}$ is the diagonal mass matrix, h is the time step size, and $\mathbf{F} = \Big(\mathbf{F}^{\mathrm{s}} + \mathbf{F}^{\mathrm{b}} + \mathbf{F}^{\mathrm{g}} + \mathbf{F}^{\mathrm{d}} + \mathbf{F}^{\mathrm{r}}\Big)$ is the sum of elastic, damping, and external forces defined before. In the absence of dissipative forces and external contact forces, this method is symplectic and momentum preserving [55, 35] – a critical feature for simulation of robots where inertial effects are significant.

Since soft robots are often intended for locomotion on unstructured terrain, we require a method to account for contact and friction with the ground. Importantly, the surface normal can vary with the horizontal x-axis. We model the nonpenetration constraints and frictional contact forces that resist sliding along interfaces based on Coulomb's law. At each time step, we apply continuous collision detection to the predicted trajectory to gather contact constraints into a contact set $\mathbb{C}$, shown in Fig. 3.1 (c). For these calculations, the velocity $\mathbf{u} = [\mathbf{v}_{2j-1}, \mathbf{v}_{2j}]^T$ (subscript denotes element number in a vector), and the reaction force $\mathbf{R} = \left[\mathbf{F}^r_{2j-1}, \mathbf{F}^r_{2j}\right]^T$, at the j-th node (the contact point) satisfy the condition

$$\mathbb{C}\left(\mathbf{u}, \mathbf{R}\right) \Leftrightarrow \begin{cases} \mathbf{R} = \mathbf{0} \text{ and } u^{\perp} > 0 \ \text{(taking off)} \\ R^{\parallel} < \mu R^{\perp} \text{ and } \mathbf{u} = \mathbf{0} \ \text{(sticking)} \\ R^{\parallel} = \mu R^{\perp} \text{ and } u^{\perp} = 0 \ \text{(sliding)}, \end{cases} \tag{3.3}$$

where $\mu = 0.8$ is the friction coefficient characterized by experiments, and the superscript $\parallel$ (and $\perp$) denotes the component along (and perpendicular to) the ground. At the normal and tangential subspaces of a contact node $\mathbf{x}_j$, we either know its perpendicular velocity $u^{\perp}$ ($u^{\parallel}$ for tangential component) or the perpendicular reaction force $R^{\perp}$ ($R^{\parallel}$ for tangential component), so the Coulombic frictional contact law can be treated as a Second Order Linear Complementary Problem (SOLCP) [56]. We employ the modified mass method [48] to solve this SOLCP such that a contact node $\mathbf{x}_j$ can be free (degrees of freedom is 2, taking off), constrained along the normal to the ground $\mathbf{p}$ (degrees of freedom is 1, sliding), or fully constrained (degrees of freedom is 0, sticking). The two modified equations of motion for the j-th node ($j = 1, \ldots, N$) are

$$\begin{bmatrix} \mathbb{F}_{2j-1} \\ \mathbb{F}_{2j} \end{bmatrix} \equiv \begin{bmatrix} \Delta \mathbf{v}^{k+1}_{2j-1} \\ \Delta \mathbf{v}^{k+1}_{2j} \end{bmatrix} - \frac{h}{2M_j} \mathbf{S}^{k+1} \left(\begin{bmatrix} \mathbf{F}^{k+1}_{2j-1} \\ \mathbf{F}^{k+1}_{2j} \end{bmatrix} + \begin{bmatrix} \mathbf{F}^{k}_{2j-1} \\ \mathbf{F}^{k}_{2j} \end{bmatrix} \right) - \Delta \mathbf{z}^{k+1} = \mathbf{0}, \tag{3.4}$$

where $\mathbb{F}_{2j-1}$ is the left hand side of the $(2j-1)$-th equation of motion, M_j is the mass associated with j-th node, $\Delta \mathbf{z}^{k+1}$ is the change in velocity we want to enforce along the constrained direction(s), and the modified mass matrix is

$$\mathbf{S}^{k+1} = \begin{cases} \mathbb{I} & \text{if ndof} = 2, \\ (\mathbb{I} - \mathbf{p}\mathbf{p}^T) & \text{if ndof} = 1, \\ \mathbf{0} & \text{if ndof} = 0, \end{cases} \tag{3.5}$$

where ndof is the number of free DOF at j-th node and $\mathbb{I}$ is the 2×2 identity matrix. Note that when a node is free, $\Delta \mathbf{z}^{k+1} = \mathbf{0}$, and Eq. (3.4) reduces to Eq. (3.2). If the node is fully constrained ($\mathbf{S}^{k+1} = \mathbf{0}$), Eq. (3.4) reduces to $\Delta \mathbf{v}_j^{k+1} = \Delta \mathbf{z}^{k+1}$ and the change in velocity (as well as the position) is enforced to take the value prescribed by $\Delta \mathbf{z}^{k+1}$.

The solution to the $2N$ equations of motion in Eq. (3.4) starts with an initial guess $\left(\Delta \mathbf{v}^{k+1}\right)^{(0)}$ and subsequent Newton's iterations to improve the solution until a desired tolerance is achieved:

$$\left(\Delta \mathbf{v}^{k+1}\right)^{(n+1)} = \left(\Delta \mathbf{v}^{k+1}\right)^{(n)} - \mathbb{J}^{(n)} \backslash \mathbb{F}^{(n)}, \tag{3.6}$$

where $\mathbb{J}^{(n)} = \frac{\partial \mathbb{F}}{\partial (\Delta \mathbf{v}^{k+1})}$ is the Jacobian matrix evaluated at $\left(\Delta \mathbf{v}^{k+1}\right)^{(n)}$. The non-trivial terms in the evaluation of this Jacobian are the Hessian matrices of the elastic energies. Due to the presence of the ground, we need to check whether the new solutions, e.g., $\mathbf{q}^{k+1}$, $\mathbf{v}^{k+1}$ and $(\mathbf{F}^r)^{k+1}$ (computed from force balance), satisfy the following conditions:

- A node $\mathbf{x}_j$ cannot fall below the ground.
- The normal component of reaction force $R^{\perp}$ exerted by the ground on a node $\mathbf{x}_j$ must be along the outward normal to the surface, e.g., $R^{\perp} > 0$.
- The reaction force $\mathbf{R}$ should be in the frictional cone zone K_{μ} (see Fig. 3.1 (c)); if the reaction force is on the boundary of the cone, this node is allowed to slide along the tangential direction of surface opposite to reaction force, $\mathbf{u} \cdot \mathbf{R} < 0$.
- If the tangential velocity $u^{\parallel}$ at a sliding node $\mathbf{x}_j$ changes its direction, $(u^{\parallel})^k \cdot (u^{\parallel})^{k+1} < 0$, this node should be fully constrained.

If one of the above rules is broken, we rewind the simulation, add (or delete) constraints at the contact pair, and re-solve Eq. (3.4) with a new guess.

When an elastic body drops onto a rigid surface, the motion normal to the surface of the contact nodes are constrained, the normal velocities are set to zero, and the tangential velocities are reduced based on impulse theory, $\Delta u^{\parallel} = \mu \Delta u^{\perp}$. If the structure is modeled as an ideal mass-spring system without viscoelasticity, the whole structure will rebound to a certain height and the recovery factor – the ratio of rebound to initial height – is not deterministic. This arises because the structure's kinetic energy will transfer into elastic potential energy during compression and then convert back to kinetic energy during the rebound phase [35]. We must account for the rate-dependent viscoelasticity of contact for predictive simulation, where the energy loss of the collision-compression-rebound process results in a deterministic rebound height. We show that the decrease in rebound height of the rolling robot can be determined by the parameter β in damping force $\mathbf{F}^{\mathrm{d}} = -\left(\alpha\mathbb{M} + \beta\mathbb{K}\right)\mathbf{v}$, such that the recovery factor of collision is also related to β. Physically, β represents a damping that opposes elastic deformation, without penalizing rigid body motion. Opposition to rigid body motion and momentum dissipation can be accounted by the viscosity α. The overall numerical framework thus accounts for inertia, friction, and collision and shows good convergence with both time and space discretization.

3.3 Results

3.3.1 Actuator Characterization

In this section, we study the mechanical property of a single Shape Memory Alloy (SMA) actuator. We manufactured a single curved SMA actuator sample with the following geometric parameters: arc length $L_s = 33\mathrm{mm}$, undeformed curvature $\bar{\kappa}_0 \equiv 1/R_0 = 97.03\mathrm{m}^{-1}$, thickness $h = 1.72\mathrm{mm}$, width $w = 19.42\mathrm{mm}$. The material density is $\rho = 1920\mathrm{kg}\cdot\mathrm{m}^{-3}$, which is similar to our previous study [33, 54, 52].

We employ load-displacement relation to find the Young's modulus of a single SMA actuator for both unactuated and actuated state. In Figure 3.2 (a) (unactuated state) and (b) (actuated state), we use a $20\mathrm{g}$ weight to apply a vertical load at the end of the actuator and evaluate the end displacement. Then we use simulation to find the Young's modulus that best matches the experimental results. In Figure 3.2 (c) and (d), we plot the best fit configurations of SMA actuator before/after loading. Here, the Young's modulus we found in unactuated state is $E_0 = 3.0$ MPa, and $E_{\text{max}} = 8.04$ MPa in actuated state; these are comparable to the values reported in Ref. [52].

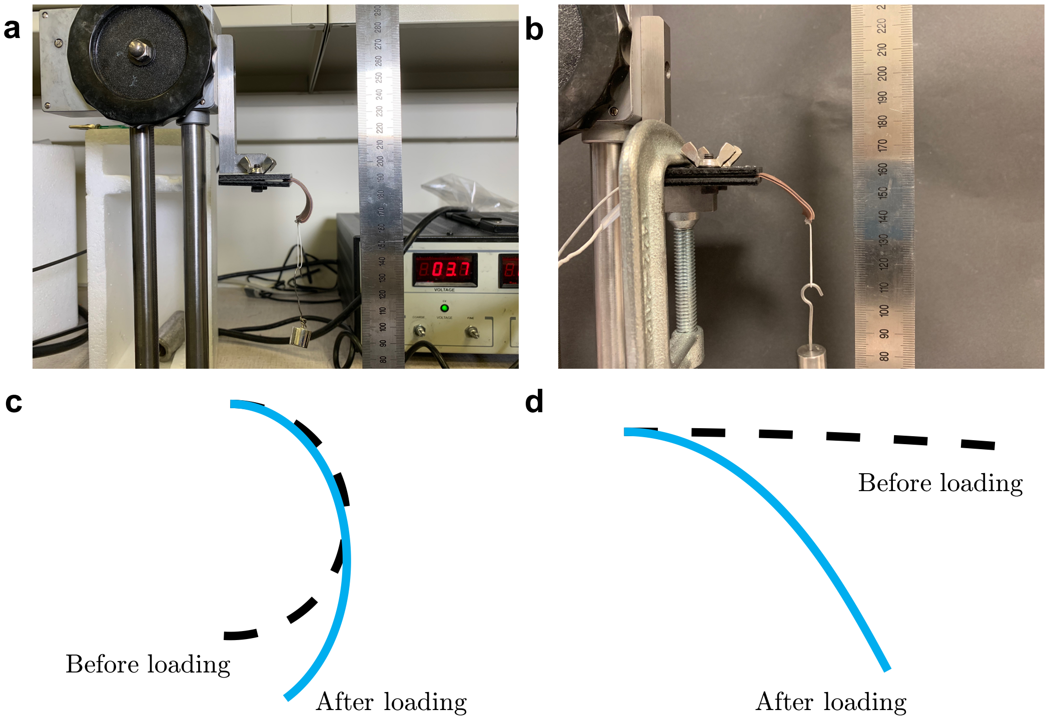

Figure 3.2: (a) Shape memory alloy actuator in unactuated state under loading. (b) Shape memory alloy actuator in actuated state under loading. (c) Simulation results of initial configuration (dashed line) and deformed configuration (solid line) in unactuated state. (d) Simulation results of initial configuration (dashed line) and deformed configuration (solid line) in actuated state.

Next, we model the dynamics of a single SMA-based actuator during actuating/cooling process. In Figure 3.3 (a) and (b), we show the undeformed shape and maximum response shape of SMA-based actuator during heating-cooling process separately. The heating time used in this experiment is 0.25s, and cooling time is 2.75s. We assume that the natural curvature $\bar{\kappa}(t)$ follows a piece-wise function,

$$\bar{\kappa}(t) = \begin{cases} \frac{(n_1-1)t}{t_0}\bar{\kappa}_0 + \bar{\kappa}_0 \text{ when } t < t_0 \\ \frac{(1-n_1)}{1+e^{-\tau(t-\bar{t})}}\bar{\kappa}_0 + n_1\bar{\kappa}_0 \text{ when } t > t_0, \end{cases} \tag{3.7}$$

and similarly for Young's modulus $E(t)$,

$$E(t)=\begin{cases}\frac{(n_2-1)t}{t_0}E_0+E_0 \text{ when } t<t_0\\ \frac{(1-n_2)}{1+e^{-\tau(t-\bar{t})}}E_0+n_2E_0 \text{ when } t>t_0,\end{cases} \tag{3.8}$$

where n_1 and n_2 are the ratios between unactuated state and actuated state, $n_1=\bar{\kappa}_{\text{min}}/\bar{\kappa}_0$, $n_2=E_{\text{max}}/E_0$ (the actuated curvature is smaller than unactuated state, while Young's modulus follows an opposite pattern), $t_0=0.05\text{s}$, $\bar{t}=1.4\text{s}$, and $\tau=3.4\text{s}^{-1}$ are from experimental fitting.

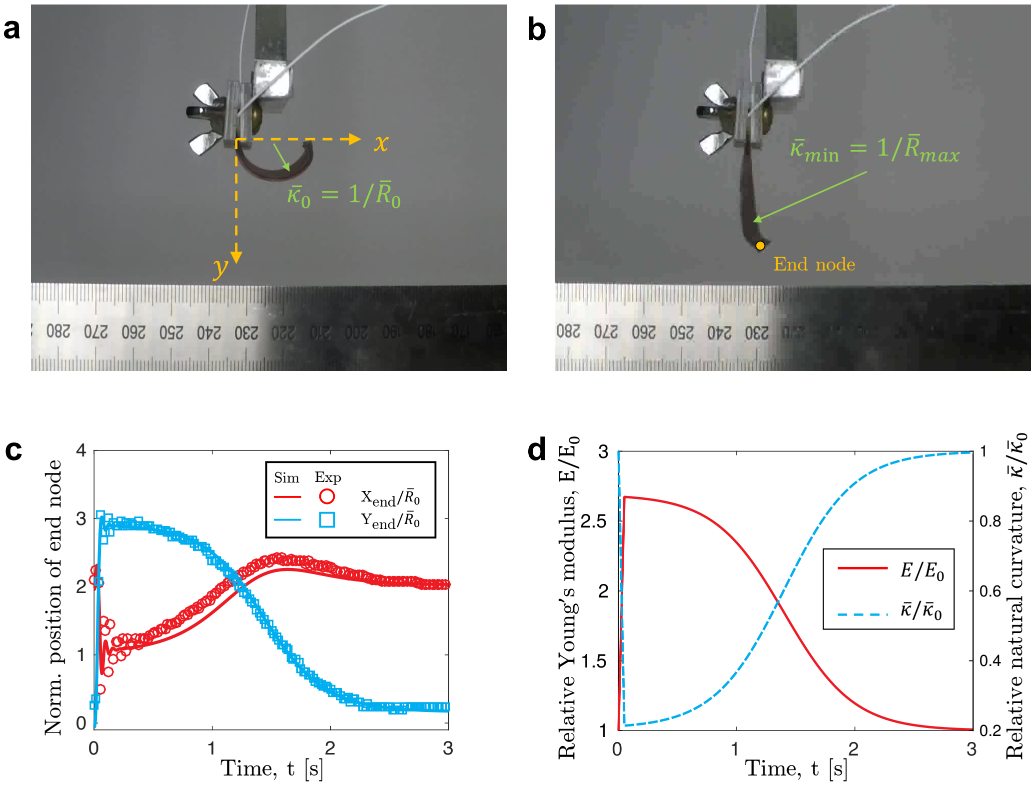

Figure 3.3: (a) The shape of SMA-based actuator before actuating. (b) Maximum response of SMA-based actuator during actuating process. (c) Relative beam end displacement $X_{\text{end}}/\bar{R}_0$ and $Y_{\text{end}}/\bar{R}_0$ from both experiments and simulations. (d) Relative Young's modulus E/E_0 (solid) and relative natural curvature $\bar{\kappa}/\bar{\kappa}_0$ (dashed) change as a function of time during actuating/cooling process.

The ratio of Young's modulus, $n_2=E_{\text{max}}/E_0=2.68$, can be easily obtained based on previous loading experiments; another experimentally evaluated parameter, minimum natural curvature, is $\bar{\kappa}_{\text{min}} = 20\text{m}^{-1}$, resulting in $n_1 = 0.21$. We use these fitting parameters to perform this dynamic process in our simulation, and plot the relative beam end position, $X_{\text{end}}/\bar{R}_0$ and $Y_{\text{end}}/\bar{R}_0$, as a function of time during this dynamic process in Figure 3.3 (c). Then, in Figure 3.3 (d), we plot these best fitting parameters, e.g., relative Young's modulus E/E_0 and relative natural curvature $\bar{\kappa}/\bar{\kappa}_0$, as a function of time, during the actuating process.

3.3.2 Rolling Ribbon

Before examining soft robot locomotion, we first investigate the simpler motion of a circular ribbon on a declined surface in order to test the accuracy of numerical implementation of friction and contact. In the numerical study of rolling ribbon, the arc length we chose for the circular ribbon is $L_0 = 0.3\text{m}$, resulting in $\bar{R}_0 = 0.3/2\pi \approx 0.048\text{m}$. The ribbon thickness is $r_0 = 1\text{mm}$, poisson ratio $\nu = 0.5$ (incompressible material), material density $\rho = 1237.52\text{kg/m}^3$, and we vary the Young's modulus, E, from 1 MPa to 100 MPa to vary the governing dimensionless group Γ_g. The damping parameters are $\alpha = 0$ and $\beta = 1e^{-3}$; however, since we do not quantitatively study the transient dynamics, these parameters do not affect the final deformed configuration and motion patterns.

Here, we show the different motion patterns of rolling ribbon. Consider a circular ribbon with $\Gamma_g = 0.57$ [53] that is moving in a declined surface with $\theta = -17.19°$. Because of gravity, this close-loop elastic structure will first undergo transient dynamics and then, as shown in Fig. 3.4 (a), move with a steady state configuration. The final shape is determined by the ratio $\Gamma_g = L_g/R$ of the gravito-bending length scale $L_g = (EI/\rho g A)^{1/3}$ to the ribbon undeformed radius R [53]. In Fig. 3.4 (b), we plot the static configurations of rolling ribbon at different values of Γ_g. At small values of Γ_g, the ribbon shows relatively large deformation with large region of contact. As Γ_g increases, the deformed shape becomes closer to its original undeformed shape and the contact length decreases to reach a single point at $\Gamma_g = \infty$.

Now we turn to the motion of a rolling ribbon. Three different motion patterns exist on a declined surface: pure sliding, combined sliding and rotation, and pure rotation,

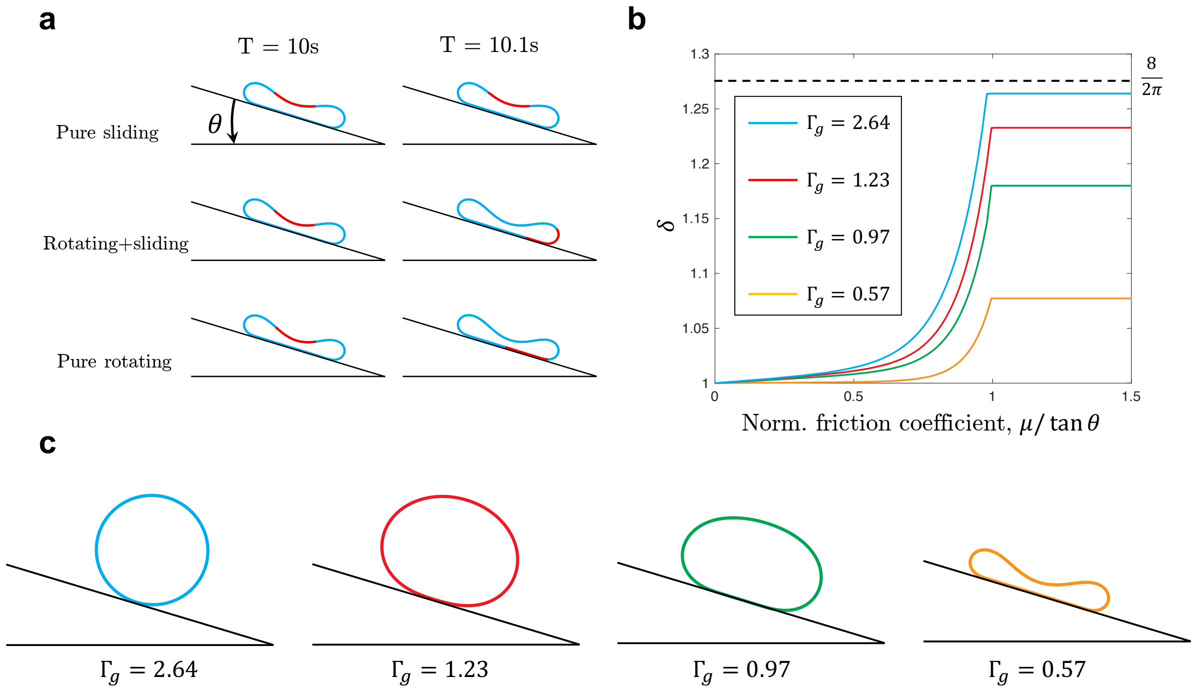

Figure 3.4: (a) Three different patterns in rolling ribbons: pure sliding ($\mu/\tan\theta = 0$), combination of sliding and rotating ($0 < \mu/\tan\theta < 1$); and pure rotating ($\mu/\tan\theta \geq 1$). (b) The ratio between the route of ribbon boundary point and ribbon centroid, $\delta = s_b/s_c$, as a function of normalized frictional coefficient $\mu/\tan\theta$, for different values of normalized ribbon curvature, Γ_g. (c) Different typologies of rolling ribbons with different Γ_g.

depending on a dimensionless number, $\mu/\tan\theta$, where μ is the frictional coefficient and θ is the decline angle. When the normalized frictional coefficient $\mu/\tan\theta = 0$, the ribbon will slide along the tangential direction of the surface without any rotation, and the path of boundary point is the same as the path of center, $\delta = 1$. If $0 < \mu/\tan\theta < 1$, the motion of the ribbon is a combination of sliding and rotation, and the larger the friction, the higher the δ. The ribbon undergoes pure rotation at $\mu/\tan\theta \geq 1$ when δ remains fixed at a constant value depending on Γ_g. At the limiting case of a rigid ribbon, the motion is purely rotational and any point on the ribbon traces a cycloid path, corresponding to $\delta = 8/2\pi$.

3.3.3 Rolling Robot

The star-shaped, rolling robot in Fig. 3.1 (a) is comprised of seven compliant actuators/limbs that are arranged radially. Each limb has a curved part with length $l_c = 2.2$cm and a straight part with length $l_s = 0.8$cm. The natural curvature of the curved part is $\bar{\kappa}_0 \equiv 1/R_c = 120\text{m}^{-1}$. The material density of the rolling robot is $\rho = 1912$ kg·m^{-3}. The mass center is located at (x_c, y_c). The height, $H \approx 5$ cm, is used as the body length. We then discretize the structure into N nodes, shown schematically in Fig. 3.1 (a). This corresponds to a degrees of freedom (DOF) vector, $\mathbf{q} = [x_0, y_0, ..., x_{N-1}, y_{N-1}]^T$, of size $2N$, representing the vertical and horizontal coordinates of each node. Here, the superscript T denotes transposition. The length of each edge – the segment between two consecutive nodes – in this study is $\Delta l \approx 2.5$ mm, resulting in $N = 84$ nodes.

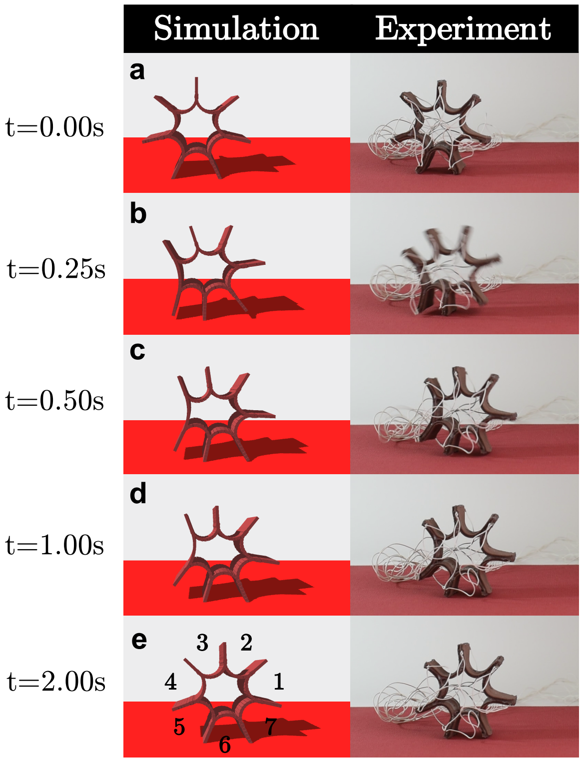

Figure 3.5: Snapshots of rolling robot from simulations and experiments between $t = 0.0$s and $t = 2.0$s. Limb #4 is actuated for a rolling motion. The width (out-of-plane dimension in this figure) is 18mm.

The simplest scenario is presented in Fig. 3.5, where the surface normal is anti-parallel to gravity. Fig. 3.6 (d) plots the x-coordinate of the centroid of the robot, x_c, with time over four actuation cycles. Note that the different symbols correspond to repeated experimental runs. In our numbering system for the limbs (see Fig. 3.5), Limb 5 is in contact with the ground at $t = 0$. Upon actuation of Limb 4, the robot rolls to the right and the contact limb changes from 5 to 6. In the next cycle, Limb 5 (the limb to the left of the contact limb) is actuated. We choose the actuation period $\Delta t = 3$s (0.25s for actuation and 2.75s for cooling); the single SMA actuator can totally reshape to its original configuration within 3s.

Next, we consider planar surfaces that are inclined at an angle θ with respect to the horizontal plane. Fig. 3.6 (a) compares the simulation and experimental results for $\theta = +3.0°$, and Fig. 3.6 (e)-(g) plots the location of the robot centroid at three different values of θ. We find good agreement between experiments and simulation in all the cases. In particular, we observe that when the angle of inclination increases from $\theta = -3.0°$ to $\theta = +3.0°$, the distance traveled by the robot decreases in both experiments and simulations. The gait at $\theta = \{-3.0°, +3.0°\}$ is similar to the horizontal planar case described above. Beyond a certain threshold for θ, the robot can no longer move forward due to the increased role of gravity, e.g., the robot fails to roll up the incline when at $\theta = +6.0°$. The simulation also accurately captures this observation.

We now move to the case of an uneven surface with an outward normal that varies with location. As a representative example shown schematically in Figs. 3.6 (b) and (c), we consider a 3D printed surface that can be described by $f(x) = A \sin(2\pi x/\lambda)$ with amplitude $A = 6.5$mm and period $\lambda = 200$mm. We consider two experimental trials: first, the robot is initially located at the crest of the surface in Fig. 3.6 (b); and second, the robot is on the trough in Fig. 3.6 (c). Fig. 3.6 (h) and (i) show the location of the robot centroid with time from both experiments and simulations. In the crest case, the robot rolls once at the first cycle. However, at the second cycle, the robot rolls multiple times, undergoes oscillatory motion, and settles stay at the trough. On the other hand, if the locomotion starts with the robot at the trough, the robot successfully rolls once in the first two cycles, but fails to roll in the third cycle. All of these observations are captured in both experiments and simulations. However, we should also note that our simulator always under-predicts the motion of the rolling robot. We attribute this to the finite thickness of the actuator elements, which is not accounted for in the model

Our novel numerical tool can achieve real-time simulation of the soft rolling robot. In Fig. 3.7, with a fixed number of vertices, $N = 84$, the computation time linearly scales with time step size h for all the scenarios. The simulations ran on a single thread of AMD Ryzen 1950X CPU @ 3.4 GHz. Also, our simulator can run faster than real time when the time step size $h \gtrsim 2.5$ms. Numerical issues associated with a large step size appear at $h \gtrsim 10$ms, in which case the computation time is infinite because we cannot get convergence.

3.3.4 Jumper Robot

Finally, we emphasize the generality of the simulation by examining another soft robot with a different geometry. The SMA-based jumper shown in Fig. 3.8 (a) is an asymmetric circle with arclength $\bar{R}_0 \approx 0.05$m. The material used in Jumper Robot is identical to the one used in the rolling robot, discussed in the previous section.

Also, we applied a constant force $\mathbf{F}_0$ on the first node on jumper robot over $t_0 \leq t \leq t_1$ (t_0, t_1 are parameters obtained from data fitting) to emulate the presence of the electrical wire. After fitting to experimental data, the horizontal and vertical components of this external force are $F_0^x = 0.05Mg$ and $F_0^y = 0.8Mg$, where M is the total mass of jumper robot. This force is applied at $t_0 = 0.1$s, and ended at $t_1 = 0.15$s. When the material is actuated, the whole structure can rise and move forward because of the reaction forces from the ground. To model the tension from the electrical wire connected at the leading edge of the jumper, we apply a force at the first node; the magnitude and duration of the force are obtained from fitting to experimental data. In Fig. 3.8 (a), we show snapshots of the jumper at $t = \{0.000, 0.125, 0.250\}$s from both experiments and simulations and see qualitative agreement. For quantitative comparison, Figs. 3.8 (b) and (c) present experimental and simulation data on the normalized position of the first node on the robot as a function of time. The two sets of results – experiments and simulations – appear to be in strong quantitative agreement, providing further evidence for the physical

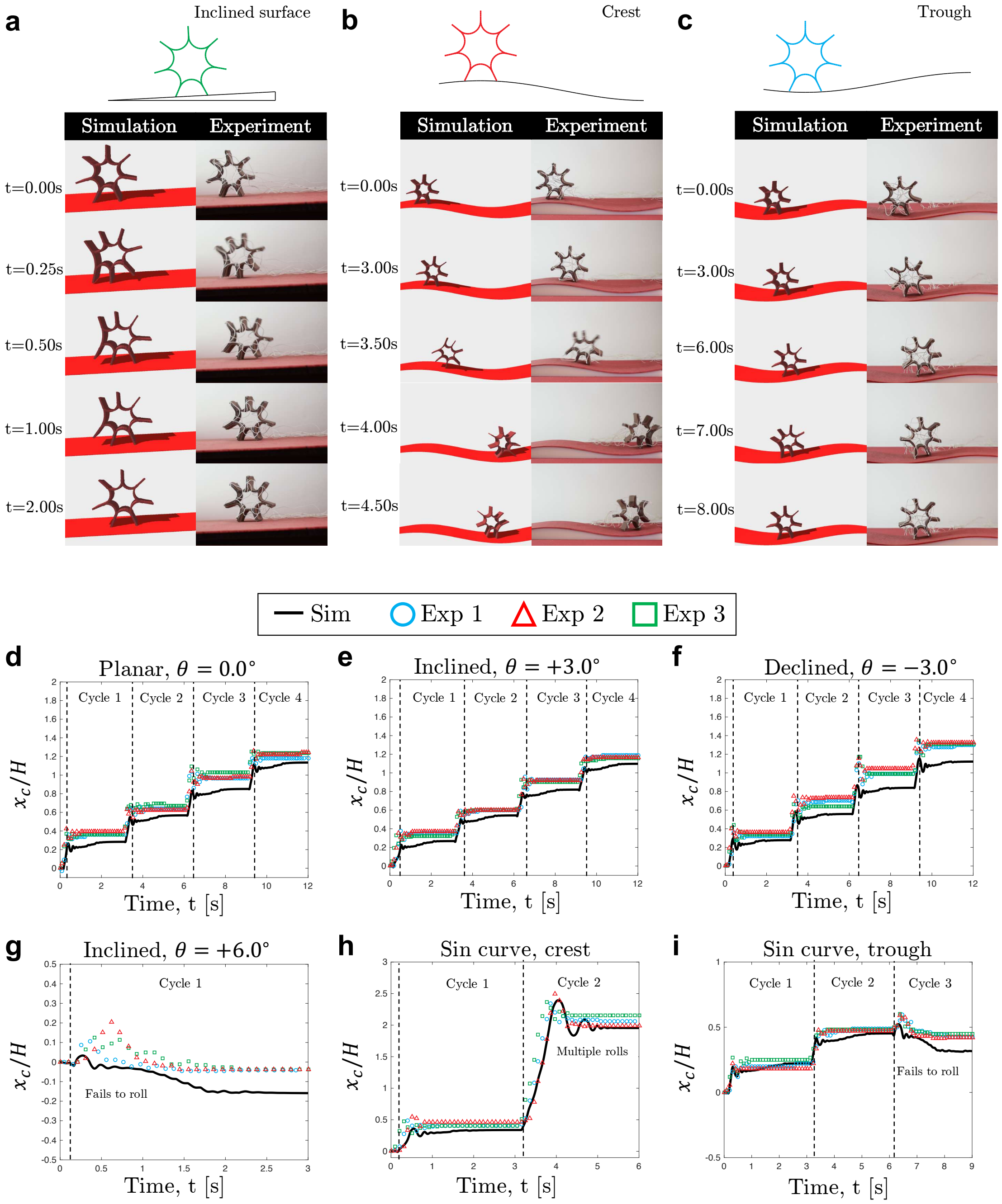

Figure 3.6: (a) Inclined surface ($\theta = +3.0°$), (b) Crest of sinusoidal surface, and (c) Trough of sinusoidal surface. Normalized x-coordinate of the robot centroid with time from experiments (symbols) and simulations (solid lines): (d) planar surface, $\theta = 0.0°$; (e) inclined surface, $\theta = +3.0°$; (f) declined surface, $\theta = -3.0°$; (g) inclined surface, $\theta = +6.0°$; (h) sinusoidal surface, crest; and (i) sinusoidal surface, trough.

accuracy of our DDG-based formulation. We should also note that, at time $t = 1.5$s, the x position predicted by numerical simulation has a sudden drop, which is not reflected

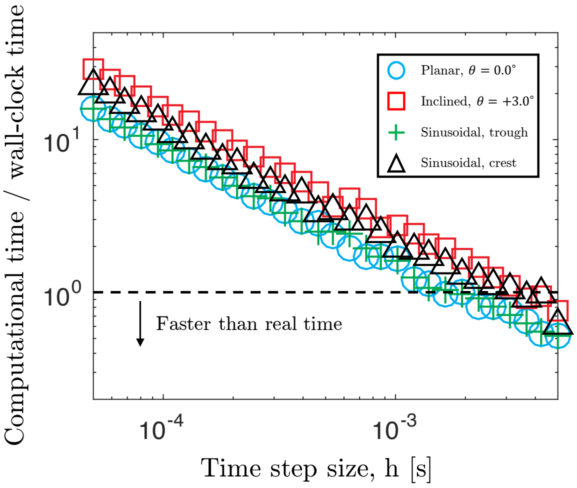

Figure 3.7: The ratio between computational time and wall-clock time as a function of time step size h in different scenarios with $N = 84$.

in the experimental data. The mismatch between numerical simulation and experimental observation is due to the discontinuity in Coulomb's formulation, i.e., the jumper robot would move only if the external reaction force is out of the frictional cone.

3.3.5 Convergence Study

Our simulation is robust and shows good convergence with both time and space discretization. In Figure 3.9 (A1)-(A4), we plot the normalized centroid of rolling robot x_c/H, as a function of time, at a fixed number of vertices $N = 84$ and different values of time step size h. Our simulations show good convergence with time for all the following cases: (A1) planar motion, (A2) inclined surface with $\theta = +3.0°$, (A3) crest, and (A4) trough. Numerical issues begin to appear beyond $h = 10$ ms. Similarly, we vary number of vertices, N, in Figure 3.9 (B1)-(B4) and fix the time step size at $h = 0.1$ ms to show the convergence with space discretization of our simulator. The simulation fails to make quantitative prediction around $N \approx 50$, e.g., see the data corresponding to $N = 49$ in Figure 3.9 (B4).

3.4 Summary and Outlook

We have introduced a numerical framework based on DER for examining the locomotion of limbed soft robots that is adapted from methods popular in the computer graphics com-

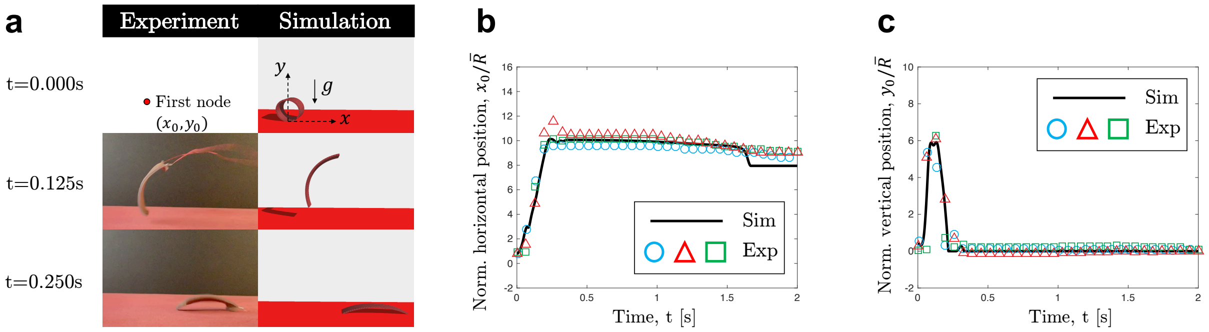

Figure 3.8: (a) Snapshots of the jumper robot from experiments and simulations at different time steps. (b) Normalized x position of the first node (marked in A) in jumper robot as a function of time from experiments (symbols) and simulations (solid lines). (c) Normalized y position of the first node (marked in A) in jumper robot as a function of time from experiments (symbols) and simulations (solid lines).

munity. To avoid the artificial energy dissipation during the time marching scheme, we replaced the first order, implicit Euler integration by a second order, symplectic Newmark-beta method, for momentum preservation during the dynamic simulation. For the frictional contact between the rigid wall and the soft material, Coulomb's law was implemented through a modified mass-based method, and this fully implicit framework allows a larger time step for convergence and numerical stability, which is also a prerequisite for real-time simulation. Similarly, the elastic/inelastic collision between the rigid wall and soft robots, related to the rate-dependent viscoelastic behavior of soft material, can be precisely described by the Rayleigh damping matrix. The mechanical response of SMA during actuating-cooling process was first experimentally measured through a single actuator, then fed to the numerical framework to simulate the dynamics of the soft robots. Overall, the simulation can seamless integrate elasticity, actuation, friction, contact, and elastic/inelastic collision to achieve quantitative prediction of the motion of fast moving highly deformable soft robots. The computational efficiency makes it ideally suited for algorithms that iterate over a wide variety of parameters in order to select a robot design or locomotion strategy.

Overall, our results show good quantitative agreement between the simulations and experiments, suggesting that our numerical approach represents a promising step towards

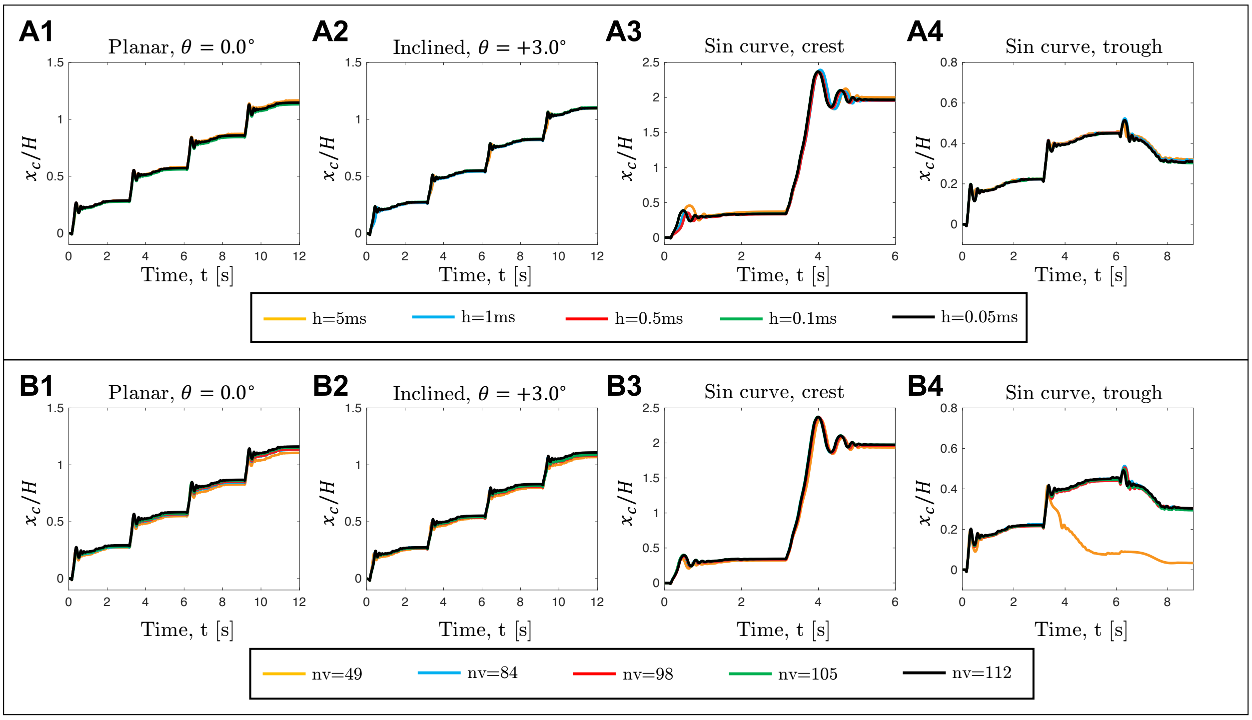

Figure 3.9: (A1)-(A4) Convergence study of rolling robot for time discretization (with $N = 84$ fixed). (B1)-(B4) Convergence study of rolling robot for space discretization (with $h = 0.1$ms fixed).

the ultimate goal of a computational framework for soft robotics engineering. However, further progress depends on additional experimental validation for a wider range of soft robot designs, locomotion gaits, and environmental conditions. The simulation introduced here also needs some prerequisite experimentally measured data, e.g., material properties of soft materials and their mechanical performance in response to external actuation. It would be meaningful to develop a more general constitutive relations that combines mechanics, electricity, heat, and magnetic field, for the direct simulation of soft robotic dynamics in response to external actuation. Moving forward, it would also be interesting to explore how DDG-based simulation tools that incorporate the formulation presented here can be used to generate optimal locomotion gaits that minimize cost of transport or maximize range for a prescribed energy input.

CHAPTER 4

Modeling of the Soft Swimming Robots

Soft swimming robots are primarily composed of elastically deformable materials, which typically make up the robot's body, limbs, and/or fins. Such robots can swim by moving their limbs, flapping their fins, or undulating their body in order to control thrust and direction. This chapter presents a technique to model these soft swimming robots using a computational framework based on the method of Discrete Elastic Rods (DER). This approach to soft robot simulation draws inspiration from methods to simulate slender structures that are widely used in the computer graphics community. In this framework, the soft robot limbs or fins are treated as flexible rods that deflect in response to internal actuation and surface tractions from contacting bodies and the surrounding fluid. Here, we apply this model to the special case of a seastar-inspired robot composed of radiating limbs that produce motion through bending and hydrodynamic drag. We begin with an overview of the DER-based framework and then present simulation results for forward swimming and turning.

We introduce the motivation and literatures in § 4.1. The numerical model is detailed in § 4.2. Next, we discuss the results in § 4.3. The summary and outlook are presented in § 4.4. The content of this chapter has appeared in Ref. [57].

4.1 Motivation

Recent progress in the field of soft robotics [58] has led to new classes of bio-inspired swimming robots that are largely composed of soft and elastically deformable materials. These include robots powered with hydraulics [59], ionic polymer-metal composites (IPMCs) [60], dielectric elastomer actuators (DEAs) [61], and shape memory alloy

(SMA) [62]. SMA-powered actuators are especially promising for swimming robots since the heat used to activate the SMA can be quickly dissipated by convection through the surrounding water. An example of a soft swimming robot inspired by the seastar is presented in Fig. 4.1. The limbs of the robot are composed of soft silicone elastomer that are embedded with SMA wires. When electrical current is delivered to the wires, they cause the limbs to bend and generate a forward thrust.

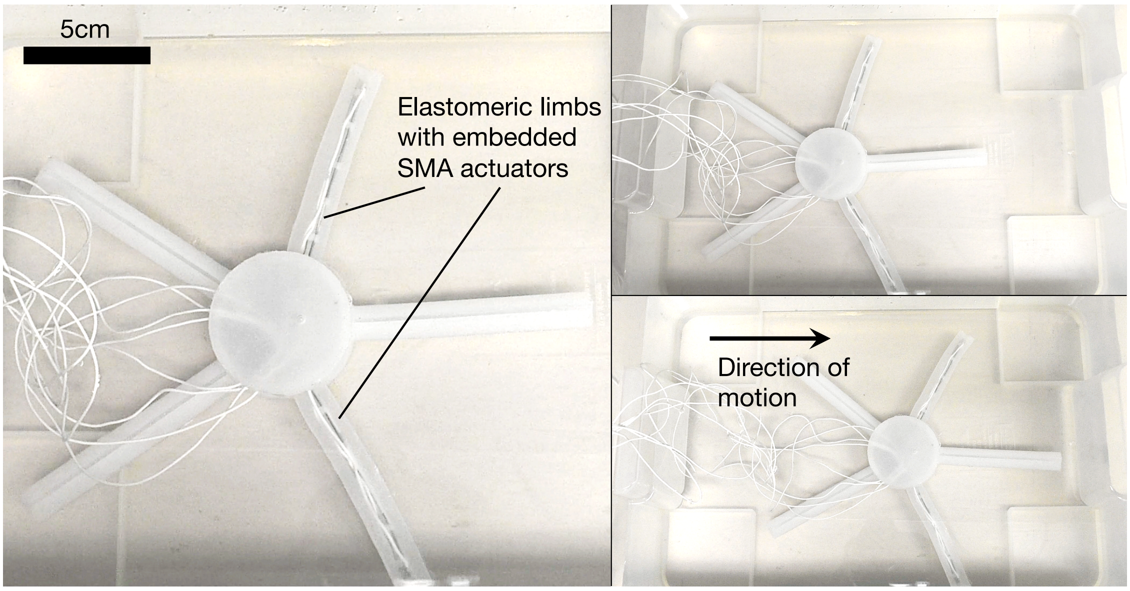

Figure 4.1: SMA-powered seastar-inspired soft robot.

There are a variety of computational tools that can be used to model soft robots like the seastar-inspired robot described above. These include reduced-order Finite Element Analysis (FEA) formulations [63] as well as 3D representations using voxel-based discretization [8]. Recently, there has been interest in modeling soft robots as a combination of slender soft appendages using elastic rod theory [44]. When combined with Discrete Differential Geometry (DDG)-based numerical tools used within the computer graphics community, these rod theories can be used to achieve rapid simulation runtimes.

The DDG-based approach to simulation has been used to model elastic slender structures, e.g., rods [29, 28] and plates [48]. The method of Discrete Elastic Rods (DER) is emerging as an especially popular tool for rapid simulation of engineered systems composed of slender filamentary structures. Goldberg et al. used a 2D version of DER to simulate a crawling, caterpillar-inspired soft robot in which each robot segment was modeled as an elastic rod element [52].

This chapter shows how DER can be used to simulate seastar-inspired soft swimming robots composed of radiating elastic limbs that flap in response to actuator stimulation. Fig. 4.2 presents several snapshots of seastar-inspired soft robot moving through a prescribed regular pentagon trajectory from simulation side. Here, the actuated limbs are highlighted as blue, and the corresponding actuating sequence of the presented trajectory is in Fig. 4.7(b). Our analysis is limited to two dimensions, although it can be easily generalized into 3D as detailed in [29], which presents a comprehensive description of the DER formulation and its application to robotics modeling. We begin with a brief background on DER, followed by an overview of the mathematical formulation used to describe the kinematics, elastic energies, and time marching scheme of rod system. Next, we apply this model to simulate the dynamics of a robot composed of five radiating limbs moving in a fluid.

4.2 Numerical Model

Each limb of the soft robot is treated as a planar elastic rod (cf. elastic beam) that bends in the $x - y$ plane. In the discrete setting of DER shown schematically in Fig. 4.3, the rod centerline is discretized into N nodes: $\mathbf{x}_0, ..., \mathbf{x}_{N-1}$, where $\mathbf{x}_i \equiv [x_i,\ y_i]^T$, superscript T denotes transposition operation, and $0 \leq i \leq N-1$, such that the total degree of freedom (DOF) vector was size of $2N$,

$$\mathbf{q} = [x_0, y_0, x_1, y_1, ..., x_{N-1}, y_{N-1}]^T. \tag{4.1}$$

This space discretization results into $N-1$ edge vectors: $\mathbf{e}^0, ..., \mathbf{e}^{N-2}$, where $\mathbf{e}^i = \mathbf{x}_{i+1} - \mathbf{x}_i$, and $0 \leq i \leq N-2$. Hereafter, we use subscripts to denote quantities associated with the nodes, e.g., $\mathbf{x}_i$, and superscripts when associated with edges, e.g., $\mathbf{e}^i$. Based on this kinematic representation, the remainder of this section discusses the formulation of elastic energies, elastic forces, and the time-stepping procedure of the rod system.

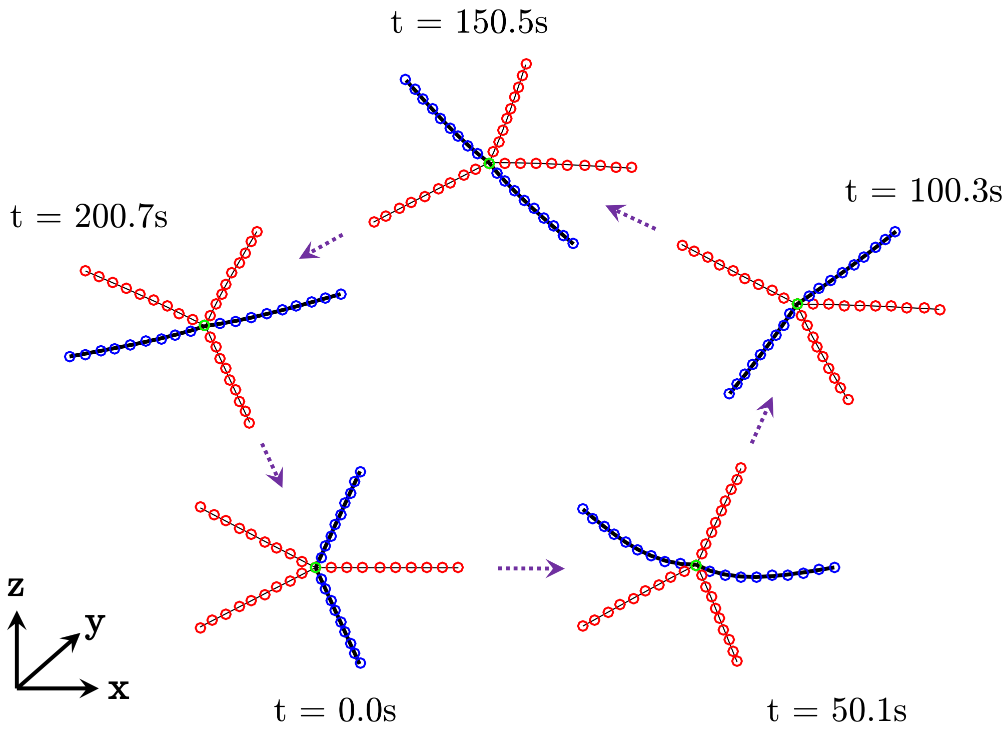

Figure 4.2: DER-based simulation of a seastar-inspired soft robot with pentagonal trajectory. The blue bold lines are the actuated limbs.

An elastic rod is modeled as a mass-spring system, with a lumped mass at each node. Associated with each node and edge is a discrete bending and stretching energy, respectively. In the case of a 3D rod, we would also have to account for the elastic twisting energy and related rotational inertia. For a rod with a constant Young's modulus E, cross section area A, and second moment of inertia I, the elastic stretching energy associated with the i th edge is

$$E_s^i = \frac{1}{2} EA(\epsilon^i)^2 \|\bar{\mathrm{e}}^i\|, \tag{4.2}$$

where $\epsilon^i = \|\mathrm{e}^i\|/\|\bar{\mathrm{e}}^i\| - 1$ is the axial strain of the i th edge, and the notation with bar on top indicates the quantity evaluated in undeformed configuration, e.g., $\|\bar{\mathrm{e}}^i\|$ is the undeformed length of the i th edge.

The bending energy of the i th node is measured by the misalignment between two

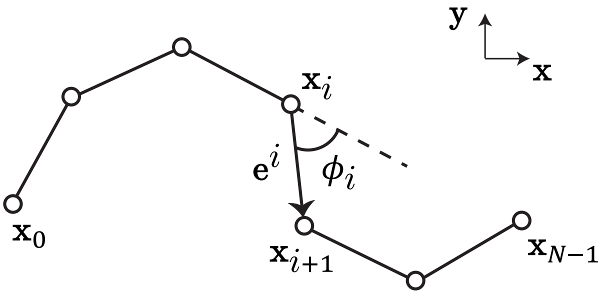

Figure 4.3: Schematic of a discrete rod in 2D.

consecutive edges $\{\mathbf{e}^{i-1}, \mathbf{e}^i\}$, i.e.,

$$E_{b,i} = \frac{1}{2} EI(\kappa_i - \bar{\kappa}_i)^2 \Delta l_i, \tag{4.3}$$

where $\kappa_i = 2\tan(\phi_i/2)/\Delta l_i$ is the discrete curvature at the i th node and $\Delta l_i = (\|\bar{\mathbf{e}}^{i-1}\| + \|\bar{\mathbf{e}}^i\|)/2$ is its Voronoi length. The turning angle ϕ_i is

$$\phi_i = \tan^{-1} \frac{(\mathbf{e}^{i-1} \times \mathbf{e}^i) \cdot \hat{\mathbf{n}}_z}{\mathbf{e}^{i-1} \cdot \mathbf{e}^i}, \tag{4.4}$$

where $\hat{\mathbf{n}}_z$ is the unit vector along the z-axis, i.e., the numerator on the right-hand side is the z-component of the cross-product between $\mathbf{e}^{i-1}$ and $\mathbf{e}^i$. Note that ϵ^i, κ_i, and ϕ_i represent the finite difference approximations of stretch, curvature, and turning angle.

The total potential energy of the rod system is obtained by summing the elastic stretching energies over all the edges and bending energies over all the nodes (except the first and the last nodes where the bending energies are always zero), i.e.,

$$E = \sum_{i=0}^{N-2} E_s^i + \sum_{i=1}^{N-2} E_{b,i}. \tag{4.5}$$

Next, the internal elastic force vector $\mathbf{F}^{\text{int}}$ is the negative gradient of the total potential energy:

$$\mathbf{F}^{\text{int}} = -\frac{\partial E}{\partial \mathbf{q}}. \tag{4.6}$$

Specifically, the non-zero force component of the i th node, $[F_{2i}^{\text{int}},\ F_{2i+1}^{\text{int}}]^T$, is only related to five neighboring energy terms: $E_s^{i-1}, E_s^i, E_{b,i-1}, E_{b,i}$ and $E_{b,i+1}$. We have

$$F_{2i}^{\text{int}} = -\frac{\partial}{\partial x_i}\left(E_s^{i-1} + E_s^i + E_{b,i-1} + E_{b,i} + E_{b,i+1}\right) \quad \text{and} \tag{4.7a}$$

$$F_{2i+1}^{\text{int}} = -\frac{\partial}{\partial y_i}\left(E_s^{i-1} + E_s^i + E_{b,i-1} + E_{b,i} + E_{b,i+1}\right) \tag{4.7b}$$

Next, we turn to the formulation of the external force vector. The external force is comprised of the force from the external environment, e.g., gravity, damping force from a viscous medium [3], or the actuation force from an external electromagnetic field [64]. Here, we consider the hydrodynamic force from fluid experienced by soft robotic limbs as the external force in our numerical framework. The discretized version of a fluid drag force applied on the i th node is [65, 66]

$$\mathbf{F}_i^{\text{ext}} = -\frac{1}{2}\rho_f C_d D \|\mathbf{v}_i\| \mathbf{v}_i \Delta l_i, \tag{4.8}$$

where ρ_f is the density of fluid medium, D is the diameter of the rod, C_d is the drag coefficient, and $\mathbf{v}_i \equiv [\dot{x}_i, \dot{y}_i]^T$ is the relative velocity of the i th node and fluid. The external force vector (size $2N$) on the entire rod is $\mathbf{F}^{\text{ext}} = \left[\mathbf{F}_0^{\text{ext}},\ \mathbf{F}_1^{\text{ext}},\ \ldots, \mathbf{F}_{N-1}^{\text{ext}}\right]^T$.

Finally, we discuss the time-marching scheme. We update the equations of motion of a discrete rod system by a first order, implicit Euler method, because of its unconditional convergence and numerical stability. We solve the following $2N$ equation of motions and update the DOF vector $\mathbf{q}$ and its velocity (time derivative of DOF) $\mathbf{v} = \dot{\mathbf{q}}$ from time step t_k to $t_{k+1} = t_k + h$ (h is the time step size) based on the following statement of force balance:

$$\mathbf{f} \equiv \mathbb{M}\frac{[\mathbf{q}(t_{k+1}) - \mathbf{q}(t_k) - h\mathbf{v}(t_k)]}{h^2} - \mathbf{F}^{\text{int}}(t_{k+1}) - \mathbf{F}^{\text{ext}}(t_{k+1}) = \mathbf{0}, \tag{4.9}$$

where $\mathbb{M}$ is the diagonal mass matrix comprised of the lumped masses, $\mathbf{F}^{\text{int}}$ is the internal elastic force given by Eqs. (4.6), $\mathbf{F}^{\text{ext}}$ is the external force formulated in Eq. (4.8), and t_k denotes evaluation of the quantity at time t_k.

We use the Newton-Raphson method to solve this set of nonlinear equations of motion. At each time step t_{k+1}, we first guess a new solution on the basis of the previous state, i.e.,

$$\mathbf{q}^{(1)}(t_{k+1}) = \mathbf{q}(t_k) + h\mathbf{v}(t_k). \tag{4.10}$$

Then, we optimize the solutions by gradient decent, such that the new solution at the $(k+1)$ th step is

$$\mathbf{q}^{(n+1)}(t_{k+1}) = \mathbf{q}^{(n)}(t_{k+1}) - \mathbb{J}^{(n)} \backslash \mathbf{f}^{(n)}, \tag{4.11}$$

where $\mathbb{J}$ is the Jacobian matrix associated with Eq. (4.9),

$$\mathbb{J} \equiv \frac{\partial \mathbf{f}}{\partial \mathbf{q}} = \frac{1}{h^2}\mathbb{M} + \frac{\partial^2 E}{\partial \mathbf{q} \partial \mathbf{q}} - \frac{\partial \mathbf{F}^{\text{ext}}}{\partial \mathbf{q}}. \tag{4.12}$$

A detailed formulation of Hessian matrix associated with the elastic energy, i.e., the second term $\partial^2 E / \partial \mathbf{q}^2$ in Eq. (4.12), is in [28]. The Jacobian associated with the external force, $\frac{\partial \mathbf{F}^{\text{ext}}}{\partial \mathbf{q}}$, can be re-written as $\frac{1}{h}\frac{\partial \mathbf{F}^{\text{ext}}}{\partial \mathbf{v}}$ and trivially computed from Eq. (4.8). Importantly, the Jacobian $\mathbb{J}$ is a banded matrix and the time complexity of this algorithm is $O(N)$ for a single rod system (the computational time linearly scales with the number of node). This computational efficiency has motivated its application in the animation industry (e.g., hair simulation for movies) as well as its adoption in mechanical engineering.

4.3 Results

Here, the main steps of the algorithm for modeling the dynamics of a soft swimming robot with the DER method are outlined below. We first introduce the geometric discretization of the seastar-inspired soft robot composed of a number of SMA-based actuators. Next, the modeling of the actuators is discussed, followed by a discussion on the locomotion of the seastar-inspired soft robot in two special cases: a straight path and a regular pentagonal trajectory. Finally, the computational efficiency of the DER-based numerical framework is detailed.

In Fig. 4.4(a), we model the seastar-inspired soft robot with five planar elastic rods

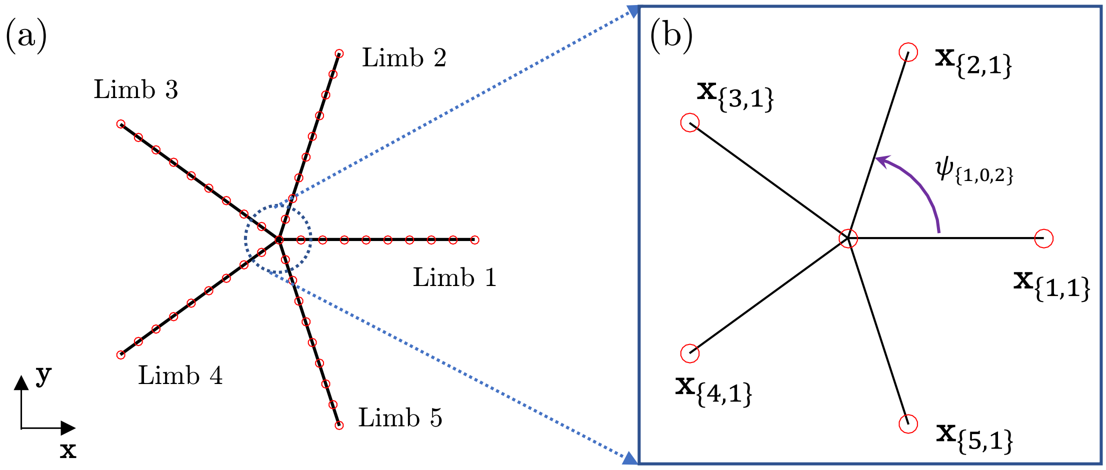

Figure 4.4: (a) Geometric discretization of seastar-inspired soft robot. (b) Zoomed-in description of the center point.

connected at the center point, $\mathbf{x}_0 \equiv [x_0, \; y_0]^T$. Each limb, with arc length $L = 0.1$m, is discretized into N nodes and $N-1$ edges. In the current study, we choose $N = 10$, resulting in an edge length of $\Delta L \approx 1.11$cm. As all five limbs share the center node, $\mathbf{x}_0$, the total number of nodes in the soft robot system is $n = 5 \times N - 4$. The i th node on j th limb is denoted as $\mathbf{x}_{\{j,i\}}$. The material properties used in this numerical study are as follows: Young's modulus $E = 1$MPa, material density $\rho_m = 1000$kg/m^3, fluid density $\rho_f = \rho_m$ (neutrally buoyant), rod radius $r_0 = 1.6$mm (and, therefore, second moment of inertia $I = \pi r_0^4/4$ and cross sectional area $A = \pi r_0^2$), and drag coefficient $C_d = 1.0$.

Besides the bending and stretching energies formulated in the DER method for each limb, the bending energy at the center node requires special treatment. As shown in Fig. 4.4(b), the bending energy between the first limb and second limb at the center node is

$$E_{b,\{1,0,2\}} = \frac{1}{2} EI \left(\kappa_{\{1,0,2\}} - \bar{\kappa}_{\{1,0,2\}} \right)^2, \tag{4.13}$$

where $\kappa_{\{1,0,2\}}$ is measured by the angle between the first limb and second limb, $\psi_{\{1,0,2\}}$. Similarly, there are four more components to the bending energy at the center node associated with the angles $\psi_{\{2,0,3\}}$, $\psi_{\{3,0,4\}}$, $\psi_{\{4,0,5\}}$, and $\psi_{\{5,0,1\}}$. Overall, the total elastic energy of seastar-inspired soft robot system is

$$E_{\text{total}} = \sum_{j=1}^{5} \left[\left(\sum_{i=0}^{N-2} E_s^i \right)_j + \left(\sum_{i=1}^{N-2} E_{b,i} \right)_j \right] \tag{4.14a}$$

$$+ E_{b,\{1,0,2\}} + E_{b,\{2,0,3\}} + E_{b,\{3,0,4\}} + E_{b,\{4,0,5\}} + E_{b,\{5,0,1\}}. \tag{4.14b}$$

Its first gradient (minus internal force) and second gradient (Hessian matrix) can be analytically formulated in a manner similar to common applications of the DER methods.

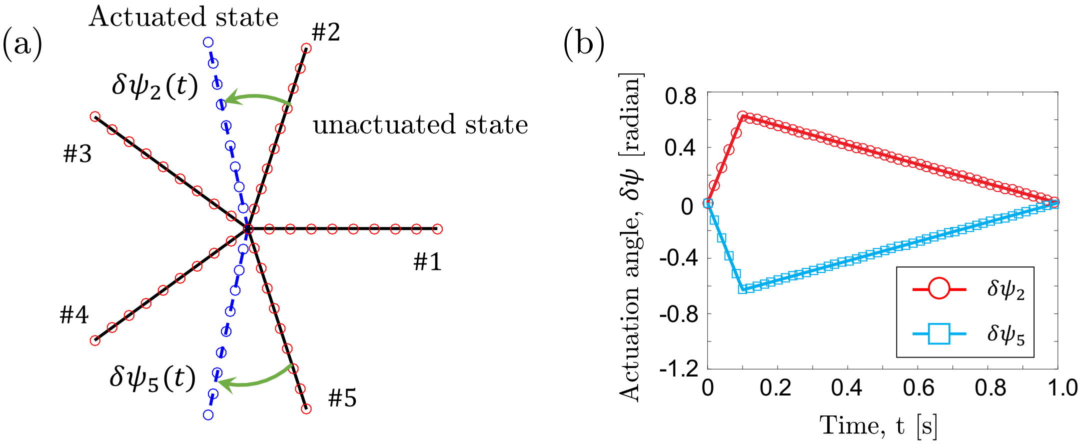

Figure 4.5: (a) Actuated and unactuated state of seastar-inspired robot. (b) Actuation signal of #2 and #5 limbs: rotating angle, $\delta\psi$, as a function of time during one actuation cycle.

Actuation is incorporated into the simulation by varying the natural curvature between two neighboring limbs, e.g., $\bar{\kappa}_{\{1,0,2\}}$ in Eq. (4.13), with time. This variation is measured through characterization of a single SMA-powered actuator, as described next. The electrically-activated SMA wire enables rapid transition between the unactuated state and the actuated state [54, 67]. Assume the limbs can rotate by a certain angle as a function of time during the actuating-cooling process, e.g., #2 rotates by an angle $\delta\psi_2(t)$ relative to the rest of the system, as shown in Fig. 4.5(a). We define anti-clockwise rotation as positive and clockwise rotation as negative.

Usually, experimental characterization of an actuator can be used to get the actuation function, e.g., $\delta\psi_2(t)$. Here, for simplicity, we assume a piecewise linear function, shown

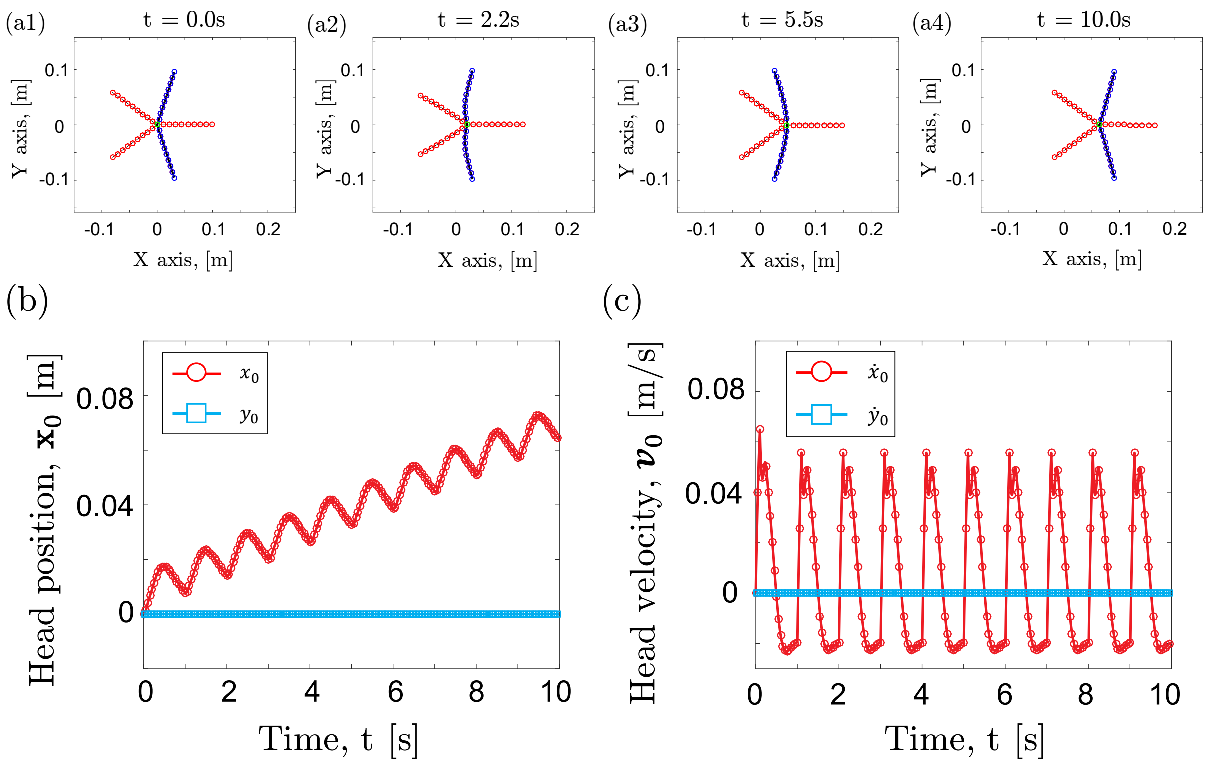

Figure 4.6: (a1)-(a4) Snapshots of swimming seastar-inspired robot at different time step, $t = 0.0$s, 2.2s, 5.5s, and, 10.0s. (b) Head node position as a function of time. (c) Head node velocity as a function of time.

in Fig. 4.5(b), to describe the actuated and cooling state. We actuated $\#2$ and $\#5$ limbs simultaneously for the straight locomotion along X-axis, and the maximum actuation angle is $\pi/5$, which is half of the angle between two neighboring limbs in the undeformed configuration. The actuation period in Fig. 4.5(b) is $\Delta t_0 = 1.0$s, with actuating time $\Delta t_1 = 0.1$s and cooling time $\Delta t_2 = 0.9$s.

By symmetrically actuating $\#2$ and $\#5$ limbs with the input shown in Fig. 4.5(b), this bio-inspired swimming robot can move forward along the X-axis. In Fig. 4.6(a1)-(a4), we show multiple snapshots of the seastar-inspired soft robot swimming in water at different time steps, $t \in \{0.0, 2.2, 5.5, 10.0\}$s. We observe that the robot swims forward during the actuating phase, but moves slightly backward in the cooling state. Overall, the net motion of the robot is forward over an entire cycle. Figs. 4.6(b) and (c) show the center node position and velocity, respectively, as functions of time over 10 actuation periods. Because of the symmetry of geometric and actuating conditions, this bio-inspired soft robot has no displacement and velocity components along the Y-axis.

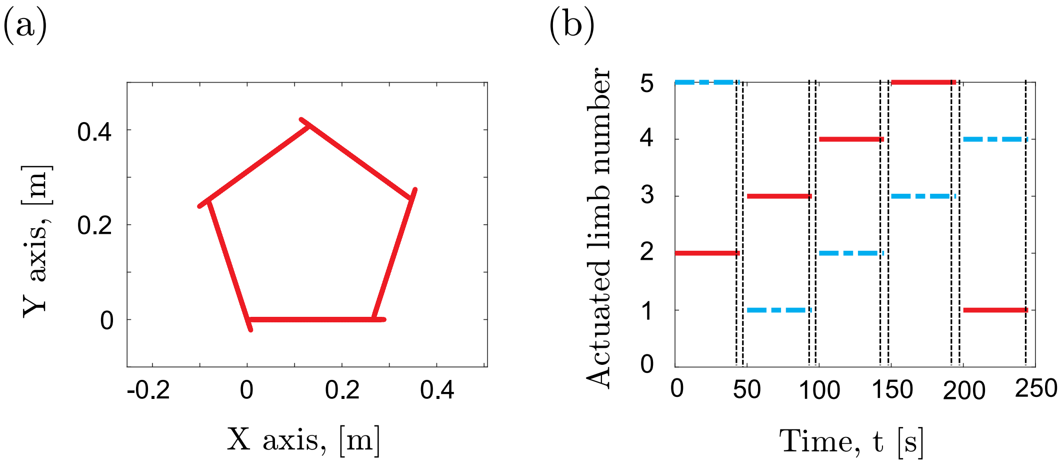

Figure 4.7: (a) Regular pentagon trajectory of seastar-inspired soft robot. (b) Actuation input signal for regular pentagon trajectory. Blue dashed line: negative rotating actuation; red solid line: positive rotating actuation.

Next, we show a nonlinear trajectory of the robot swimming in a fluid medium. The soft robot can follow a straight trajectory along one limb by actuating two neighboring limbs next to it, e.g., the soft robot can swim along X-axis (the direction of $\#1$ limb) by actuating $\#2$ and $\#5$ limbs, as discussed in the previous case. A complex nonlinear trajectory, on the other hand, can be achieved by combining multiple straight trajectories that are not parallel. In Fig. 4.2, we provide some snapshots of seastar-inspired soft robot moving along a prescribed regular pentagonal trajectory, i.e., a closed path that combines five straight trajectories. Fig. 4.7(a) shows the trajectory traced by the center node. Here, we actuated two limbs at a time for each straight line segment. For the presented pentagonal trajectory in the current study, the actuation sequence of the limbs are

$$\{2,5\}\,;\ \{1,3\}\,;\ \{2,4\}\,;\ \{3,5\}\,;\ \{1,4\}\,, \tag{4.15}$$

as shown in Fig. 4.7(b), and the actuating function for each limb is in Fig. 4.5(b). During each straight path, we actuated two specific limbs in Eq. (4.15) for 45s, then left the limbs unactuated for 5s in order to bring the robot to a complete stop. This way, we maintained the same initial conditions for each straight component of the pentagonal trajectory.

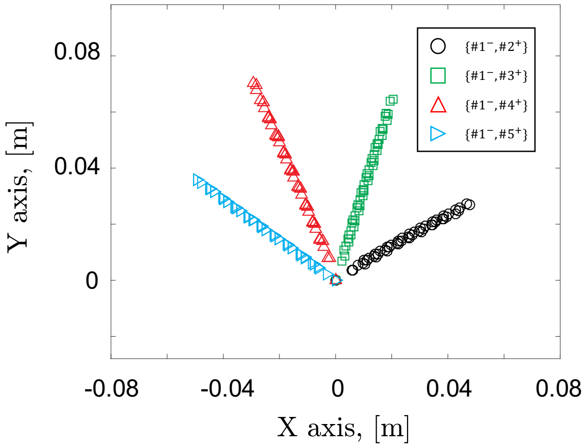

Figure 4.8: Trajectories of seastar-inspired soft robot when actuating through different combinations of limbs over 10 actuation periods.

Previous investigations mainly focus on a specific actuating condition. Here, exploiting the efficiency and robustness of our simulator, we perform different actuating combinations of soft limbs. In Fig. 4.8, we plot the trajectories of the seastar-inspired soft robot with different actuated limbs, i.e., $\{1^-, 2^+\}, \{1^-, 3^+\}, \{1^-, 4^+\}, \{1^-, 5^+\}$, over 10 actuation periods. Here, the positive indicates the anti-clockwise rotation and the negative indicates the clockwise rotation, similar to the previous study. The seastar-inspired soft robot always moves along the bisector of the two actuated limbs, while the translation distance is different. The maximum translation is obtained when actuated $\#1$ and $\#4$ limbs simultaneously, while the actuating combination of $\#1$ and $\#2$ limbs have a lower efficiency. Overall, any desired nonlinear trajectory can be fitted by a zig-zag path constituted some simple straight lines described above.

Finally, we highlight the computational efficiency of the DER-based soft robotic simulation. For the case of the seastar-inspired swimmer, this numerical framework can achieve real-time simulation speed in which the time required to perform the computation is equal to or faster that the duration of the physical motion being modeled. In Fig. 4.9, with a fixed number of nodes, $N = 46$, the computational time linearly scales with time step size, h. The simulations ran on a single thread of AMD Ryzen 1950X CPU @ 3.4 GHz. The simulator can run faster than real time when the time step size $h \gtrsim 3.0\text{ms}$. Numerical issues associated with large step size appears at $h \gtrsim 20\text{ms}$.

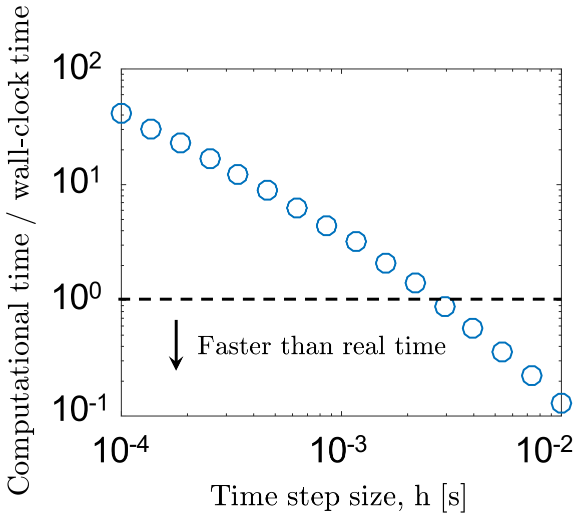

Figure 4.9: The ratio between computational time and wall-clock time as a function of time step size, h, with a fixed number of vertices, $n = 46$.

4.4 Summary and Outlook

We have introduced a computational framework to study the dynamics of seastar-inspired soft robot that is adapted from methods popular in the computer graphics community. This numerical framework integrates elasticity of slender structures, actuation of shape memory alloy, and hydrodynamic loading for fluid-structure interaction, to achieve fast prediction of the motion of seastar-inspired soft robot swimming in fluid medium. In particular, the DDG-based method presented here can quantitatively predict the robot's motion while running faster than real time on one thread of a contemporary desktop processor. The computational efficiency of this method makes it ideally suited for algorithms that iterate over a wide variety of parameters in order to select a robot with optimized design. Moving forward, it would be interesting to apply this method to simulate limbed locomotion of soft robots in 3D. This includes the untethered quadruped in [67] as well as the soft SMA-powered robots presented in [33]. Future efforts could also explore the development of a data-driven based trajectory plan algorithm for the motion control of bio-inspired soft robots. Such an algorithm would combine rapid, DDG-based simulation of robots with training data for mechanical and fluid-structure interactions obtained from empirical measurements and sensor feedback.

CHAPTER 5

Buckling Instability for Directional Control in Flagellar Propulsion

In this chapter, we will couple the elasticity of a slender rod with hydrodynamic loading at a low Reynolds fluid in the context of uniflagellar bacteria and bio-inspired soft robots, then control its swimming direction by exploiting buckling instability in its helical flagellar. Our model system is comprised of a spherical rigid head and a helical elastic flagellum. The rotation of the flagellum in low Reynolds environment generates a propulsive force that allows the system to swim in fluid. The locomotion is an intricate interplay between the elasticity of the flagellum, the hydrodynamic loading, and the flow generated by the moving head. We use the Discrete Elastic Rods (DER) algorithm to capture the geometrically nonlinear deformation in the flagellum, Lighthill's Slender Body Theory to simulate the hydrodynamics, and Higdon's model for the spherical head in motion within viscous fluid. This flagellated system follows a straight path if the angular velocity of the flagellum is below a critical threshold. Buckling ensues in the flagellum beyond this threshold angular velocity and the system takes a nonlinear trajectory. We consider the angular velocity as the control parameter and solve the inverse problem of computing the angular velocity, that varies with time, given a desired nonlinear trajectory. Our results indicate that bacteria can exploit buckling in flagellum to precisely control their swimming direction.

We describe the underlying motivation and relevant literatures in § 5.1. The numerical simulation procedure is detailed in § 5.2. The buckling instability of helical filament and a data-driven approach for the trajectory design are in § 5.3. We conclude a summary and point out potential directions for future research in § 5.4. The content of this chapter has appeared in Ref. [68].

5.1 Motivation

A primary mode of locomotion in bacteria is the rotation of a single helical flagellum in a fluid medium [9]. A flagellum – typically several microns in length and a few nanometers in cross-sectional radius [9] – is effectively an elastic rod, and the fluid flow – at the length and time scales of bacterial locomotion – is in the Stokes regime (Reynolds number $\ll 1$) [69]. A non-trivial coupling between the geometrically nonlinear deformation in the flagellum and the hydrodynamics of the low Reynolds flow leads to a number of hallmarks of flagellar propulsion, e.g., tumbling [10], turning [11], bundle formation [70], and polymorphic transformations [71]. Previous investigations involving both experiments [11, 72] and simulations [3, 13] show that the hydrodynamic force can lead to buckling in the flagellum or in the soft connector between the flagellum and the cell body [73, 74]. In this article, we assume that the connector and the flagellum are made of the same material; this assumption simplifies the system and makes the design of bio-inspired robot easier to fabricate. We seek to understand how buckling of soft flagellum can be exploited to precisely steer the swimming direction. We are also motivated by revolutionary advances in flagellated micro-robots [75] and the potential application of the steering by buckling mechanism in the control of such robots. Bacteria-inspired flagellated robots are typically controlled by external magnetic field [76, 77], electric field [78], acoustic excitation waves [79, 80], and chemically powered propulsion [81]. As a result, their manufacturing process often involves advanced specialized materials, e.g., ionic polymer-metal composites [82]. Buckling, on the other hand, can be induced in any elastic material simply by changing a single scalar variable – the rotational speed of the flagellum [3].

The propulsion of a uniflagellar system (bacteria or robot) can be divided into three components: (1) elasticity of the flagellum, (2) hydrodynamic flow by the flagellum, and (3) hydrodynamics of the head. Prior works [3] showed that Kirchhoff elastic rod [83] – as a model for the flagellum – and Lighthill's slender body theory (LSBT) [15] – as the hydrodynamic force model – can accurately describe the dynamics of a flexible flagellum in a viscous medium, including the buckling instability [84, 85]. The role of a head, the flow generated by its motion, and its coupling with the flow generated by the flagellum, were not explored in these studies. Thawani et al. [86] incorporated the effect of the head on the locomotion of a model uniflagellar bacterium; however, the flagellum was assumed to be rigid. We seek to bridge this gap and incorporate all the three aforementioned components to demonstrate that the buckling instability can be used by the uniflagellar system to follow a prescribed 3D trajectory.

In this numerical study, we consider a model system comprised of a rigid spherical head and a rotating flexible flagellum in a viscous medium at low Reynolds number. The flagellum is treated as an elastic rod and modeled using the Discrete Elastic Rods (DER) [27, 28] algorithm – a numerical method developed in the computer graphics community for visually dramatic simulation of hair, fur, and other filamentary structures. The hydrodynamic force applied by the surrounding medium on the flagellum is modeled using LSBT that can capture the long range hydrodynamic interaction between flows generated by distant parts of the structure. The hydrodynamics of the spherical head is included in the framework following Higdon's model [87]. These three ingredients – DER, LSBT, and Higdon's model – in concert form a numerical framework that seamlessly captures the geometrically nonlinear deformation in the flagellum. Exploiting the computational efficiency of the framework, DER in particular, we systematically explore parameter space to quantify the change in swimming direction resulting from buckling instability. We demonstrate that the swimming direction can be controlled simply by changing a single scalar input – the angular velocity of the flagellum. While the numerical tool is general enough to include a hook – a soft joint between the head and the flagellum [88], we do not include it in our numerical exploration and, instead, focus on the most simple system of a head and a single flagellum that can follow any desired trajectory. This study indicates that uniflagellar bacteria can apply buckling in flagella to turn. It also provides a blueprint for self-contained soft robots, particularly suited for the micro-meter scale due to the assumption of low Reynolds number.

5.2 Fluid-Structure Interactions

The simulation of fluid-structure interaction of flagellar robot combines three components: (i) DER that simulates the flexible flagellum as a linear elastic rod [27, 28], (ii) LSBT that models the force exerted by the viscous flow on the flagellum [15], and (iii) Higdon's model [87] for flow generated by the spherical head.

5.2.1 Geometry of Flagella Soft Robot

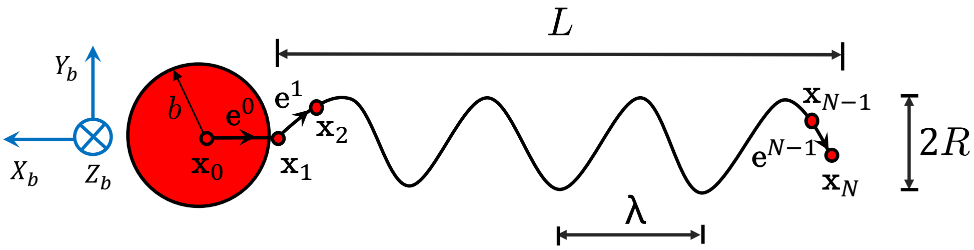

Figure 5.1: Geometry of a flagella-inspired soft robot.

The system has two parts shown schematically in Fig. 5.1 – a rigid spherical head and a soft helical flagellum. The physical parameters are: helix pitch $\lambda = 32.6$ mm, helix radius $R = 6.04$ mm, axial rod length $L = 13$ cm, (resulting in a contour length $l =$ 20cm), rod radius $r_0 = 1$ mm (and, therefore, second moment of inertia $I = \pi r_0^4/4$, polar moment of inertia $J = \pi r_0^4/2$, and cross sectional area $A = \pi r_0^2$), Young's modulus $E = 10$ MPa, shear modulus $G = E/3$ (assuming incompressible material), and material density $\rho_r = 1.273\text{g/cm}^3$. The radius of head is $b = 1.2$cm. The viscosity of the fluid is $\mu = 2.7$ Pa·s, and its density ρ_m is the same as the rod density ρ_r. Overall, the system is neutrally buoyant. The Reynolds number in the current study is $\rho_r \omega R r_0/\mu \leq 4 \times 10^{-2}$, i.e., always in the Stokes limit [89]. These physical parameters were chosen partly based on prior experimental works [3, 89].

5.2.2 Hydrodynamic Model for Soft Filament

We use LSBT to model the viscous drag experienced by a slender filament in motion within a low Reynolds environment and implement this as the external force $\mathbf{F}^{\text{ext}}$. Previous studies have already successfully coupled DER algorithm and LSBT to show the buckling instability of helical rods rotating in viscous fluid and compared the numerical results against experiments [3, 89]. In this section, we review the LSBT-DER implementation.

The velocity at each node on the rod is equal to the fluid velocity at that point (no-slip boundary condition). The velocity at the j-th node on the flagellum is $\mathbf{u}_j \equiv \left[\dot{\mathbf{q}}_{4j}, \dot{\mathbf{q}}_{4j+1}, \dot{\mathbf{q}}_{4j+2}\right]^T$; recall that $\dot{\mathbf{q}}$ is the $4N-1$ sized velocity vector of the DOFs. This nodal velocity $\mathbf{u}_j$ can be decomposed into two components: (i) a flow velocity $\left(\mathbf{u}_f\right)_j$ that is generated by the force exerted by the flagellum onto the fluid (equal and opposite to the hydrodynamic force on the flagellum), and (ii) another flow velocity $\left(\mathbf{u}_h\right)_j$ that is induced by the motion of the head. For the first component, we use LSBT to relate the velocity $\left(\mathbf{u}_f\right)_j$ and the hydrodynamic force on the flagellum.

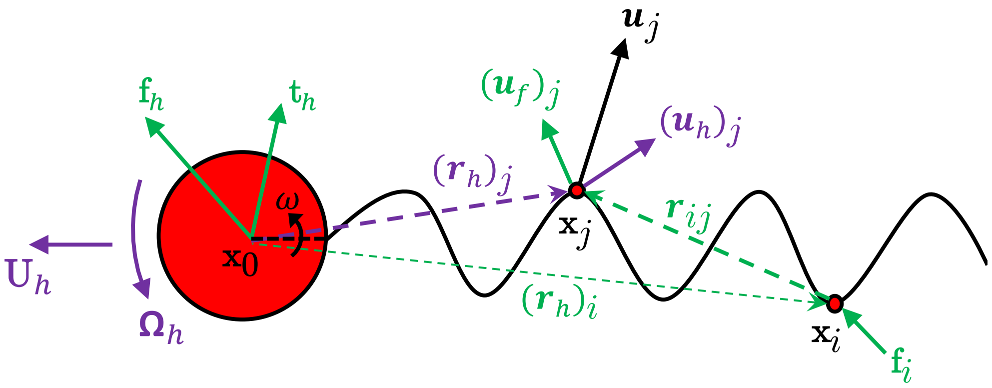

Figure 5.2: Interaction between the head and the filament in a viscous fluid.

Due to the linearity of the Stokes equations for low Reynolds number flow [90, 91], LSBT assumes a series of Stokeslets and dipoles along the centerline of rod, and builds a relationship between the velocity field contributed by the flagellum with the hydrodynamic force applied on it. In the discrete setting, that relation is [3]

$$-\left(\mathbf{u}_f\right)_j = \frac{\left(\mathbf{f}_j\right)_\perp}{4\pi\mu(2\delta)} + \sum_{i=1, i\neq j}^{N-1} \frac{1}{8\pi\mu \|\mathbf{r}_{ij}\|} \left[\mathbb{I} + \hat{\mathbf{r}}_{ij} \otimes \hat{\mathbf{r}}_{ij}\right] \mathbf{f}_i, \tag{5.1}$$

where $\mathbf{f}_i \equiv \left[\mathbf{F}^{\text{ext}}_{4i}, \mathbf{F}^{\text{ext}}_{4i+1}, \mathbf{F}^{\text{ext}}_{4i+2}\right]^T$ is the external force at the i-th node, $\left(\mathbf{f}_j\right)_\perp = \left(\mathbb{I} - \mathbf{t}_j \otimes \mathbf{t}_j\right) \mathbf{f}_j$ is the projection of $\mathbf{f}_j$ in the plane perpendicular to the tangent $\mathbf{t}_j$ at the j-th node, $\mathbb{I}$ is the identity tensor, $\otimes$ denotes the tensor product, $\mathbf{r}_{ij}$ is the position vector from the i-th to the j-th node, $\hat{\mathbf{r}}_{ij}$ is the unit vector along $\mathbf{r}_{ij}$, and $\delta = r_0\sqrt{e}/2$ is the natural cutoff length (r_0 is the radius of the circular cross-section of the rod and e is the Napier's constant). The node-based tangent, $\mathbf{t}_j$, is computed from the average of the preceding and following edge vectors such that $\mathbf{t}_j = \frac{1}{2}\left(\mathbf{t}^{j-1} + \mathbf{t}^j\right)$, where $\mathbf{t}^j$ (and $\mathbf{t}^{j-1}$) is the unit vector along the j-th (and $j-1$-th) edge. While $\delta = r_0\sqrt{e}/2$ has been commonly used in prior works [86, 3], recent studies suggest that this value can be tuned to achieve the most accurate solution [92]. However, in the model setup used in this study, the buckling threshold does not strongly depend on the value of δ. This discrete formulation of LSBT requires that the length of each edge be 2δ, resulting in a total node number of $N = 122$ in our model system.

Using Eq. (5.1), a linear system can be formed to describe the relationship between the velocity and the hydrodynamic forces:

$$\mathbf{U}_f = \mathbb{A}\mathbf{F}, \tag{5.2}$$

where the velocity vector, $\mathbf{U}_f \equiv \left[(\mathbf{u}_f)_1, (\mathbf{u}_f)_2, \ldots (\mathbf{u}_f)_{N-1}\right]$, and the hydrodynamic force vector, $\mathbf{F} \equiv [\mathbf{f}_1, \mathbf{f}_2, \ldots, \mathbf{f}_{N-1}]$, both have size $3(N-1)$. The matrix $\mathbb{A}$, with size $3(N-1) \times 3(N-1)$, depends on the geometry of the flagellum and can be evaluated from Eq. (5.1). Of the total N nodes, the first one is the head and will be treated in the next section.

Knowing the velocity field, $\mathbf{U}_f$, generated by the flagellum and the matrix $\mathbb{A}$, the viscous drag force, $\mathbf{F}$, along the centerline can be computed using Eq. (5.2). This force is then used as the external force in the equations of motion. To avoid numerical issues while solving this inverse problem in Eq. (5.2), we assume that the force varies smoothly along the arc-length of the rod. Details of this algorithm can be found in a previous work [89].

5.2.3 Interplay Between Head and Filament in a Viscous Fluid

LSBT provides a formulation for the hydrodynamic flow generated by the flagellum and the viscous drag force. However, the flow generated by the head and the hydrodynamic forces on it have not been considered. Here, we discuss the interaction between the rigid spherical head and the soft flagellum in viscous fluid environment.

We first formulate the flow generated by the moving spherical head with radius b. In Fig. 5.2, we consider a rigid head with a translation velocity, $\mathbf{U}_h \equiv [\dot{\mathbf{q}}_0, \dot{\mathbf{q}}_1, \dot{\mathbf{q}}_2]$, and angular velocity, $\mathbf{\Omega}_h$ (along $\hat{x}_b$). The viscous flow at the j-th node from the spherical head is given by Higdon's model [87, 86],

$$(\mathbf{u}_h)_j = \frac{b^3}{(r_h)_j^3}(\mathbf{r}_h)_j \times \mathbf{\Omega}_h + \frac{3}{4}b\left[\left(\frac{\mathbb{I}}{(r_h)_j} + \frac{(\mathbf{r}_h)_j \otimes (\mathbf{r}_h)_j}{(r_h)_j^3}\right) + \frac{b^2}{3}\left(\frac{\mathbb{I}}{(r_h)_j^3} - \frac{(\mathbf{r}_h)_j \otimes (\mathbf{r}_h)_j}{(r_h)_j^5}\right)\right] \cdot \mathbf{U}_h, \tag{5.3}$$

where $(\mathbf{r}_h)_j$ is the position vector of the j-th node relative to the center of the head, $(r_h)_j = ||(\mathbf{r}_h)_j||$, and $\times$ notation is the cross product. As a reminder, when combining equations Eq. (5.1) and Eq. (5.3), the actual velocity at the j-th node is $\mathbf{u}_j = (\mathbf{u}_f)_j + (\mathbf{u}_h)_j$ (no-slip boundary condition).

Next we model the viscous drag experienced by the moving head. The hydrodynamic force applied on the head is also comprised of two parts: (i) drag force $-6\pi\mu b \mathbf{U}_h$ (and torque $-8\pi\mu b^3 \mathbf{\Omega}_h$) caused by its own motion, and (ii) the force from the Stokeslets on the flagellum. Because of the long range hydrodynamic interaction in viscous environment, the Stokeslets on the flagellum also contribute force and torque to the spherical head [87, 86],

$$\mathbf{f}_h = \sum_{i=1}^{N-1}\left[-\frac{3}{2}\frac{b}{(r_h)_i} + \frac{1}{2}\frac{b^3}{(r_h)_i^3}\right]\mathbf{f}_i + \frac{\mathbf{f}_i \cdot (\mathbf{r}_h)_i}{(r_h)_i^2}\left[-\frac{3}{4}\frac{b}{(r_h)_i} + \frac{3}{4}\frac{b^3}{(r_h)_i^3}\right](\mathbf{r}_h)_i, \tag{5.4}$$

$$\mathbf{t}_h = \sum_{i=1}^{N-1} -\frac{b^3}{(r_h)_i^3}(\mathbf{r}_h)_i \times \mathbf{f}_i, \tag{5.5}$$

where $(\mathbf{r}_h)_i$ is the position vector of the i-th node relative to the center of the head and its norm is $(r_h)_i = ||(\mathbf{r}_h)_i||$.

Note that, without considering the method of image [87], the presence of flow from the Stokeslets on the flagellum does not satisfy the no-slip boundary on the surface of the spherical head. Method of image assumes that there is an imaginary Stokeslet located inside the head, such that the sum of the flow exerted by the real Stokeslet and the fake Stokeslet can ensure the no-slip boundary on the spherical surface [87]. However, the error can be small when compared with experimental data if the fake Stokeslets are ignored [86].

5.2.4 Numerical Simulation Procedure

At this point, we have all the pieces to build a framework to capture the coupling of DER, LSBT, and moving head. At each time step t_k, we know the DOF vector $\mathbf{q}_k$, its velocity $\dot{\mathbf{q}}_k$, and the angular velocity of the head $(\mathbf{\Omega}_h)_k$. We first evaluate the flow generated by the head based on Eq. (5.3). Then the flow from the flagellum $\mathbf{U}_f$ can be obtained by subtracting the flow due to the head from the velocity of each node. Next, LSBT (Eq. (5.2)) is used to compute the external force $\mathbf{F}$ applied on the filament. The external force on the head can be obtained from

$$\mathbf{f}_0 = -6\pi\mu b \mathbf{U}_h + \mathbf{f}_h, \tag{5.6}$$

where $\mathbf{f}_h$ is given by Eq. (5.5). With the external force on both the spherical head and the elastic flagellum, we can compute $\mathbf{F}^{\text{ext}} \equiv [\mathbf{f}_0, 0, \mathbf{f}_1, 0, \mathbf{f}_2, ..., 0, \mathbf{f}_N]^T$ and use Newton's method to solve the equations of motion in rod system. This gives us the updated DOF vector $\mathbf{q}_{k+1}$ and the velocity $\dot{\mathbf{q}}_{k+1} = (\mathbf{q}_{k+1} - \mathbf{q}_k)/h$. Finally, the angular velocity of the head $(\mathbf{\Omega}_h)_{k+1}$ is updated from the torque balance of the entire structure,

$$-8\pi\mu b^3 \mathbf{\Omega}_h + \mathbf{t}_h + \sum_{i=1}^{N-1} \left[(\mathbf{r}_h)_i \times \mathbf{f}_i \right] = \mathbf{0}. \tag{5.7}$$

These quantities ($\mathbf{q}_{k+1}$, $\dot{\mathbf{q}}_{k+1}$, $(\mathbf{\Omega}_h)_{k+1}$) evaluated at time t_{k+1} are used in the next iteration to move from $t = t_{k+1}$ to $t = t_{k+2}$. The time step size used in the current work is $h = 1$ ms following a convergence study.

5.3 Results

5.3.1 Buckling Instability of Helical Filament

We use this numerical framework to systematically investigate the deformation and locomotion of the uniflagellar bacteria and robots in viscous fluid. We apply a Dirichlet boundary condition to specify the twisting angle on the first edge, θ^0, to perform the rotation of the soft filament at a prescribed angular velocity ω – the control parameter in this study. All other nodes and edges are free and evolve based on the balance between the elastic and external forces. The *motor speed* is the angular velocity of the flagellum relative to the angular velocity of the head, $\mathbf{\Omega}_h$. The rotation of the flagellum generates a propulsive force that moves the entire structure – the head and the flagellum – forward. At sufficiently small angular velocity in Fig. 5.3(a), the motion of the head, i.e., the position of the first node, traces a linear path, and the helical structural remains stable. However, the soft filament undergoes a buckling instability when the angular velocity ω exceeds a critical value and the swimming trajectory becomes highly nonlinear. A representative configuration of the flagellum upon buckling is shown in Fig. 5.3(b). A time-scale – $\mu L^4/EI$ – is obtained from the balance between bending force and viscous force [89], which can be used to normalize the angular velocity and time. Hereafter, overbar represents non-dimensional quantities, e.g., $\bar{\omega} = \omega\mu L^4/(EI)$ and $\bar{t} = tEI/(\mu L^4)$ are normalized angular velocity and normalized time, respectively.

To quantify the buckling angular velocity, $\bar{\omega}_b$, for application in trajectory design, we perform a parameter sweep along angular velocity to systematically study the mechanical response of the uniflagellar system in viscous fluid. In Fig. 5.3(c), we plot the normalized length, L'/L, as a function of the normalized angular velocity, $\bar{\omega}$, at different values of the head radius, where L' is the Euclidean distance between the first node and the last node, and L is the end-to-end distance in the undeformed configuration. In this parameter sweep, a flagellated system in rest position starts moving at a prescribed angular velocity and keeps that angular velocity constant for 100s (1.02 in normalized time) – a time sufficiently longer than the transient dynamics. The normalized length of the flagellum is measured at $\bar{t} = 1.02$. Regardless of the size of the head, we observe that, at small values of $\bar{\omega}$, the soft filament slightly stretches so that L'/L is above 1. There exists a critical value of angular velocity, $\bar{\omega}_b$, beyond which the helical structure undergoes buckling instability and deforms into a shape substantially different from its natural helical shape. The buckling direction is deterministic and the rotational symmetry is broken by the connection between the flagellum and the head. This buckling velocity, $\bar{\omega}_b$, is strongly influenced by the radius of the head, b: compared with the case where the effect of head is ignored ($b = 0.0$), different values of the head size, $b = \{0.4, 0.8, 1.2\}$ cm, reduces ω_b by 19%, 32%, and 40%, respectively. A physical explanation behind the trend of decreasing ω_b with increasing head size is provided next. If the angular velocity of the flagellum, ω, remains fixed, a larger head requires more propulsive force to overcome the drag and, therefore, the overall swimming velocity of the flagellated system decreases. As a result, the relative fluid velocity between the medium and the system along the axis of the flagellum ($-X_b$ in the body-fixed frame) decreases. Since a fluid flow along $-X_b$ direction resists buckling [93], a larger head brings about the buckling instability sooner, i.e., at a lower value of angular velocity.

We turn to another measure of the motion to explore the effect of instability in Fig. 5.3(d) and use the same data to plot the traversed displacement $||\mathbf{s}||$ – the Euclidean distance between the position of the head at $\bar{t} = 0$ and $\bar{t} = 1.02$ – as a function of angular velocity, ω. The distance $||\mathbf{s}||$ increases approximately linearly with angular velocity when $\bar{\omega} < \bar{\omega}_b$, and the flagellated system covers a straight path in this phase. This relation between $||\mathbf{s}||$ and $\bar{\omega}$ would be exactly linear in case of a rigid flagellum. Due to the flexibility of the flagellum, it deforms and slightly deviates from the linear displacement - angular velocity relationship. However, the distance covered, and as such the speed of the whole structure, depends on the radius of the head, b. Compared with the case without a head ($b = 0$), the traversed distance drops by 16%, 32%, and 43% at $b = \{0.4, 0.8, 1.2\}$ cm, respectively, when swimming at a constant angular velocity in this regime ($\bar{\omega} < \bar{\omega}_b$). On the other hand, the translational displacement $||\mathbf{s}||$ shows a nonlinear behavior when the angular velocity is beyond the threshold $\bar{\omega}_b$. This is due to the structural instability in the helical filament and the resulting nonlinear 3D trajectory.

Considering the potential application of this study in design of soft robots, we turn to the torque and power required by the flagellated system. Fig. 5.3(e) shows the normalized external torque, $\bar{T} = TL/EI$, applied by the head to maintain the rotation of the flagellum as a function of normalized angular velocity. We observe that the torque increases almost linearly with the angular velocity. Moreover, there is negligible variation in torque with

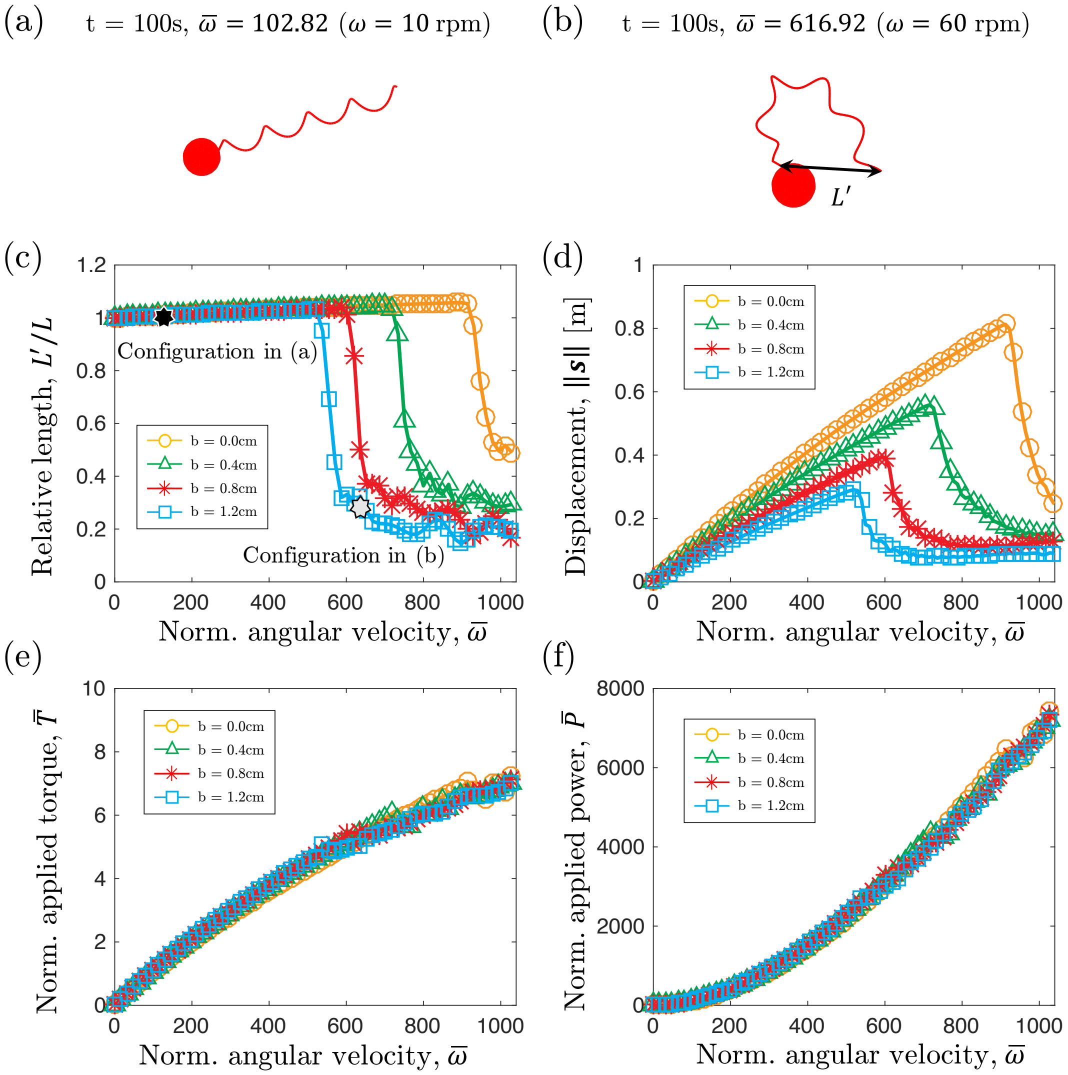

Figure 5.3: Configurations at normalized time $t = 100$ s ($\bar{t} = 1.02$): (a) stable configuration (with $\bar{\omega} = 102.82$); and (b) buckling configuration (with $\bar{\omega} = 616.92$). Relation between normalized angular velocity and (c) normalized length, L'/L at $\bar{t} = 1.02$; (d) translational displacement, $\|\mathrm{s}\|$, over $\bar{t} = 1.02$; (e) normalized external applied torque, $\bar{T} = TL/EI$; and (f) normalized external power $\bar{P} = \bar{T}\bar{\omega}$.

the size of the head, even though the swimming speed varies with the head radius. In Fig. 5.3(f), we plot the normalized power, $\bar{P} = \bar{T}\bar{\omega}$, as a function of $\bar{\omega}$. As expected from the data on torque vs. angular velocity, the required power increases quadratically with angular velocity.

5.3.2 Data-Driven Approach for Trajectory Design

Due to the existence of a critical angular velocity for buckling, $\bar{\omega}_b$, the flagellated system follows a straight line at $\bar{\omega} < \bar{\omega}_b$ and goes into a complex 3D trajectory at $\bar{\omega} > \bar{\omega}_b$. Based on this observation, we present a control policy for directional control of uniflagellar robots and bacteria. This far, the numerical framework computes the trajectory of the system given the physical parameters and the angular velocity, $\omega(t)$, as a function of time. We now turn to the inverse problem of computing the angular velocity, $\omega(t)$, – a single scalar input – given a prescribed 3D trajectory. The prescribed trajectory can be divided into a finite number of discrete line segments and, therefore, the path following process can be reduced to a simpler problem comprised of three parts: (i) initially the flagellated system goes along a straight line with an initial direction, $\mathbf{d}_0$, by rotating its flagellum at a low angular velocity ω_l (where $\omega_l < \omega_b$), and the traversed distance depends linearly on the running time of this lower angular velocity; (ii) when there is a misalignment between its initial direction $\mathbf{d}_0$ and the target direction $\mathbf{t}_1$ (see Fig. 5.4(a)), its angular velocity increases to ω_h (where $\omega_h > \omega_b$) and stays at that value for t_c seconds such that the helical filament undergoes buckling instability and the orientation changes; (iii) finally the angular velocity switches from ω_h to ω_l, the helical structure reshapes to the unbuckled state, and the flagellated system swims along a straight line with a new orientation, $\mathbf{t}_1$. By repeating these three phases, the uniflagellar system can cover a given 3D trajectory. The lower angular velocity for straight path used in this study – chosen rather arbitrarily – is $\omega_l = 10$ rpm ($\bar{\omega}_l = 102.82$) and the higher angular velocity for directional change is $\omega_h = 60$ rpm ($\bar{\omega}_h = 616.92$). The head size considered in this section is $b = 1.2$ cm and, from Fig. 5.3, the critical normalized angular velocity for buckling is $\omega_b \approx 52$ rpm ($\bar{\omega}_b \approx 534.66$). The outstanding problem is to compute the *running time*, t_c, at high angular velocity, ω_h, given the desired change in swimming direction.

In Fig. 5.4(a), we explain the turning process: the flagellated system is moving along an initial direction, $\mathbf{d}_0$, at time $t = 0$ and it has to change its swimming direction to $\mathbf{t}_1$. Without any loss of generality, we define a world frame $x - y - z$ based on the body-fixed

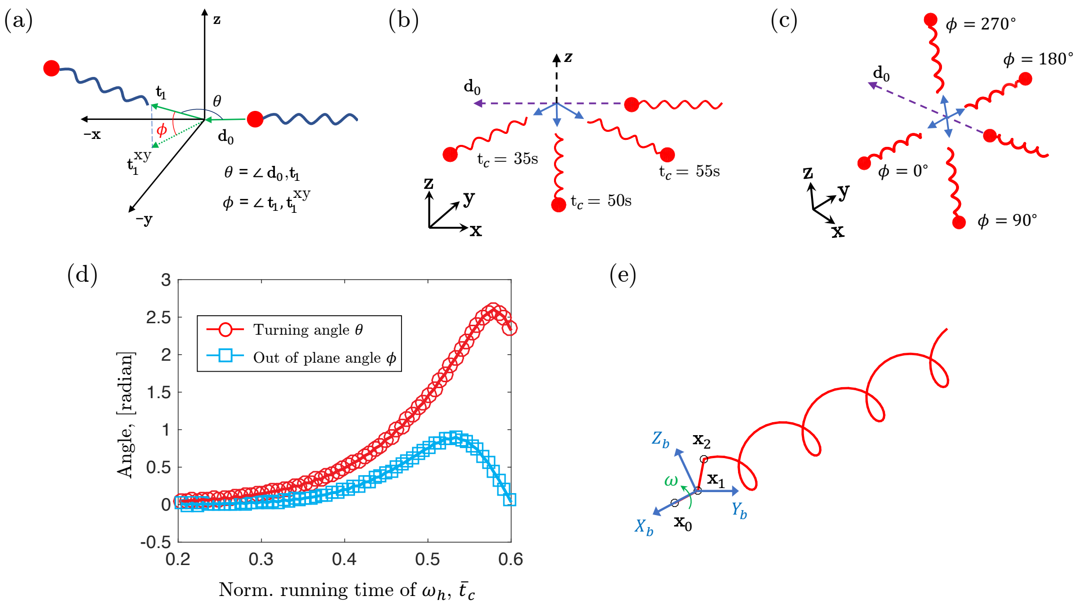

Figure 5.4: (a) Definition of turning angle, θ, and out of plane angle, ϕ, in 3D trajectory. (b) Illustration of different turning angle, θ, on $x - y$ plane ($\phi = 0$). (c) Illustration of different out of plane angle, ϕ, with a fixed turning angle, $\theta = 90°$. (d) Turning angle, θ, and out of plane angle, ϕ, as functions of running time, t_c, of higher angular velocity, ω_h. (e) Schematic of body-fixed frame of rotating helix.

frame $X_b - Y_b - Z_b$ at $t = 0$, such that the x, y, and z-axes are along $-X_b$, $-Y_b$, and Z_b-axes. This world frame remains fixed with time and the body-fixed frame moves and rotates with the flagellum. We can define the turn from $\mathbf{d}_0$ to $\mathbf{t}_1$ using two parameters: turning angle, θ, and out of plane angle, ϕ. Turning angle, θ, is the angle between the initial direction, $\mathbf{d}_0$, and the target direction, $\mathbf{t}_1$. Out of plane angle, ϕ, is the angle between the target, $\mathbf{t}_1$, and its projection, $\mathbf{t}_1^{xy}$, on the $x - y$ plane. Fig. 5.4(b) shows the initial and final directions, corresponding to different values of θ, at a fixed out of plane angle $\phi = 0°$. Next, to illustrate the out of plane angle, ϕ, Fig. 5.4(c) shows different out of plane angles at a fixed turning angle, $\theta = 90°$.

We first investigate how t_c influences the turning process, quantified by θ and ϕ. In Fig. 5.4(d), we plot the turning angle, θ, and out of plane angle, ϕ, between $\mathbf{d}_0$ and $\mathbf{t}_1$, as functions of t_c. Each value of t_c corresponds to a pair of θ and ϕ angles. We observe that the turning angle, θ, is nonlinearly related to the running time, t_c. Within a certain range ($0 \lesssim \bar{t}_c \lesssim 0.55$), the longer the buckled phase at ω_h, the greater the turning angle, θ.

Depending on the duration of the higher angular velocity, t_c, the system can make a turn from $0°$ to a maximum of $154°$. For a turn requiring an even greater turning angle, we can divide it into two turns so that each turn necessitates $\theta < 154°$.

For a given initial direction, $\mathbf{d}_0$, and final direction, $\mathbf{t}_1$, we can compute a turning angle, θ^*, and an out of plane angle, ϕ^{**}. The turning angle, θ^*, corresponds to a running time, t_c^* from Fig. 5.4(d). This combination of θ^* and t_c^* then corresponds to a specific value of out of plane angle, ϕ^*. However, the values of ϕ^* and ϕ^{**} are not necessarily equal and this may imply that the problem is overdetermined. Referring to Fig. 5.4(e), we can resolve this issue from the simple observation that the desired out of plane angle, ϕ^{**}, can be varied by upto 2π with a single rotation of the flagellum and the distance covered during a single rotation at the lower angular velocity, ω_l, is only 0.37 cm. This is negligible compared with the length of the flagellum $L = 13$ cm. A methodological explanation of the turning process, as implemented in our simulation, is provided next.

When the uniflagellar system, with the flagellum rotating at a low angular velocity of ω_l, needs to turn, it first computes the turning angle, θ^*, and the running time, t_c^*. This (θ^*, t_c^*) pair corresponds to an admissible value of the out of plane angle, ϕ^*, based on Fig. 5.4(d). The flagellated system will keep rotating at ω_l, i.e., *hovering*, until the required out of plane angle is equal to the admissible value of ϕ^*. The flagellum needs to make less than one turn during hovering and moves less than 0.37 cm. Following this step, the angular velocity of the flagellum will be increased to ω_h for t_c seconds and the swimming direction will change due to buckling. Subsequently, the angular velocity is switched back to ω_l to return to straight line motion. The sequence of steps discussed above has to be repeated for each turn in the trajectory. With this path planning strategy, the uniflagellar system can follow an arbitrary 3D trajectory with only a single control parameter – angular velocity ω – by utilizing the buckling instability of soft filament.

An example implementation is presented in Fig. 5.5 where the system covers a square trajectory on $x - y$ plane ($z = 0$; $x - y - z$ is the space-fixed frame) with each side of length $\Delta L = 0.25$m, approximately equal to only two body lengths. Initially ($t = 0$), the flagellated system is located at $z = 0$ along the x-axis. Fig. 5.5(a) presents snapshots of

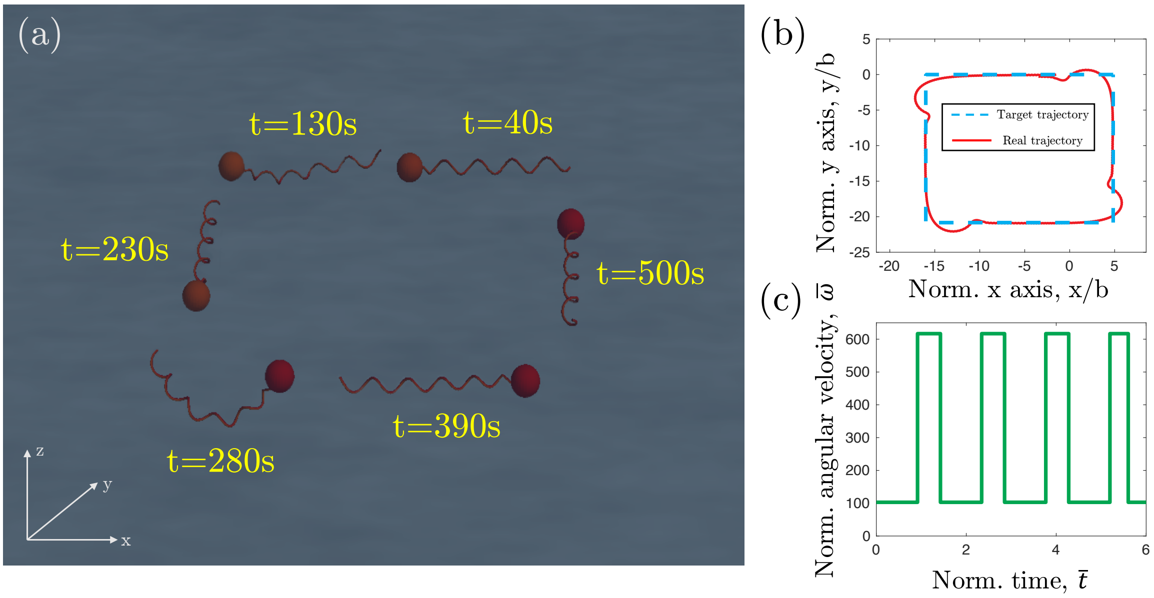

Figure 5.5: (a) A planar square trajectory obtained by buckling instability. (b) The comparison between the prescribed trajectory (dashed line) and real path (solid line). (c) The angular velocity ω as a function of time for the achieving of the desired trajectory.

the deformed structure at five points along the path. In Fig. 5.5(b), the target trajectory (dashed line) and the achieved trajectory (solid line) are shown on the $x - y$ plane. As desired, the trajectory remains almost entirely in the $x - y$ plane, with relatively small displacement along the z-axis, $\Delta z/\Delta L < 5\%$, during the buckled phase. The corresponding control signal – the angular velocity as a function of time – is presented in Fig. 5.5(c).

5.4 Summary and Outlook

We developed a computational framework to simulate the geometrically nonlinear deformation of soft filament and bio-locomotion of uniflagellar soft robot rotating in low Reynolds fluid environment and solved the inverse problem of following a desired trajectory simply using one control parameter – angular velocity ω. The computational framework fully accounts for three components: elasticity of the flagellum, long-range hydrodynamic forces on the flagellum, and the flow due to the head. We quantified the effect of the size of the head on the instability of the flagellum and the motion of the entire system. Our finding indicates a strong role of the head size on flagellar propulsion. We then studied the application of this instability to control the swimming direction of uniflagellar bacteria and robots. Supported by the robustness and efficiency of the numerical tools, we performed systematic parameter sweeps to quantify how the turning angles change with the time series of the angular velocity. The results are used to solve the problem of making a prescribed turn by varying the angular velocity with time. A sequence of such turns can then be employed to follow any prescribed trajectory in three dimensions. The results were presented in non-dimensional form to emphasize the scale independence of the phenomenon; turning by buckling may be used in the microscopic scale of bacteria and can be equally applicable to centimeter-sized swimming robots.

Our findings can lead to design and control of bioinspired soft robots that applies the same mechanism for swimming. Such robots will require a single control input, leading to simplified control scheme. The structure of these robots will be comprised of motor embedded in the head and one flexible flagellum, leading to simplified structural design. The material of the flagellum is linear elastic and, as such, a wide variety of polymeric materials can be used. The trajectory design in the current study has some limitations, i.e., after each turn, we allow the flagellum to relax to its unbuckled helical state and only then we can consider another turn. The numerical tool, in future, can be used in conjunction with machine learning to develop model-based control policies that are more generic. Importantly, we used a long range hydrodynamic force model and our framework may be extended to study multi-flagellated systems. In these more complex systems, the numerical simulation can be used as the source of data for machine learning-based data-driven models. We hope that our numerical results can inspire future work on all these fronts to motivate fundamental understanding of the biophysics of microorganisms and support the design of advanced functional soft robots.

CHAPTER 6

Bundling of Bacterial Flagella in a Viscous Fluid

In this chapter, we numerically investigate the fluid-structure interaction between two helical filaments rotating under low Reynolds number condition, motivated by the propulsion of bacteria using helical flagella. Our numerical framework couples the elasticity of the thin filaments, nonlocal hydrodynamic loading, and the contact between multiple linear elastic rods. Each of these three ingredients is respectively modeled by the Discrete Elastic Rods method (for a geometrically nonlinear description of soft filaments), Regularized Stokeslet Segments method (for a nonlocal drag force in viscous fluid), and non-penetration condition between rod segments. Two helical rods rotating side by side attract each other and become closer because of their hydrodynamic interplay in viscous fluid. Depending on the initial distance between the two and their rotational frequency, the two filaments can come in physical contact. Exploiting the efficiency and robustness of the simulator, we perform a systematic parameter sweep to quantify the bundling behavior. The findings may shed light on the physics of the bio-locomotion of microorganisms and inspire the design of novel biomimetic soft robots.

We introduce the underlying motivation and relevant literatures in § 6.1. The numerical simulation procedure is detailed in § 6.2. Then, the buckling instability of a single helical filament and the bundling between two helical flagellar are studied in § 6.3. The summary and potential directions for future research is concluded in § 6.4. The content of this chapter has been submitted, referring to Ref. [94].

6.1 Motivation

Bacteria often rely on the deformation of filamentary helical structures, called flagella, for locomotion [95, 9]. The propulsion arises from a complex fluid-structure interaction between the structural flexibility of the flagellum and the viscous forces generated by the flow. This fluid-structure interaction may lead to geometrically nonlinear deformations [96], which in turn can be exploited for functionality, e.g., turning [11], tumbling [10], and polymorphic transformations [97]. One of the particular biophysical importance is a phenomenon called bundling [70] that may appear during the swimming of microbes consisting of multiple flagella, e.g., *Escherichia coli* and *Salmonella typhimurium* [69]. Each flagellum consists of a rotary motor embedded in the cell wall, a short flexible hook that acts as a universal joint, and a helical filament. The trajectory of an individual swimming cell consists of runs interrupted by tumbles. Since the radius of the flagellar filament is well below optical wavelengths and the motor rotation is relatively rapid, it is difficult to study the mechanics of the bundling process through systematic experiments [69]. Predictive simulation of bundling is equally challenging due to the need to incorporate the long-range hydrodynamic interaction among multiple flagella, geometrically nonlinear deformation in the elastic rods – our model for flagella, and possible contact when two flagella come in close proximity. To mitigate the experimental challenges, scaled-up analog model experiments provide a promising path [69]. This chapter focuses on overcoming the computational hurdles to achieve fast and robust simulation of this system.

In comparison with simulation of uni-flagellar systems, multiple interacting flagella and their bundling clearly present a more difficult set of challenges. Previous experimental investigations built macroscopic model systems consisting of flexible rotating helices in a viscous fluid to mimic the dimensionless parameters of the natural bio-locomotion system, e.g., the ratio between elastic force and viscous drag, normalized helical pitch and radius, and the Reynolds number [69]. In the soft robotics community, researchers considered biomimetic soft robots with multi-flagellar structure for its propulsive efficiency and directional control [98]. Despite the critical role of bundling in the propulsion of several economically important bacteria – as evidenced by the aforementioned experimental works, a predictive numerical model for systematical investigation of flagellar bundling is a challenging work [12], simply because of the difficulty in describing the geometrically nonlinear dynamics of multiple rods coupled with the hydrodynamic interaction and the non-penetration contact between two approaching rod segments.

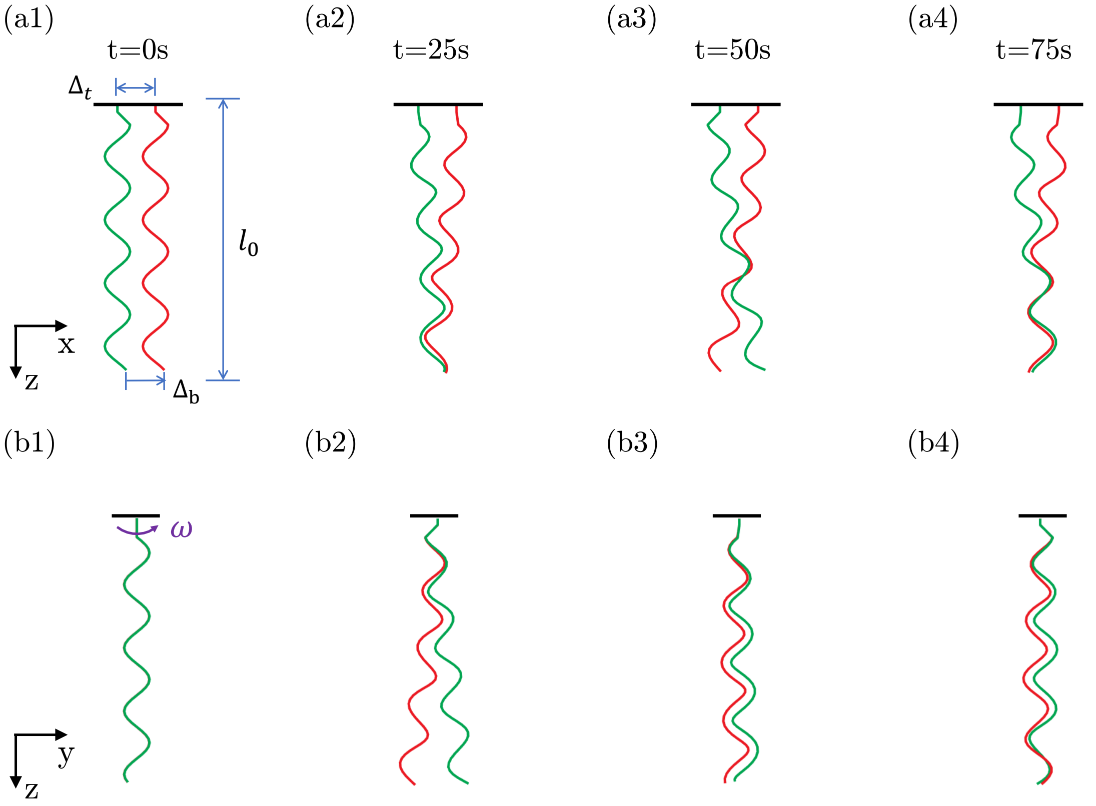

Figure 6.1: Two identical flagella rotate side by side at an angular velocity of $\omega = 15$rpm ($\bar{\omega} = 320$) with initial distance $\Delta_t = 3$cm. Front view (Upper) and side view (Lower) of helical rods at $t \in \{0, 25, 50, 75\}$s ($\bar{t} \in \{0, 0.125, 0.250, 0.375\}$).

Here, we numerically study the dynamics of two helical elastic rods rotating side-by-side at a constant angular velocity in low Reynolds environment. We develop a numerical framework that combines DER for elasticity of the structure [27, 28], Regularized Stokeslet Segments (RSS) method for long-range hydrodynamic force model [16], and a penalty force-based contact model [99]. While prior works coupled LSBT with DER, we choose to replace LSBT with RSS – nodel method published in 2018 – as the hydrodynamic model; the reason is twofold: (i) numerical issues appear when simulating the interaction among multiple rods using LSBT, because of the discontinuity between the local and nonlocal hydrodynamic terms in the LSBT formulation [15]. RSS, on the other hand, formulates a continuous flow field generated by a line segment with a regularization parameter and no numerical issues appear when two rod segments become closer and contact one another. (ii) The spatial discretization in LSBT-DER framework [3] is dictated by the ratio between the arclength of the flagellum, L, and the cross-sectional radius, r_0. The distance between two adjacent nodes – the discretization length – on the rod is required to be approximately equal to $1.65 r_0$. RSS, however, allows us to choose a coarser discretization without any specific requirement on discretization length. This results in more than an order of magnitude speed-up in the computation time for the model system studied in this chapter. Inclusion of physically-based contact model in the numerical framework is a novel feature of this study. To achieve non-penetration condition between two rod segments (a rod is divided into a number of segments in DER), we first perform a continuous collision detection during each time step of the simulation and iteratively include a penalty force in the equations of motion to guarantee no intersection between every pair of rod segments [99]. Similar contact formulations have been successfully applied in the computer graphics literature for geometric constraint maintenance [100], hair dynamics [101], and deformable body collision response [102]. The reliability of this simulation tool for making quantitative predictions is examined by a comparison between the previous experimentally validated LSBT-based method and the current RSS-based method. We then employ this computational method to quantify the deformation in two rotating flagella leading to bundling – a system similar to the one explored experimentally by [69]. Fig. 6.1 presents snapshots from our numerical simulation of a model setup for flagellar bundling. Through systematic parameter-space exploration, we analyze the onset of *bundling* between two soft filaments as a function of the angular velocity and the initial distance between the two flagella. We next measure the propulsive efficiency in a flagellum due to a nearby rotating flagellum. This is followed up by a sweep of geometric parameter space in biologically relevant regimes to quantify the dependence of bundling on the flagellar geometry. These observations can lead to better understanding of the presence of bundling and the resulting benefits to propulsion in microorganisms.

6.2 Numerical Framework

The numerical framework combines three components: (i) Discrete Elastic Rods (DER) method for the description of geometrically nonlinear deformation of soft filaments [27, 28, 29]; (ii) Regularized Stokeslet Segments (RSS) method for nonlocal hydrodynamic force generated by slender structures in viscous fluid [16], and (iii) a contact model for the achievement of non-penetration condition between two rod segments [99].

6.2.1 Regularized Stokeslet Segments Method

We use RSS to model the viscous drag force experienced by a slender rod in motion within a viscous fluid. In this section, we present the relation between the velocity at each node and the hydrodynamic force applied on each node [16].

The primary Green's function (or fundamental singular solution) of Stokes flow is the Stokeslet, which describes the flow associated with a singular point force [91]. For a particular choice of regularization [103], the velocity $\mathbf{u}(\hat{\mathbf{x}})$ at evaluation point $\hat{\mathbf{x}}$ due to a regularized force $\mathbf{f}(\mathbf{x})$ applied at $\mathbf{x}$ is the regularized Stokeslet

$$8\pi\mu\mathbf{u}(\hat{\mathbf{x}}) = (\frac{1}{R} + \frac{\epsilon^2}{R^3})\mathbf{f}(\mathbf{x}) + \frac{(\mathbf{f}(\mathbf{x}) \cdot \mathbf{r})\,\mathbf{r}}{R^3}, \tag{6.1}$$

where μ is the fluid viscosity, $\mathbf{r} = \hat{\mathbf{x}} - \mathbf{x}$, $R^2 = |\mathbf{r}|^2 + \epsilon^2$, and ϵ is the regularized parameter.

Next, consider an edge of length Δl connecting the nodes $\mathbf{x}_0$ and $\mathbf{x}_1$: a point on this edge is located at $\mathbf{x}_\alpha = \mathbf{x}_0 - \alpha\mathbf{v}$ (with $\mathbf{v} = \mathbf{x}_0 - \mathbf{x}_1$ and $|\mathbf{v}| = \Delta l$). As shown in Fig. 6.2, we assume a linear force density $\mathbf{f}_\alpha = \mathbf{f}_a + \alpha(\mathbf{f}_b - \mathbf{f}_a)$ along the cylinder segment, such that the velocity at point $\hat{\mathbf{x}}$ due to this linear force density is,

$$8\pi\mu\mathbf{u}(\hat{\mathbf{x}}) = \Delta l \int_0^1 \left[(\frac{1}{R_\alpha} + \frac{\epsilon^2}{R_\alpha^3})\mathbf{f}_\alpha + \frac{(\mathbf{f}_\alpha \cdot \mathbf{r}_\alpha)\mathbf{r}_\alpha}{R_\alpha^3} \right] d\alpha, \tag{6.2}$$

where $\mathbf{r}_\alpha = \hat{\mathbf{x}} - \mathbf{x}_\alpha$ and $R_\alpha^2 = |\mathbf{r}_\alpha|^2 + \epsilon^2$. With the assumption that $\mathbf{f}_\alpha$ is a polynomial in α, the velocity in Eq. (6.2) can be written as [16]

$$(8\pi\mu/\Delta l)\,\mathbf{u}(\hat{\mathbf{x}}) = \mathbf{f}_a(T_{0,-1} + \epsilon^2 T_{0,-3}) + \mathbf{f}_b(T_{1,-1} + \epsilon^2 T_{1,-3}) + \sum_{n=0}^{3} \mathbf{f}_n T_{n,-3}, \tag{6.3}$$

where the coefficients $\mathbf{f}_n$ are

$$\mathbf{f}_0 = (\mathbf{f}_a \cdot \mathbf{r}_0)\mathbf{r}_0, \tag{6.4a}$$

$$\mathbf{f}_1 = (\mathbf{f}_a \cdot \mathbf{v})\mathbf{r}_0 + (\mathbf{f}_a \cdot \mathbf{r}_0)\mathbf{v} + (\mathbf{f}_b \cdot \mathbf{r}_0)\mathbf{r}_0, \tag{6.4b}$$

$$\mathbf{f}_2 = (\mathbf{f}_a \cdot \mathbf{v})\mathbf{v} + (\mathbf{f}_b \cdot \mathbf{r}_0)\mathbf{v} + (\mathbf{f}_b \cdot \mathbf{v})\mathbf{r}_0, \tag{6.4c}$$

$$\mathbf{f}_3 = (\mathbf{f}_b \cdot \mathbf{v})\mathbf{v}. \tag{6.4d}$$

Then, the sequence of $T_{k,l}$ terms in Stokeslet Segments can be computed by the direct integration of α [16],

$$T_{0,-1} = \frac{1}{\Delta l} \log\left[\Delta l R_\alpha + (\mathbf{r}_\alpha \cdot \mathbf{v})\right]\Big|_0^1 \tag{6.5a}$$

$$T_{0,-1} = -\frac{1}{R_\alpha\left[\Delta l R_\alpha + (\mathbf{r}_\alpha \cdot \mathbf{v})\right]}\Bigg|_0^1 \tag{6.5b}$$

$$T_{1,-1} = \frac{R_\alpha}{(\Delta l)^2}\Bigg|_0^1 - \frac{(\mathbf{r}_0 \cdot \mathbf{v})}{(\Delta l)^2} T_{0,-1} \tag{6.5c}$$

$$T_{1,-3} = -\frac{1}{R_\alpha (\Delta l)^2}\Bigg|_0^1 - \frac{(\mathbf{r}_0 \cdot \mathbf{v})}{(\Delta l)^2} T_{0,-3} \tag{6.5d}$$

$$T_{2,-3} = -\frac{\alpha}{R_\alpha (\Delta l)^2}\Bigg|_0^1 + \frac{1}{(\Delta l)^2} T_{0,-1} - \frac{(\mathbf{r}_0 \cdot \mathbf{v})}{(\Delta l)^2} T_{1,-3} \tag{6.5e}$$

$$T_{3,-3} = -\frac{\alpha^2}{R_\alpha (\Delta l)^2}\Bigg|_0^1 + \frac{2}{(\Delta l)^2} T_{1,-1} - \frac{(\mathbf{r}_0 \cdot \mathbf{v})}{(\Delta l)^2} T_{2,-3} \tag{6.5f}$$

For completeness, we first describe the case of a continuous rod with arclength L (instead of a discrete rod composed of straight edges): consider a velocity at point $\hat{\mathbf{x}}$ due to

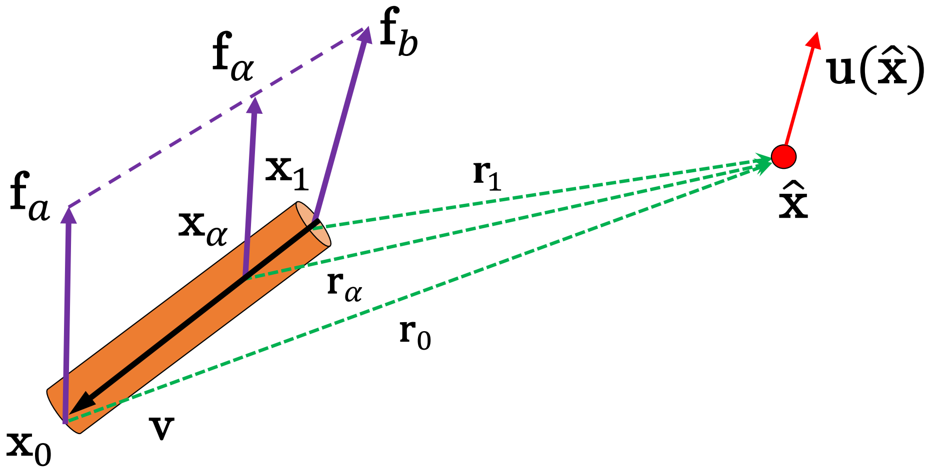

Figure 6.2: Notations associated with the flow $\mathbf{u}(\hat{\mathbf{x}})$ at point $\hat{\mathbf{x}}$ generated by a line segment from $\mathbf{x}_0$ to $\mathbf{x}_1$. Note $\mathbf{r}_\alpha = \hat{\mathbf{x}} - \mathbf{x}_\alpha$ and $\mathbf{v} = \mathbf{x}_0 - \mathbf{x}_1$.

the force field along a curve with arclength parameter, s:

$$8\pi\mu\mathbf{u}(\hat{\mathbf{x}}) = \int_0^L \left[(\frac{1}{R} + \frac{\epsilon^2}{R^3})\mathbf{f} + \frac{(\mathbf{f}\cdot\mathbf{r})\mathbf{r}}{R^3} \right] \mathrm{d}s. \tag{6.6}$$

Moving on to the case of a discrete rod with N nodes and $N-1$ segments, we denote the length of i-th segment as $|\mathbf{e}^i| \equiv |\mathbf{v}_i| = |\mathbf{x}_i - \mathbf{x}_{i+1}|$, and its force density (unit: force/length) as $\mathbf{f}_i$. Then the discretized version of Eq. (6.6) is

$$8\pi\mu\mathbf{u}(\hat{\mathbf{x}}) = \sum_{i=0}^{N-2} \left(\mathbb{A}_1^i \mathbf{f}_i + \mathbb{A}_2^i \mathbf{f}_{i+1} \right), \tag{6.7}$$

where $\mathbb{A}_1^i$ and $\mathbb{A}_2^i$ are 3×3 matrices:

$$\mathbb{A}_2^i = |\mathbf{v}_i| \left[(T_{1,-1}^{i,i+1} + \epsilon^2 T_{1,-3}^{i,i+1}) + T_{1,-3}^{i,i+1}(\mathbf{r}_i\mathbf{r}_i^T) + T_{2,-3}^{i,i+1}(\mathbf{r}_i\mathbf{v}_i^T + \mathbf{v}_i\mathbf{r}_i^T) + T_{3,-3}^{i,i+1}(\mathbf{v}_i\mathbf{v}_i^T) \right] \tag{6.8a}$$

$$\mathbb{A}_1^i = |\mathbf{v}_i| \left[(T_{0,-1}^{i,i+1} + \epsilon^2 T_{0,-3}^{i,i+1}) + T_{0,-3}^{i,i+1}(\mathbf{r}_i\mathbf{r}_i^T) + T_{1,-3}^{i,i+1}(\mathbf{r}_i\mathbf{v}_i^T + \mathbf{v}_i\mathbf{r}_i^T) + T_{2,-3}^{i,i+1}(\mathbf{v}_i\mathbf{v}_i^T) \right] - \mathbb{A}_2^i \tag{6.8b}$$

We use this formulation to build the following linear system that describes the relation between the velocity along the discrete rod and the force density applied on it:

$$\mathbf{U} = \mathbb{A}\mathbf{F}, \tag{6.9}$$

where $\mathbf{U} = [\dot{\mathbf{x}}_0, \dot{\mathbf{x}}_1, ..., \dot{\mathbf{x}}_{N-1}]^T$ is the velocity vector of the nodes (with no-slip boundary condition, the velocity of one point on the rod is equal to the velocity of viscous fluid at the same point) and $\mathbf{F} = [\mathbf{f}_0, \mathbf{f}_1, ..., \mathbf{f}_{N-1}]^T$ is the vector containing the force density at each node. The hydrodynamic force associated with i-th node is the product of the force density $\mathbf{f}_i$ and its Voronoi length Δl_i such that

$$\mathbf{F}_i^h = \mathbf{f}_i \Delta l_i. \tag{6.10}$$

6.2.2 Contact Between Two Filaments

In this subsection, we describe the contact model to enforce non-penetration condition between two approaching edges; this model has been described in sufficient detail in [99]. We first collect all the collision pairs (two edges that intersect) [104]. In our simulation code, a simple brute force method was employed to detect collisions. However, if the number of nodes is too large, the collision detection method can be made efficient by bounding volume hierarchy (BVH) through axis-aligned bounding boxes (AABBs) [105]. Referring to Fig. 6.3, the spatial coordinates of the i-th rod segment, $S_i = (\mathbf{x}_i, \mathbf{x}_{i+1})$, can be extracted from the generalized DOF vector $\mathbf{q}$, such that we can calculate the minimum Euclidean distance between two rod segments S_i and S_j,

$$\delta_{i,j}^{\text{min}} = \text{md}(\mathbf{x}_i, \mathbf{x}_{i+1}, \mathbf{x}_j, \mathbf{x}_{j+1}). \tag{6.11}$$

Then the collision detection procedure collects a set of collision pairs (S_i, S_j), with $\delta_{i,j}^{\text{min}} < 2r_0$, where r_0 is the rod radius. The penetration depth $\epsilon_{i,j}$ (should be always positive) of a collision pair (S_i, S_j) is defined as

$$\epsilon_{i,j} = 2r_0 - \delta_{i,j}^{\text{min}}. \tag{6.12}$$

We are looking for the minimum displacements $\{\Delta\mathbf{x}_i, \Delta\mathbf{x}_{i+1}, \Delta\mathbf{x}_j, \Delta\mathbf{x}_{j+1}\}$ such that the new coordinates define an interference free configuration. Since all the nodes have the same mass in our simulation, the required collision displacement of [99] simplifies to

$$\Delta\mathbf{x}_i = -\frac{1}{2}\mathbf{n}_{ij} w_i \tag{6.13a}$$

$$\Delta\mathbf{x}_{i+1} = -\frac{1}{2}\mathbf{n}_{ij}(1 - w_i) \tag{6.13b}$$

$$\Delta\mathbf{x}_j = \frac{1}{2}\mathbf{n}_{ij} w_j \tag{6.13c}$$

$$\Delta\mathbf{x}_{j+1} = \frac{1}{2}\mathbf{n}_{ij}(1 - w_j), \tag{6.13d}$$

where $\mathbf{n}_{ij}$ is the minimum distance vector between S_i and S_j (with $|\mathbf{n}_{ij}| = \delta_{i,j}^{\text{min}}$), and w_i (as well as w_j) is the barycentric coordinate of the contact point on the line segment. For a prescribed collision-based displacement at the i-th node, the contact force is

$$\mathbf{F}_i^{\text{c}} = \frac{1}{h^2}\Delta\mathbf{x}_i m_i, \tag{6.14}$$

where h is the time step size of the time-marching scheme (see next section) and m_i is the lumped mass of the i-th node. Similar results can be obtained for $(i+1)$-th, j-th, and $(j+1)$-th nodes.

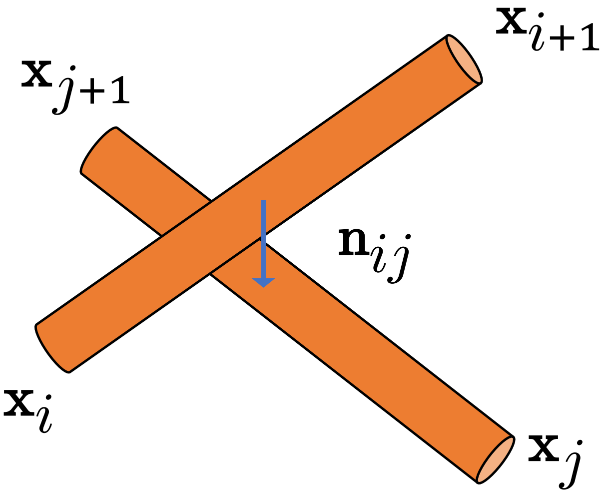

Figure 6.3: Notations of contact between two line segments S_i and S_j.

6.2.3 Numerical Simulation Procedure

Now we turn to the overall numerical framework of flagellar bundling simulation that involves updating the configuration of two rods with time. At each time step t_k, we know the DOF vectors and their time derivative (velocity vectors). To march forward in time, we need to compute the hydrodynamic force experienced by elastic rods and then solve the equations of motion, accounting for the contact between two filaments, to get the DOFs and velocities of next time step, $t_{k+1} = t_k + h$ (h is the time step size).

Besides the flow generated by its own hydrodynamic force, the drag force applied on one rod also contributes to a flow field affecting the other one, and vice versa. To account for the interplay between the two, the linear system $\mathbf{U} = \mathbb{A}\mathbf{F}$ in Eq. (6.9) should be expanded from size of $3N \times 3N$ to $6N \times 6N$,

$$\begin{bmatrix} \mathbf{U}^{(1)} \\ \mathbf{U}^{(2)} \end{bmatrix} = \begin{bmatrix} \mathbb{A}^{(11)} & \mathbb{A}^{(12)} \\ \mathbb{A}^{(21)} & \mathbb{A}^{(22)} \end{bmatrix} \begin{bmatrix} \mathbf{F}^{(1)} \\ \mathbf{F}^{(2)} \end{bmatrix}, \tag{6.15}$$

where matrices $\mathbb{A}^{(12)}$ and $\mathbb{A}^{(21)}$ show the interaction between two rods in viscous fluid, $\mathbf{F}^{(1)}$, and $\mathbf{F}^{(2)}$ are the $3N$-sized hydrodynamic force density vectors for the two rods, and $\mathbf{U}^{(1)}$, and $\mathbf{U}^{(2)}$ are the velocity vectors of same size. We use LDLT decomposition to obtain the viscous drag forces from the linear system in Eq. (6.15).

After computing the hydrodynamic forces acting on the rod, we independently solve for the DOF and velocity vectors of each rod from the equations of motion by a first order, implicit Euler integration,

$$\mathbf{E} \equiv \mathbf{M}\Delta\mathbf{q}(t_{k+1}) - h\mathbf{M}\dot{\mathbf{q}}(t_k) - h^2\left(\mathbf{F}^{\text{int}} + \mathbf{F}^c + \mathbf{F}^h\right) = \mathbf{0}, \tag{6.16a}$$

$$\mathbf{q}(t_{k+1}) = \mathbf{q}(t_k) + \Delta\mathbf{q}(t_{k+1}), \tag{6.16b}$$

$$\dot{\mathbf{q}}(t_{k+1}) = \frac{1}{h}\Delta\mathbf{q}(t_{k+1}), \tag{6.16c}$$

where the DOFs of the previous time step, $\mathbf{q}(t_k)$, and the velocities, $\dot{\mathbf{q}}(t_k)$ are known; the DOFs, $\mathbf{q}(t_{k+1})$, and velocities, $\dot{\mathbf{q}}(t_{k+1})$, of the next time step need to be solved for; $\mathbf{F}^{\text{int}}$ is the internal elastic force of size $(4N-1)$; $\mathbf{F}^h$ is the hydrodynamic force computed from Eq. (6.15) and Eq. (6.10); $\mathbf{F}^c$ is the contact force in Eq. (6.14); and $\mathbf{M}$ is the diagonal mass matrix comprised of lumped masses. The Jacobian associated with Eq. (6.16) is necessary for Newton's iteration and can be expressed as

$$\mathbb{J} = \mathbf{M} - h^2 \left[- \frac{\partial^2 \left(E_s + E_b + E_t\right)}{\partial \mathbf{q}^2} \right]. \tag{6.17}$$

Here, the gradient of the hydrodynamic force and contact forces cannot be analytically evaluated, i.e., external forces are treated explicitly.

At the beginning of each time step, we initialize the external contact force $\mathbf{F}^c$ as zeros, and compute the hydrodynamic force by Eq. (6.15) and Eq. (6.10), then solve the equations of motion in Eq. (6.16) to update the DOFs. This DOF is used to detect any collision. If the non-penetration condition is broken, external contact forces are updated on the basis of Eq. (6.13) and Eq. (6.14) and the equations of motion in Eq. (6.16) are solved again. This rewind and re-solve process continues until the non-penetration condition is achieved for every segment pair. The overall algorithm of flagellar bundling simulation can be found in algorithm 1.

6.2.4 Convergence Study

we present a convergence study with both time and space discretization for the coupling framework between DER and RSS. In Fig. 6.4(a), we show the relationship between the normalized height, $\bar{l}$, and the normalized angular velocity $\bar{\omega}$, at different values of number of vertices, $N \in \{43, 65, 81\}$, at a fixed time step size, $h = 1$ms. In the simulations presented in Fig. 6.4(a), we kept the regularization parameter fixed at $\epsilon = 1.02 r_0$. According to RSS theory, this parameter ϵ may vary between $1.01 r_0$ to $1.04 r_0$ as N is changed. However, the effect of 3% variation in ϵ has negligible effect on the simulation results.

We use a similar plot in Fig. 6.4(b) to show the convergence with time discretization for this numerical framework, at $N = 65$. The simulation results remain the same even when the time step size, h, is varied from $1e^{-3}$ to $1e^{-4}$.

Algorithm 1 Flagellar bundling simulation

```
**Input:** $k \leftarrow 0$, $t_k \leftarrow 0.0\text{s}$, $N$, $r_0$, $l \in \{1, 2\}$, $\mathbf{q}^{(l)}(t_k)$, $\dot{\mathbf{q}}^{(l)}(t_k)$, $\omega$, $h$, $T$, $tol$
while $t_k \leq T$ do
  $t_{k+1} = t_k + h$
  for $l = 1$ to $l = 2$ do
    $(\theta^0)^{(l)} \leftarrow (\theta^0)^{(l)} + h\omega$
    $(\mathbf{F}^c)^{(l)} \leftarrow \mathbf{0}$
  end for
  Calculate $\mathbb{A}^{(11)}, \mathbb{A}^{(12)}, \mathbb{A}^{(21)},$ and $\mathbb{A}^{(22)}$ from Eq. (6.8)
  Calculate $(\mathbf{F}^h)^{(1)}$ and $(\mathbf{F}^h)^{(2)}$ from Eq. (6.15) and Eq. (6.10)
  solved $\leftarrow 0$
  while solved $== 0$ do
    for $l = 1$ to $l = 2$ do
      $n \leftarrow 0$
      Guess $\mathbf{q}_n^{(l)}(t_{k+1}) = \mathbf{q}^{(l)}(t_k) + h\dot{\mathbf{q}}^{(l)}(t_k)$
      $error \leftarrow 10 \times tol$
      while $error > tol$ do
        Compute $\mathbf{E}_n^{(l)}$ in Eq. (6.16) and $\mathbb{J}_n^{(l)}$ in Eq. (6.17)
        $\mathbf{q}_{n+1}^{(l)}(t_{k+1}) = \mathbf{q}_n^{(l)}(t_{k+1}) - \mathbb{J}_n^{(l)} \backslash \mathbf{E}_n^{(l)}$
        $n \leftarrow n + 1$
        $tol = |\mathbf{E}_n^{(l)}|$
      end while
    end for
    solved $\leftarrow 1$
    for $i = 0$ to $i = N - 2$ do
      for $j = 0$ to $j = N - 2$ do
        Compute $\delta_{i,j}^{\text{min}}$ from Eq. (6.13)
        if $\delta_{i,j}^{\text{min}} < 2r_0$ then
          Compute $(\mathbf{F}_i^c)^{(1)}$, $(\mathbf{F}_{i+1}^c)^{(1)}$, $(\mathbf{F}_j^c)^{(2)}$, and $(\mathbf{F}_{j+1}^c)^{(2)}$ from Eq. (6.14)
          solved $\leftarrow 0$
        end if
      end for
    end for
  end while
  $k \leftarrow k + 1$
end while
```

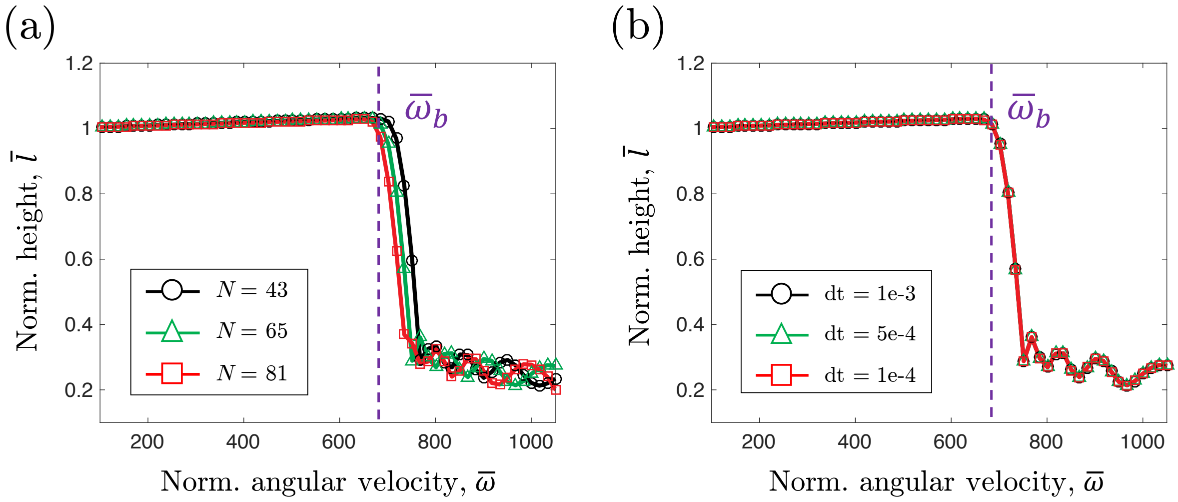

Figure 6.4: Convergence study for (a) space discretization and (b) time discretization.

6.3 Results

6.3.1 Comparison Between RSS and LSBT

Before the exploration on bundling of bacterial flagella, we first discuss the buckling instability of a single rotating helix in viscous medium, for comparison between the DER-LSBT model [3], that shows reasonable agreement with experiments, and the newly introduced DER-RSS framework. First we provide specifics on the geometric and physical parameters of the numerical study. We assume a right-handed helical rod, made out of a linear elastic material, with Young's modulus $E = 10\text{MPa}$ and Poisson's ratio $\nu = 0.5$ (incompressible). The rod density, $\rho = 1000\text{kg/m}^3$, is assumed to be equal to the fluid density so that no buoyant force is present. Radius of circular cross section is $r_0 = 1\text{mm}$, (and, therefore, second moment of inertia, $I = \pi r_0^4/4$, and cross section area, $A = \pi r_0^2$). The fluid viscosity is $\mu = 1.0$ Pa · s. As shown schematically in Fig. 6.5(a), in the stress free configuration, the first edge, $\mathbf{e}^0$, connecting $\mathbf{x}_0$ and $\mathbf{x}_1$, is parallel to the z-axis; the second edge connecting $\mathbf{x}_1$ and $\mathbf{x}_2$ is $\mathbf{e}^1 = R\hat{z} + R\hat{x}$ ($\hat{x}$ and $\hat{z}$ are unit vectors along the x and z axes, respectively); all other nodes, $[\mathbf{x}_2, \mathbf{x}_3, ..., \mathbf{x}_{N-1}]$, fall on a helical shape. The helix used in the current numerical study (axis length $l_0 = 0.2\text{m}$, helical pitch $\lambda = 5\text{cm}$, and helical radius $R = 1\text{cm}$), similar to the previous explorations [3, 89], is in the biological relevant regime [106]. The helical filament is clamped at one extremity, with first two nodes ($\mathbf{x}_0$ and $\mathbf{x}_1$) fixed. The first twisting angle, θ^0, is rotated anticlockwise (viewed from above with a prescribed angular velocity, ω). Apart from these fixed DOFs, all other nodes and edges are free and evolve based on the balance between elastic and fluid forces. In this representative setup, the number of nodes along the discrete rod is $N = 65$, corresponding to a Voronoi length of $\Delta l_i = 5$mm. The regularization parameter ϵ in RSS theory is related to the rod radius r_0, and can be determined based on the drag force experienced by a finite cylinder moving in viscous fluid perpendicularly to its axis. The regularization parameter, ϵ, varies slightly with the length of each edge. In our simulations, we choose $\epsilon = 1.02 r_0$ based on the value of $\Delta l_i / r_0$ [16]. The time step size in this simulation is $h = 1$ms.

In Figs. 6.5(b1-b2), we present representative deformed shapes of the rod rotating at two different angular velocities, $\bar{\omega} \in \{533, 1067\}$, after 100s. The end to end length l is used to quantify the deformation of helical rod. When the helical rod rotates at lower angular velocity, e.g., $\bar{\omega} = 533$, the whole structure retains its helical shape and stretches a little due to the hydrodynamic force from viscous fluid, seeing Fig. 6.5(b1); however, when the helical rod spins at a higher frequency, e.g., $\bar{\omega} = 1067$, the structure undergoes buckling instability and, in Fig. 6.5(b2), deforms into a highly nonlinear configuration. In Fig. 6.5(c1), we plot the normalized height of helical rod, $\bar{l} = l/l_0$, as a function of time for two different normalized angular velocity $\bar{\omega} \in \{533, 1067\}$. The final steady-state configurations can be achieved after $t = 50$s for both these two cases.

There exists a critical buckling angular velocity [3, 13] above which the final configuration is distorted, similar to the one shown in Fig. 6.5(b2). We perform a parameter sweep along angular velocity to find the critical buckling angular velocity, $\bar{\omega}_b$, of a single helical rod rotating in low Reynolds fluid. Fig. 6.5(c2) shows the normalized end to end length, $\bar{l}$, at time $t = 100$s, as a function of normalized angular velocity, $\bar{\omega}$. As expected, the soft filament remains in stable regime and stretch as a linear function of $\bar{\omega}$ at low enough angular velocity; When $\bar{\omega}$ is larger than a critical value, the rod will undergo buckling instability and deform into a curved shape . The maximum normalized angular velocity that retains

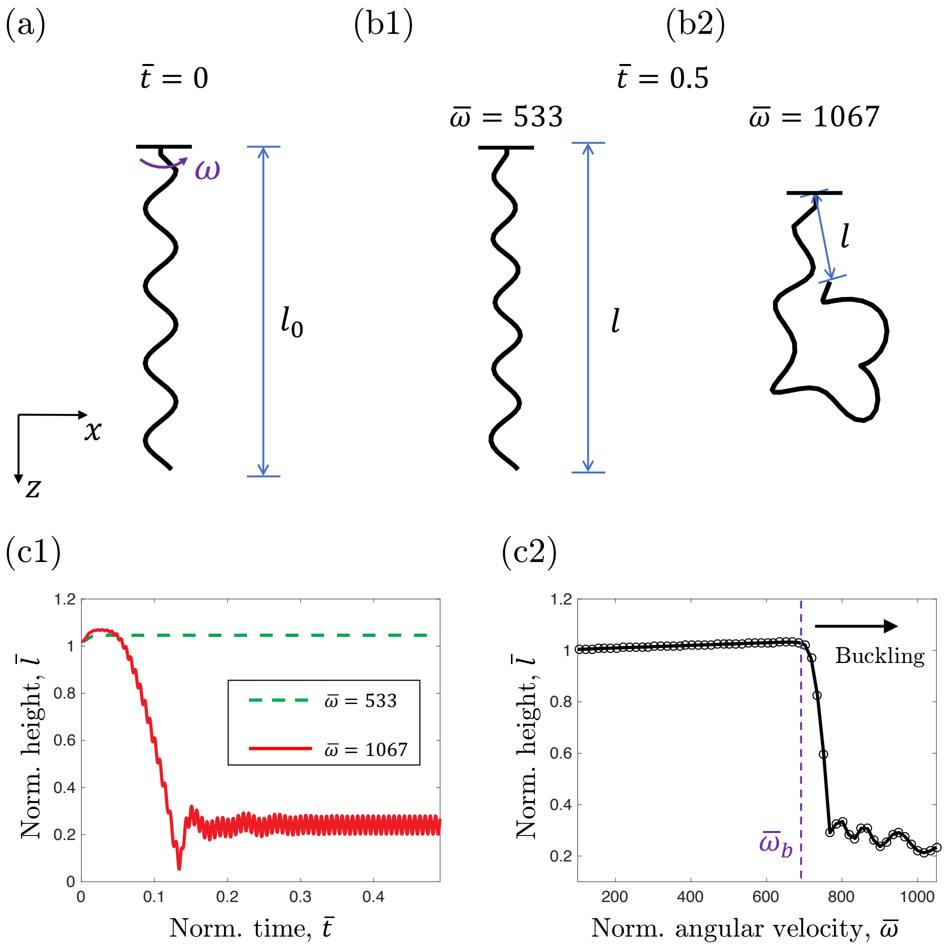

Figure 6.5: (a) The helical rod in stress free configuration. (b) Configuration of rotating flagellum at (b1) stable phase (with $\bar{\omega} = 533$) and (b2) buckling instability phase (with $\bar{\omega} = 1067$). (c1) Normalized height $\bar{l}$ as a function of normalized time for a single helical rod rotating at $\bar{\omega} \in \{533, 1067\}$. (c2) Normalized height $\bar{l}$ as a function of normalized angular velocity $\bar{\omega}$ for the definition of critical buckling angular velocity $\bar{\omega}_b$.

the helical shape of the structure is defined as the critical buckling angular velocity, $\bar{\omega}_b$. For the specific geometry chosen in this study, the normalized critical angular velocity is $\bar{\omega}_b \approx 675$.

We next briefly review the Lighthill Slender Body Theory (LSBT), and compare the numerical results performed by DER-LSBT method and DER-RSS framework. Note that for the specific helix discussed in this study (axis length $l_0 = 0.2$m, helical pitch $\lambda =$ 5cm, helical radius R =1cm, arclength $L = 0.32$m, and rod radius $r_0 = 1$mm), edge length should be $\Delta = 1.65$mm, resulting into $N = 195$ nodes. In Fig. 6.6(a), we plot the normalized height, $\bar{l}$, as a function of normalized rotating velocity $\bar{\omega}$, with two different fluid-structure interaction models: LSBT and RSS. The critical angular velocity obtained by LSBT is $\bar{\omega}_b^{\mathrm{LSBT}} \approx 660$, and the one achieved by RSS is $\bar{\omega}_b^{\mathrm{RSS}} \approx 675$, with relative error less than 5%.

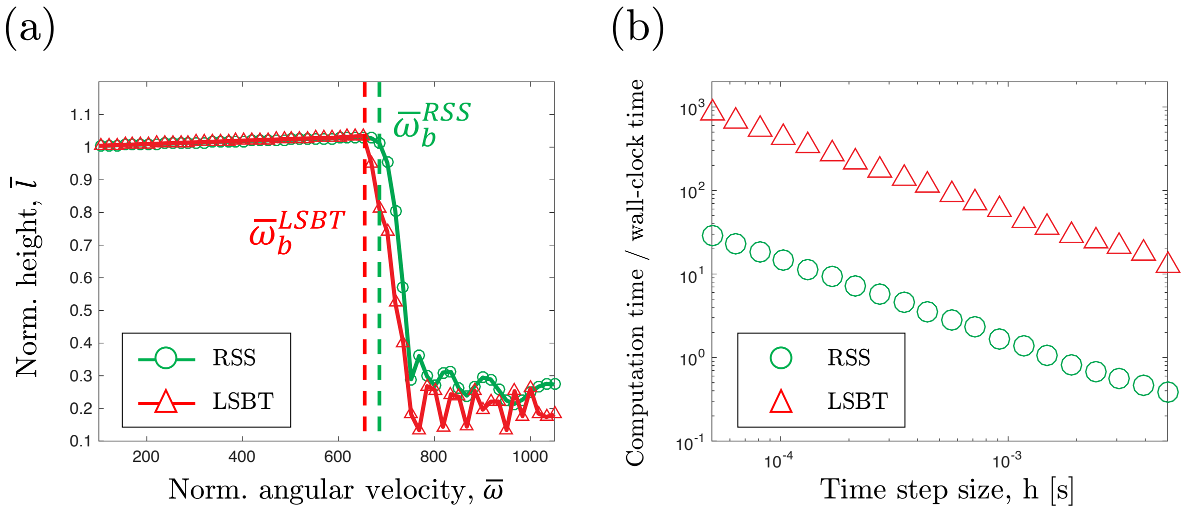

Figure 6.6: (a) Normalized height $\bar{l}$ as a function of normalized angular velocity $\bar{\omega}$ for LSBT and RSS. (b) The ratio between computational time and wall-clock time as a function of time step size h for LSBT and RSS.

Regarding computational efficiency, note that the size of each edge is fixed at Δ in LSBT. If the rod too slender (i.e., ratio between the total arclength and cross-sectional radius is large), we would require too many vertices and, consequently, a longer computational time. On the other hand, RSS allows more aggressive discretization (i.e., lower number of nodes). In Fig. 6.6(b), we show the computational time, normalized by the wall-clock time, as a function of time step size, h, for both RSS ($N = 65$) and LSBT ($N = 195$) method. The simulations ran on a single thread of AMD Ryzen 1950X CPU @ 3.4 GHz. Even though the node number of LSBT is only three times larger than RSS, the computational time of LSBT is almost 30 times slower than the time performed by RSS. This is rooted in the computational time of solving the dense linear system.

6.3.2 Bundling Between Two Rotating Flagella

We now turn to the main contribution of the current study and include the effect of the interaction between two rotating helical rods in viscous fluid. Previous coupling numerical framework between DER and LSBT can also capture the buckling instability of a single helical rod rotating in viscous fluid [3, 89], but meets numerical issue when applied to study the bundling behavior of multiple flagella, because LSBT divides the hydrodynamic force generated by soft filaments into two parts, local and nonlocal terms; as two rod segments attract each other and become closer, nonlocal hydynamic term must be replaced by local formulation, and the numerical simulator got into stuck at this discontinuous step. This issue, on the other hand, can be solved by RSS method, for its continuous evaluation of Stokeslet generated by cylinder segment.

Fig. 6.1 shows a sequence of snapshots of two helices (axis length $l_0 = 0.2$m, normalized helical pitch $\lambda/l_0 = 0.25$, and normalized helical radius $R/l_0 = 0.05$) rotating side by side with same frequency, $\bar{\omega} = 320$ (both anticlockwise when viewed from above), at a normalized initial distance $\Delta_t/R = 3$. The induced flows of helical rods cause large deflections, and then a bundle form appears. The helices wrap around each other in a right-handed sense; the flow field generated by each helix tilts the other helix, causing the helices to roll around each other and form a right-handed wrapping. We use the end to end distance between two rods along the x-axis, denoted as Δ_b (see Fig. 6.1(a1)), as a shape parameter to quantify the bundling behavior between two rotating filaments. This parameter, Δ_b, becomes negative when two rods wrap around each other.

We now turn to examine the effect of angular velocity on the end to end distance. Fig. 6.7(a1)-(a3) shows the trajectory of the end of the rod – the last node in DER simulation – on the $x-y$ plane with time at three different normalized angular velocities $\bar{\omega} \in \{43, 107, 427\}$, with the normalized top distance fixed at $\Delta_t/R = 4$. Similar data from macroscopic model experiments can be found in [69]. We observe that the two flagella come closer through a U-shaped trajectory of the last node. Eventually, the two ends settle to a steady circular path. Fig. 6.7(c1) plots the normalized end to end distance, Δ_b/R, as

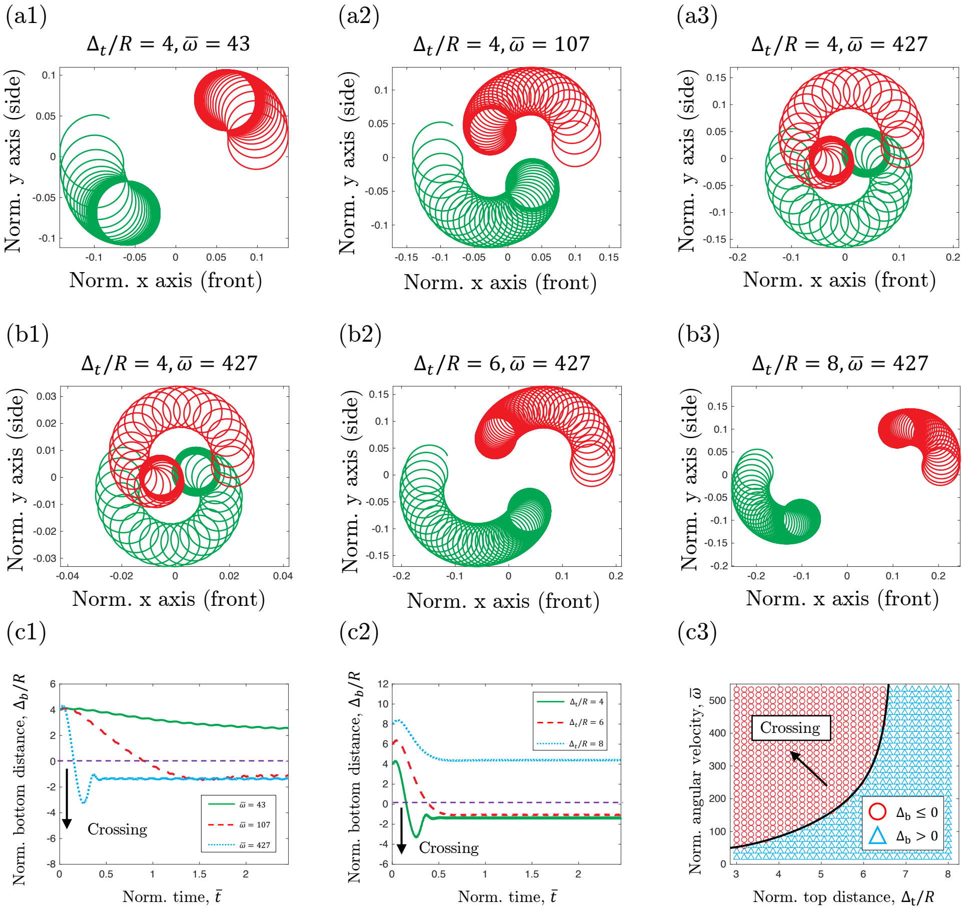

Figure 6.7: Projected trajectory of helical end point on normalized $x-y$ plane, with different parameter combinations: (a) normalized top distance $\Delta_t/R = 4$ fixed, varying angular velocity $\bar{\omega} \in \{43, 107, 427\}$; (b) normalized angular velocity $\bar{\omega} = 427$ fixed, varying initial top distance $\Delta_t/R \in \{4, 6, 8\}$. Normalized bottom distance Δ_b/R as a function of normalized time by varying (c1) angular velocity $\bar{\omega}$ and (c2) initial top distance Δ_t/R. (c3) Phase diagram of the critical crossing angular velocity in the $(\Delta_t/R, \bar{\omega})$ parameter space.

a function of time, in all these three cases. While the top distance, Δ_t, – the distance between the first nodes on two rods – remains fixed with time due to the boundary conditions imposed in the simulation, the end to end distance varies significantly due to the deformation from hydrodynamic forces. Also note that $\Delta_t = \Delta_b$ at time $t = 0$. For small angular velocity, two rods will become closer in their final stable shapes with $0 < \Delta_b/R < \Delta_t/R$, shown in Fig. 6.7(a1). However, when rotating at a higher angular velocity, two helical rods can go beyond each other, such that a *crossed* configuration with $\Delta_b/R < 0 < \Delta_t/R$ can be achieved, when looking on the $x-z$ plane. An example configuration is presented in Fig. 6.1(a3).

We now explore the role of the initial top distance, Δ_t, on the bundling behavior of two flagella. In Fig. 6.7(b1)-(b3), we plot the trajectory of the last nodes of the rods at three different values of top distance, $\Delta_t/R \in \{4, 6, 8\}$, while keeping the normalized angular velocity fixed at $\bar{\omega} = 427$. Fig. 6.7(c2) shows the end to end distance as a function of time in these three cases. When the top distance is small ($\Delta_t/R = 4$ and $\Delta_t/R = 6$), the crossed shape is achieved within $t \approx 100$s. However, in the long distance case ($\Delta_t/R = 8$), the end to end distance eventually reaches a value equal to approximately half of the top distance and always remains positive ($\Delta_b/R > 0$).

To combine all the information together, in Fig. 6.7(c3), we perform a two dimensional parameter sweep, by varying both angular velocity, $\bar{\omega} \in [0.0, 550.0]$, and initial distance, $\Delta_t/R \in [3.0, 8.0]$, and show the final shape. A circular symbol presents a crossed configuration ($\Delta_b \leq 0$), whereas a triangle stands for $\Delta_b > 0$. The critical normalized angular velocity beyond which this crossed configuration is achieved is defined as $\bar{\omega}_c$, and, in Fig. 6.7(c3), is indicated by a solid line. This threshold parameter, $\bar{\omega}_c$, first increases as the the initial distance Δ_t increases. When the initial distance exceeds $\Delta_t/R \approx 7$, the crossing behavior cannot be achieved even when the angular velocity goes beyond the critical buckling angular velocity, $\bar{\omega}_b$, discussed in the previous section.

Then, we turn the focus to the propulsive force of two helical flagella rotating side by side. The first two nodes are fixed in place and the reaction forces corresponding to this boundary condition (equal to the sum of elastic and external forces on the node in question) can be computed from the simulation. The propulsive force is defined here as the average of the reaction forces applied on the first two fixed nodes, $\{\mathbf{x}_0, \mathbf{x}_1\}$, projected along the z-axis,

$$F_p = \frac{1}{2}\left[(\mathbf{F}_0^{\text{cons}})^{(1)} + (\mathbf{F}_1^{\text{cons}})^{(1)} + (\mathbf{F}_0^{\text{cons}})^{(2)} + (\mathbf{F}_1^{\text{cons}})^{(2)}\right] \cdot \mathbf{n}_z, \tag{6.18}$$

where $\mathbf{n}_z = [0, 0, 1]^T$ is the unit vector along the z-axis, $\mathbf{F}_i^{\text{cons}}$ is the constrained force applied on the i-th node, and the superscript represents the rod number. Next, we formulate

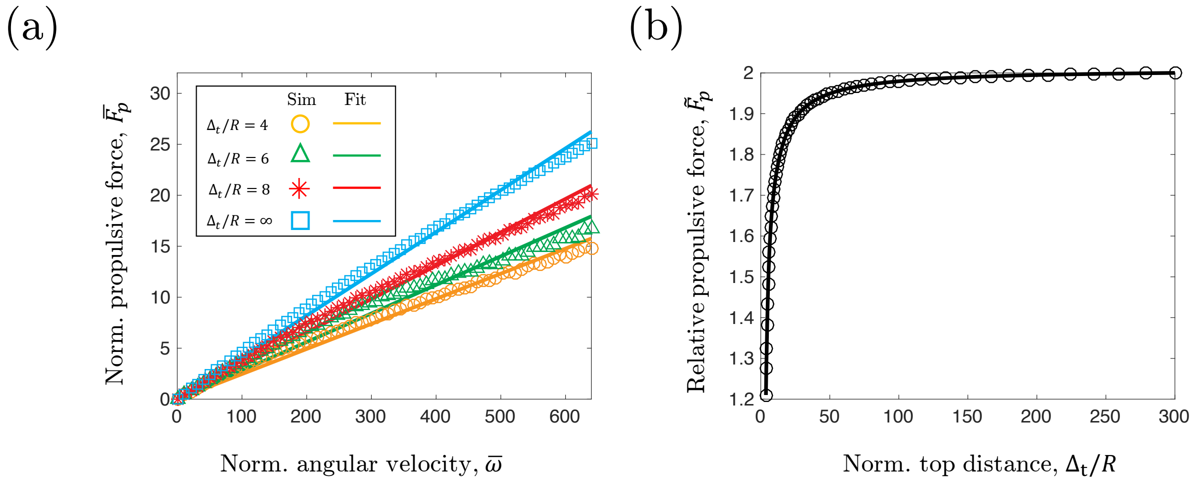

Figure 6.8: (a) Normalized propulsive force $\bar{F}_p$ as a function of normalized angular velocity $\bar{\omega}$, by varying normalized top distance, $\Delta_t/R \in \{4, 6, 8, \infty\}$, from simulation (symbols) and linear fit (solid lines). (b) Relative propulsion, $\tilde{F}_p$, as a function of normalized top distance, Δ_t/R, with a fixed normalized angular velocity $\bar{\omega} = 213$.

a non-dimensional propulsive force,

$$\bar{F}_p = F_p l_0^2/(EI), \tag{6.19}$$

by normalizing F_p with the characteristic bending force, EI/l_0^2 [89]. In Fig. 6.8(a), we plot the normalized propulsive force, $\bar{F}_p$, as a function of normalized angular velocity, $\bar{\omega}$, at different values of normalized top distance, $\Delta_t/R \in \{4, 6, 8, \infty\}$. The propulsive force approximately linearly goes up with the increase of the angular velocity in the pre-buckling phase. The propulsive force is maximum when two helices are rotating at infinite distance, i.e., there is no hydrodynamic interaction between them. As the top distance decreases, the propulsive force monotonically decreases. Compared with the case of $\Delta_t = \infty$, the propulsive force at $\Delta_t/R = 4, 6,$ and 8 decreased 40.0%, 31.7%, and 20.2%, respectively. Moreover, in Fig. 6.8(b), we show the normalized propulsive force, $\bar{F}_p$, as a function of normalized top distance, Δ_t/R, with a fixed normalized angular velocity, $\bar{\omega} = 213$. Here, we clearly see that the propulsive force increases by more than 60% from $\Delta_t/R = 3$ to $\Delta_t/R = 50$, and shows almost no variation beyond $\Delta_t/R > 100$. Regardless of the top distance, the propulsive force with hydrodynamic interaction is always lower than the force without this interaction.

This far, we kept the geometry of the flagella at the representative value. Now, we employ our numerical simulation to explore the effect of the geometric parameters on the critical crossing angular velocity, ω_c, in biologically relevant regime [106]. Specifically, we varied the helical pitch, λ/l_0, and helical radius, R/l_0, to understand the hydrodynamic performances of helices in different shapes. In Fig. 6.9(a), we vary the normalized helical pitch, $\lambda/l_0 \in [0.15, 0.45]$, at fixed values of radius ($R/l_0 = 0.05$) and top distance ($\Delta_t/R = 4$), and plot the normalized critical crossing angular velocity, $\bar{\omega}_c$, as a function of the normalized helical pitch. Note that the parameter, $\bar{\omega}_c$, strongly depends on the pitch of the flagella. On the other side, we vary helical radius in the range $R/l_0 \in [0.0375, 0.1125]$, at fixed values of $\lambda/l_0 = 0.25$ and $\Delta_t/R = 4$, and, in Fig. 6.9(b), explore the variation of $\bar{\omega}_c$ with the nondimensional helical radius, R/l_0. We again observe that the helical radius significantly changes the bundling behavior. As the radius increases, the angular velocity required for the crossed configuration decreases. Altogether, these results emphasize the prominent role of geometry of the helical filaments on their hydrodynamic interactions between each other with a focus on biologically relevant regime [107, 106]. Our investigation opens up questions on how microorganisms utilize bundling of their flagellar during their motion in low Reynolds environment.

6.4 Summary and Outlook

We have introduced a computational framework to study the geometrically nonlinear interaction between two neighboring elastic flagella rotating in a viscous fluid. For this purpose, our numerical approach combined DER, RSS, and a contact model. We first studied the mechanical response of a single helical rod undergoing rotation in low Reynolds environment, and compared the results against the experimentally validated fluid-structure interaction model, LSBT. The relative $\leq 5\%$ error between the critical buckling angular velocity computed from LSBT and the one obtained by RSS indicates the accuracy of the numerical method coupling DER and RSS. Empowered by this simulation tool, we next

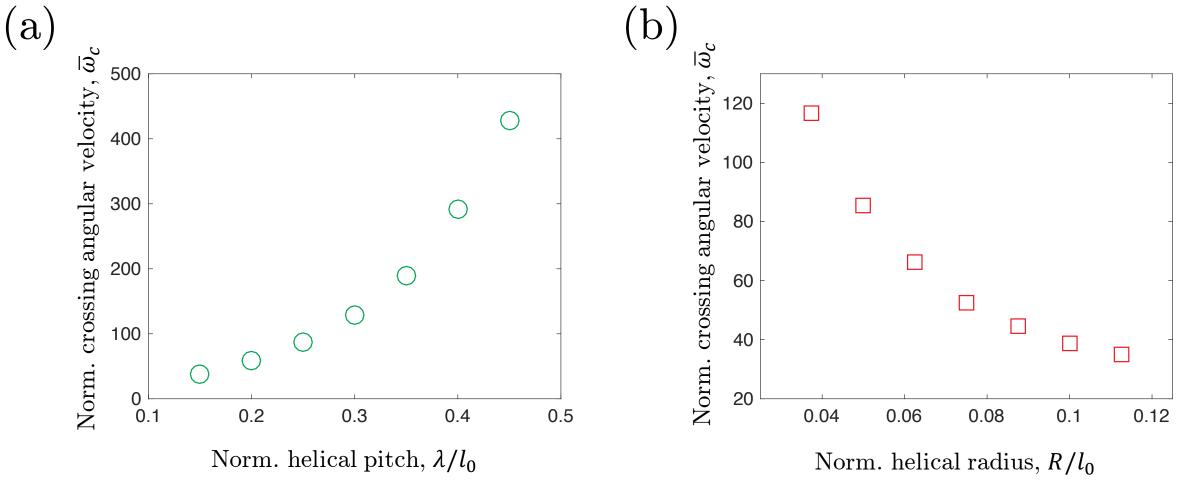

Figure 6.9: Normalized critical crossing angular $\bar{\omega}_c$ versus (a1) normalized helical pitch λ/l_0 (with $R/l_0 = 0.05$ and $\Delta_t/R = 4$ fixed) and (a2) normalized helical radius R/l_0 (with $\lambda/l_0 = 0.25$ and $\Delta_t/R = 4$ fixed).

investigated the dynamics between two rotating soft filaments side-by-side in a viscous fluid. Two rotating helical rods attract each other and become closer because of the coupling flow field generated by each other; and the crossing behavior is related to their initial distance and rotating frequency. The propulsive force, on the other hand, shows a decreasing tendency as two flagella are brought closer to one another. In order to realize the importance of the helical geometry in the propulsion of natural bacterial flagella, the simulation tool was then employed to sweep through parameter space along two geometric parameters (helix pitch and radius), for quantification of the bundling behavior and the critical rotating velocity for crossing. Our findings are scale invariant and can be applied to bacterial propulsion at micron-scale as long as the dimensionless groups (e.g., Reynolds number, normalized angular velocity, normalized helical pitch, and so on) are maintained. The results on the effect of angular velocity and geometry on the bundling behavior and propulsive force are, therefore, potentially relevant to flagellated bacteria.

The significant effect of flagellum geometry, flexibility, and the interaction in viscous fluid poses a nontrivial design space for both nature and engineering. This might have potential application in controlling the swimming speed and direction in multi-flagellated microorganisms. Our findings may also provide guidelines for the design of laboratory experiments on bacterial propulsion and biomimetic soft robots. Since we avoid the numerical discontinuity in previous long-range hydrodynamic force model, LSBT, our framework can be directly applied for the simulations of bacterial system with more than one flagellum. The sparse space discretization of RSS shows a better computational efficiency than LSBT, and this fast numerical framework can be treated as a data generator by sweeping the essential geometric and physical parameters, for a better understanding of biophysics in natural environment, and can also be potentially used for the optimized design and online control of multi-flagellated soft robots. We hope that our numerical investigations can motivate a fundamental understanding of the biophysics of microorganisms, as well as support modeling, design, and control of functional soft robots.

CHAPTER 7

Numerical Method for the Form-finding Problem in Convex Gridshell

Elastic gridshell is a class of net-like structure formed by an ensemble of elastically deforming rods coupled through joints, such that the structure can cover large areas with low self-weight and allow for a variety of aesthetic configurations. Gridshells, also known as X-shells or Cosserat Nets, are a planar grid of elastic rods in its undeformed configuration. The end points of the rods are constrained and positioned on a closed curve – the final boundary – to actuate the structure into a 3D shape. Here, we report a discrete differential geometry-based numerical framework to study the geometrically nonlinear deformation of gridshell structures, accounting for non-trivial bending-twisting coupling at the joints. The form-finding problem of obtaining the undeformed planar configuration given the target convex 3D topology is then investigated. For the forward (2D to 3D) physically-based simulation, we decompose the gridshell structure into multiple one dimensional elastic rods and simulate their deformation by the well-established Discrete Elastic Rods (DER) algorithm. A simple penalty energy between rods and linkages is used to simulate the coupling between two rods at the joints. For the inverse problem associated with form-finding (3D to 2D), we introduce a contact-based algorithm between the elastic gridshell and a rigid 3D surface, where the rigid surface describes the target shape of the gridshell upon actuation. This technique removes the need of several forward simulations associated with conventional optimization algorithms and provides a direct solution to the inverse problem. Several examples, e.g., hemispherical cap, paraboloid, and hemi-ellipsoid, are used to show the effectiveness of the inverse design process.

We introduce the motivation and review the relevant literatures in § 7.1. Next, we discuss the numerical method for the simulation of elastic gridshell in § 7.2. The result is in § 7.3. Finally, the summary is presented in § 7.4. The content of this chapter has appeared in Ref. [108].

7.1 Motivation

Traditional three dimensional shell structures can resist external loads through their inherent shapes; however, if regular holes are made in the shell, with the removed material concentrated into the remaining strips, a structurally flexible gridshell can be achieved. Several spectacular architectures, e.g., Helsinki Zoo's observatory tower and Centre Pompidou Metz, were manufactured with a network of one dimensional beams; such structures serve both aesthetical and functional purposes in the civil engineering community [109]. Besides the construction of buildings in civil engineering [110], abundant applications in mechanical systems, e.g., micro/nano structures [111], stretchable electronics [112], and bio-inspired patterns [113], employ gridshell as a major structural component in their design step to achieve specific functionalities. While the gridshells studied by Baek et al. [17, 18] had joints that were free to rotate and twist, recent work by Panetta et al. [114] constrained the bending and twisting at the joints. This leads to non-trivial twisting and bending coupling between two rods at the joints, which can improve the robustness of the structure and increase the design space of the architectural shapes [115]. Computationally efficient numerical simulation tools for this class of structures can allow simulation-guided design and eliminate the need for painstaking trial-and-error prototyping.

In the computational mechanics community, modeling and simulation of thin elastic objects, e.g., rods and shells, are of sufficient general interest because of the preponderance of geometrically nonlinear deformation. Finite Element Method has been the most commonly used method in structural analysis over the past few decades [116]. Recently, Discrete Differential Geometry (DDG)-based methods [31] are becoming popular in the computer graphics community to simulate the thin elastic structures, e.g., hair and clothes, due to the computational efficiency and the robustness in handling geometric nonlinearity, collision, and contact [117, 118]. Gridshell usually represents a curved surface comprised

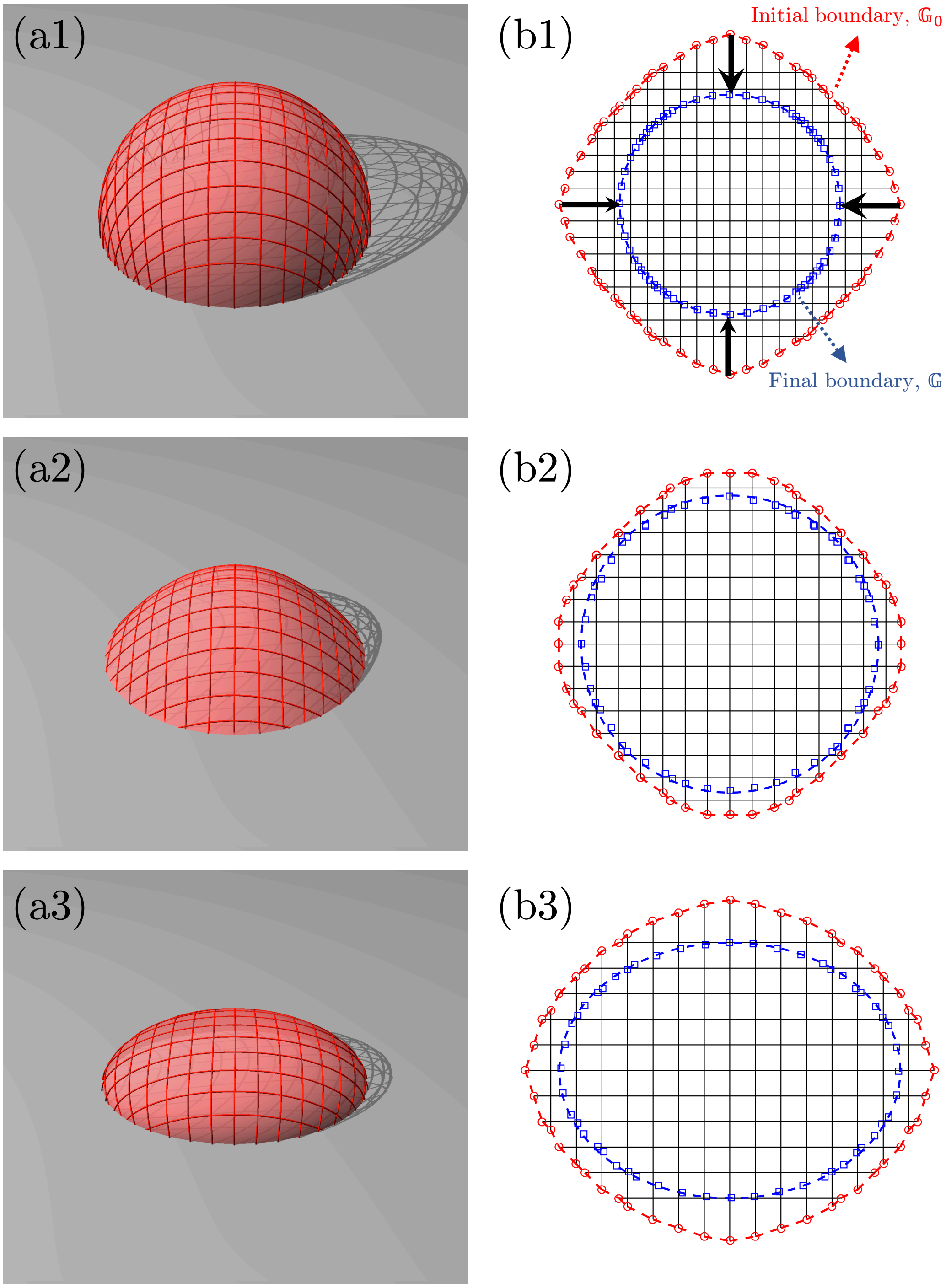

Figure 7.1: (a) 3D gridshells: (a1) hemispherical cap, (a2) paraboloid, and (a3) hemi-ellipsoid. (b) Their corresponding initial and final boundaries.

of multiple 1D elastic rods and differs from the traditional 1D rods or 2D shells. This leaves room for new numerical methods for accurate and efficient simulation of gridshells. Baek et. al first proposed a method based on Discrete Elastic Rods (DER) to investigate the buckling instability and form-finding of gridshells [17] and found excellent agreement between experiments and simulations. A stiff spring is used in that framework to simulate the joint between two rods and the spring force is treated using an explicit approach. The joint between two intersecting rods is free to twist as well as rotate such that the twisting and bending coupling between two rods are not taken into account. This numerical framework was later used to study the elastic rigidity of hemispherical gridshells [18]. Numerical methods to capture the bending and twisting coupling at the joints either use a penalty energy between the neighboring material frames of two rods system [119], or a geometric constraint-based energy functional [114]. Finite element-based numerical methods to simulate this class of structures have also been introduced [120].

An even more intriguing feature of elastic gridshell is its form-finding process. Fig. 7.1(a) shows three examples of convex 3D gridshells, whereas Fig. 7.1(b) describes the actuation process. In Fig. 7.1(b), the undeformed gridshell is planar and the extremities of the elastic rods fall on a closed curve, $\mathbb{G}_0$. In order to actuate the gridshell, the end points of the rods are constrained to fall on a second closed curve, $\mathbb{G}$. The form-finding problem, i.e., the inverse problem in this case, calls for computation of $\mathbb{G}_0$ given the target 3D shape and the final boundary, $\mathbb{G}$. This transformation between the 2D planar structures and the complex 3D topologies by using the geometry and structural instability is of interest [113], and might lead many applications in mechanical systems [121]. Prior works on mechanically guided assembly of 3D structures range from macroscopic origami-inspired structures [122] to microscopic buckling of elastic ribbons attached to a pre-stretched substrate [111]. While a number of studies investigated the forward dynamics, we focus on a computationally efficient method to solve the inverse design problem of finding the initial planar shape with a given 3D target configuration. Ref. [123] considered Chebyshev net theory to map a group of rods onto a given surface, e.g., human face, to design wire mesh. Prior works on the inverse problem include analytical solution to a pair of ordinary differential equations (ODEs) on the basis of Gauss equation [17], or numerical optimization coupled with physics-based simulations [113, 114, 124]. Recently, a genetic algorithm-based method [124] and an optimization-based simulation framework [114] have been introduced to study the form-finding problem in elastic gridshells; however, these methods require running the physics-based simulation numerous times in order to find the optimal solution, especially when a good initial guess is not available. As an example, the form-finding problem of a hemispherical gridshell in Fig. 7.1(a) may take approximately 10^2 generations with 5×10^2 individuals in a population in genetic algorithm, corresponding to 5×10^4 forward simulations. The proposed method reduces this problem to a single forward simulation.

Here, we develop a numerical method for the inverse form-finding problem of gridshells. Different from above analytic and optimization methods that typically require numerous “forward" simulations to predict the deformation of the gridshell under various boundary conditions imposed by $\mathbb{G}$ and $\mathbb{G}_0$, this method implements a mechanics-based forward simulation of a gridshell draping around the target rigid shape under gravity. This single forward simulation can offer an excellent solution to the inverse problem. The simulation relies on a DER-based numerical framework, where both the rods and the joints are represented by the discrete elastic rod model. Discrete equations of motions, based on the balance of elastic and external forces, are solved to update the structural configuration with time. The main contribution of this paper is a numerical method for form-finding of convex gridshells based on contact [125]. In Fig. 7.1, we show several 3D configurations of convex gridshell structures as well as their corresponding initial planar boundaries constructed by the contact-based method described in this paper. The boundary of the 2D undeformed shape, $\mathbb{G}_0$, can be almost exactly obtained by draping the elastic gridshell under gravity over the rigid 3D target surface. This calls for simulation of contact between the gridshell and the rigid surface and is handled via the modified mass method [48]. Discrete simulations are naturally suited to handle contact, which underlines the need for DDG-based methods in the study of form-finding of gridshells. The initial planar pattern of grid can be easily obtained by only running the physically-based simulation once, which can significantly reduce the computational time when solving the form-finding problem.

7.2 Numerical Method

7.2.1 Discrete Elastic Gridshells

In this section, we discuss the forward physically-based simulation of gridshells. Gridshell is a type of structure that comprises multiple one dimensional rods connected through joints. These joints may twist and rotate [114].

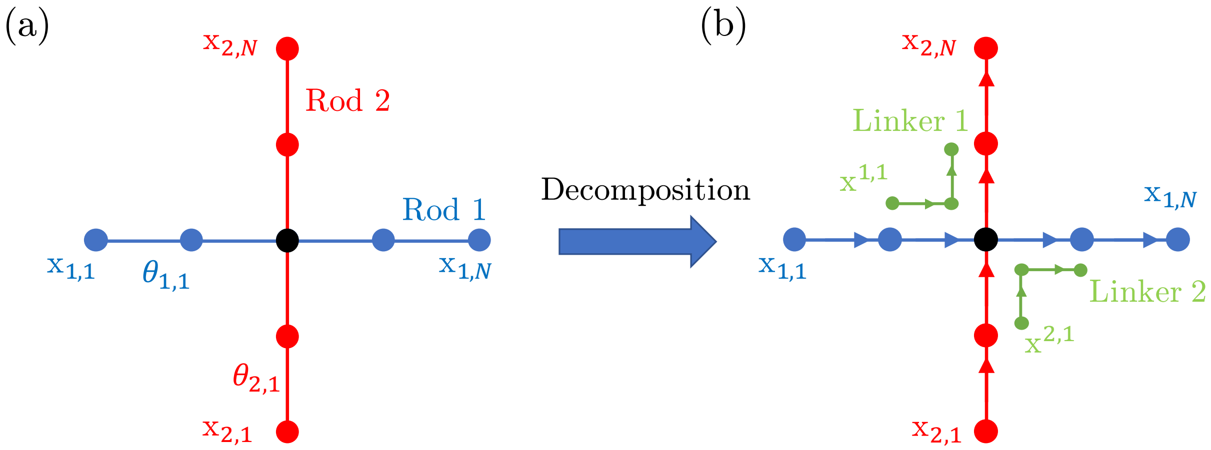

Figure 7.2: Schematic of geometric decomposition of gridshell. The configuration of gridshell (a) before decomposition and (b) after decomposition.

We consider a basic element of the gridshell in Fig. 7.2(a), where two rods intersect each other at a shared point. The position of the j-th node on the i-th rod within the gridshell system is denoted as $\mathbf{x}_{i,j}$. The twist angle of the j-th edge on the same rod is $\theta_{i,j}$. In Fig. 7.2(a), the two nodes, $\mathbf{x}_{1,3}$ and $\mathbf{x}_{2,3}$, from two different rods overlap at the joint. A straightforward method to enforce the coincidence of two nodes at the joint is a linear spring-like energy of the form

$$E_c = \frac{1}{2} C \|\mathbf{x}_{1,3} - \mathbf{x}_{2,3}\|^2, \tag{7.1}$$

where C is the Lagrange multiplier. Its negative gradient, $-\partial E_c / \partial \mathbf{q}$, can be treated as an external force in standard rod simulation. The Hessian of this energy can be trivially computed to aid the Newton's method in the solution of the equations of motion. An alternative approach to enforce this condition will be discussed next.

In addition to the coincidence of two nodes, there is a non-trivial coupling between the twisting and bending modes at the joints, e.g., twisting rod 1 in Fig. 7.2(a) can cause rod 2 to rotate. Here, we consider the pin-joints with a specific constraint for rotations at the contact area. To account for this coupling at the joints, we decompose the basic gridshell element into four elastic rods in Fig. 7.2(b): the first two are the *physical* rods denoted as rod 1 and 2; the other two are *linker* rods with 3 nodes to model the joints. Hereafter, we use subscripts to denote quantities associated with the physical rods, e.g., $\mathbf{x}_{1,1}$ is the first node on the first rod, and superscripts when associated with linker rods, e.g., $\mathbf{x}^{1,1}$ is the first node on Linker 1. Each rod can be simulated by the conventional DER method. A penalty energy can be used to account for the coupling between twisting and rotating at the joints. For the first linker and the first physical rod, the penalty energy is

$$E_c' = \frac{1}{2}C_1\|\mathbf{x}_{1,2} - \mathbf{x}^{1,1}\|^2 + \frac{1}{2}C_1\|\mathbf{x}_{1,3} - \mathbf{x}^{1,2}\|^2 + \frac{1}{2}C_2\|\theta_{1,2} - \theta^{1,1}\|^2, \tag{7.2}$$

where C_1 and C_2 represent the stiffness of the joint against the rotation and twist coupling. A similar penalty energy exists between the first linker and the second physical rod. At sufficiently high values of C_1 and C_2, the rods at the joint cannot twist or rotate with respect to one another. We use $C_1 = C_2 = 10^6 EI$ in the current numerical investigation after a convergent study [124]. The external force and Jacobian associated with these energies can again be trivially computed. We should keep in mind that, when we decompose the basic element of the gridshell structure into two rods and two linkers, the mass and stiffness of the rods at the joint should not be double counted, e.g., the lumped mass at the joint node should be divided by four and then used as the mass associated with $\mathbf{x}_{1,3}$, $\mathbf{x}_{2,3}$, $\mathbf{x}^{1,2}$, and $\mathbf{x}^{2,2}$.

In our numerical implementation, at every time step, the equations of motions for the physical and linker rods are independently solved. This allows us to take advantage of the banded nature of the Jacobian matrix. The penalty forces in Eqs. (7.1-7.2) are then calculated and included as external force in the next time step, i.e., the penalty forces are treated explicitly. An alternative to this approach of solving a number of smaller systems and subsequently bringing them together is to solve a large system, consisting of all the physical and linker rods, with an implicit treatment of the penalty forces. The large system would no longer have a banded Jacobian matrix since the Hessian matrix of the penalty energies would occupy non-banded entries within the Jacobian. A second alternative is to forego the use of penalty energies and treat the overlapping nodes (e.g., $\mathbf{x}_{1,3}$, $\mathbf{x}_{2,3}$, $\mathbf{x}^{1,2}$, and $\mathbf{x}^{2,2}$) and edges (e.g., $\theta_{1,2}$ and $\theta^{1,1}$) with the same degrees of freedom. For example, instead of using 3×4 degrees of freedom for the overlapping nodes in Fig. 7.2(b), we can introduce 3 degrees of freedom, $\mathbf{x}_{\text{joint}}$, for the joint node and apply the sum of forces from all the four nodes onto the newly introduced single node. A simulation code developed for one method can be easily re-purposed to employ a different method. While solving extremely large systems, correct choice of the time integration scheme may depend on the computer memory as well as the degree of parallelism. A detailed comparison among the explicit method (used in the current study), implicit method, and the mapping method can be found in Ref. [124].

7.2.2 Modified Mass Method

In Fig. 7.3(a), the target rigid shape is described by the function $z = f(x, y)$. The position of a node, $\mathrm{x}_i(t_k)$, in a discrete gridshell structure at time $t = t_k$, approaches the target rigid surface, $z = f(x, y)$. If the rigid surface is not accounted for, the position of this node at the next time step is, say, $\mathrm{x}'_i(t_{k+1}) \equiv [x_0, y_0, z_0]$. In the time marching scheme of the simulation, if this node falls under the target surface so that

$$z_0 < f\left(x_0, y_0\right), \tag{7.3}$$

a *correction* is required to move $\mathrm{x}'_i(t_{k+1})$ onto the target surface along the the surface normal vector,

$$\mathbf{p}_n(x_0, y_0) = \left[-\frac{\partial f(x_0, y_0)}{\partial x_0}, -\frac{\partial f(x_0, y_0)}{\partial y_0}, 1 \right], \tag{7.4}$$

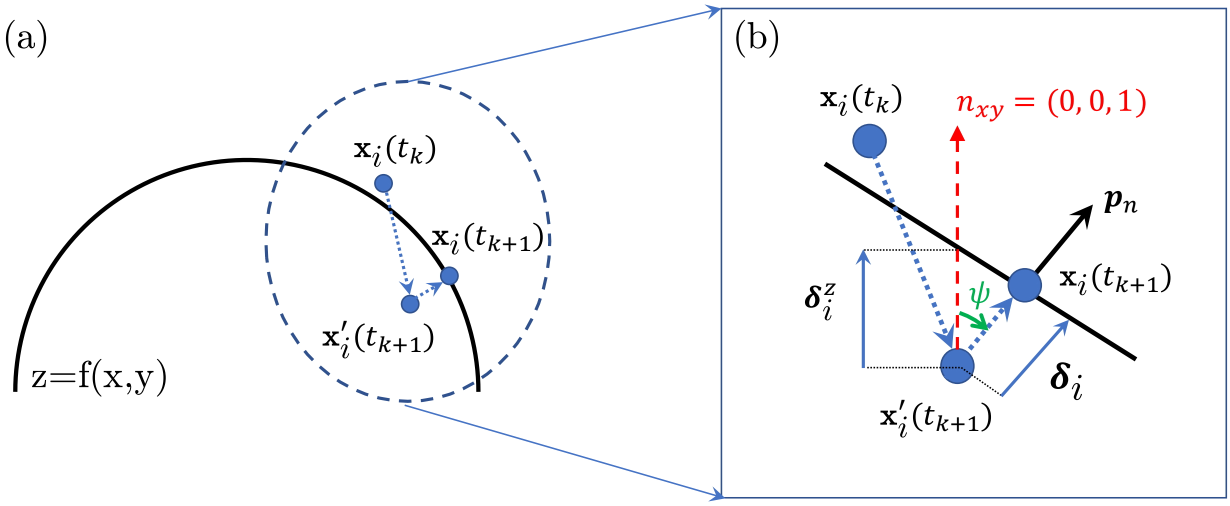

Figure 7.3: (a) Notations and schematic used in modified mass-based contact method. (b) Zoom in figure of (a).

and the necessary displacement vector for correction is

$$\boldsymbol{\delta}_i = \|\boldsymbol{\delta}_i^z\| \cos\psi \frac{\mathbf{p}_n}{\|\mathbf{p}_n\|}, \tag{7.5}$$

where $\boldsymbol{\delta}_i^z = [f(x_0, y_0) - z_0]\, \mathbf{n}_{xy}$, $\|\mathbf{p}_n\|$ is the magnitude of the vector $\mathbf{p}_n$, and ψ is the angle between $\mathbf{n}_{xy}$ (the normal vector to the $x-y$ plane) and $\mathbf{p}_n$ (the surface normal vector), as shown in Fig. 7.3(b).

In order to enforce this displacement, the equations of motion for the nodal positions have to be slightly modified. For the three degrees of freedom at the i-th node, $\mathbf{x}_i = [x_i, y_i, z_i]$, the updated form is

$$\Delta\dot{\mathbf{x}}_i(t_{k+1}) - \frac{h}{m_i}\mathbf{S}_i(t_{k+1})\left[\mathbf{F}_i^{\text{int}}(t_{k+1}) + \mathbf{F}_i^{\text{ext}}(t_{k+1})\right] - \Delta\mathbf{v}_i^{\text{pre}}(t_{k+1}) = \mathbf{0}, \tag{7.6}$$

where m_i is the lumped mass; $\Delta\mathbf{v}_i^{\text{pre}}$ is the prescribed change in velocity that can be obtained from the prescribed displacement, $\boldsymbol{\delta}_i$; $\mathbf{F}_i^{\text{int}}$ is the 3-element elastic force vector on the i-th node; $\mathbf{F}_i^{\text{ext}}$ is the external force vector; and the modified mass matrix is

$$\mathbf{S}_i = \begin{cases} \mathbb{I} & \text{if free DOF of } i\text{-th node } = 3, \\ (\mathbb{I} - \frac{\mathbf{p}_n \mathbf{p}_n^T}{||\mathbf{p}_n||^2}) & \text{if free DOF of } i\text{-th node} = 2, \\ (\mathbb{I} - \frac{\mathbf{p}_n \mathbf{p}_n^T}{||\mathbf{p}_n||^2} - \frac{\mathbf{q}_n \mathbf{q}_n^T}{||\mathbf{q}_n||^2}) & \text{if free DOF of } i\text{-th node} = 1, \\ \mathbf{0} & \text{if free DOF of } i\text{-th node} = 0, \end{cases} \tag{7.7}$$

where $\mathbb{I}$ is the 3×3 identity matrix; $\mathbf{p}_n$ is the constrained direction when free DOF=2; and $\mathbf{p}_n$ and $\mathbf{q}_n$ are the constrained directions when free DOF=1. Note that when a node is free, $\Delta \mathbf{v}_i^{\text{pre}} = \mathbf{0}$. If the node is fully constrained ($\mathbf{S}_i = \mathbf{0}$), Eq. (7.7) reduces to $\Delta \dot{\mathbf{x}}_i(t_{k+1}) - \Delta \mathbf{v}_i^{\text{pre}}(t_{k+1}) = \mathbf{0}$ and the change in position (as well as the velocity) is enforced to take the prescribed value. In our case, we only constrain the node along surface normal, $\mathbf{p}_n$, such that the number of free DOFs of the i-th node is 2. In our numerical implementation, we employ inelastic collision between the i-th node and the target 3D surface, i.e., once the node is in contact with the target surface, we manually set its velocity to zero at the end of the current time step.

Every time step in simulation accounting for the contact with a rigid surface may require integration of the equations of motion twice. The first solve is the predictor step that determines if any node fell under the target surface. The optional second solve is the corrector step that is only necessary if any node was detected to fall through the rigid surface.

7.3 Results

7.3.1 Demonstration of Bending and Twisting Coupling

We use two simple demonstrations to show the coupling between two rods at the joint. In Fig. 7.4(a), we show the response of the basic element of a gridshell when one rod is twisted. The first twist angle of one rod, $\theta_{1,1}$, referring to Fig. 7.4(a), is rotated with a prescribed angular velocity, $\omega = 10$rpm, such that $\theta_{1,1}(t) = \omega t$. Due to the two linkers

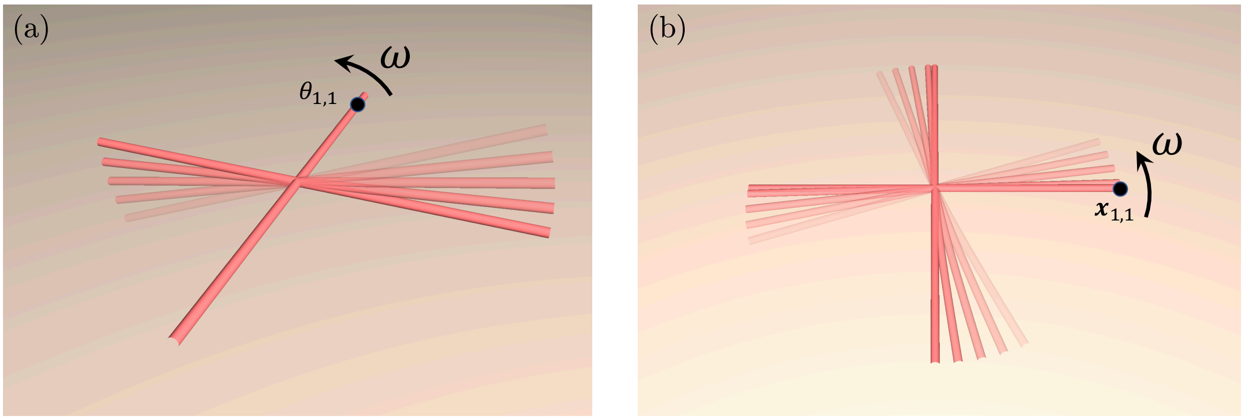

Figure 7.4: Illustration of non-trivial coupling between two intersected rods at joint. (a) twisting coupling; (b) bending coupling.

at the joint, the centerline of the other rod rotates about the former one with the same angular velocity ω. This demonstrates the twisting coupling between two rods.

We now turn to bending coupling in Fig. 7.4(b) and specify the position of the first node of the first rod, $\mathbf{x}_{1,1} \equiv [x_{1,1}(t), y_{1,1}(t), z_{1,1}(t)]$, highlighted in Fig. 7.4(b), where

$$x_{1,1}(t) = \frac{1}{2} L \cos \omega t, \tag{7.8a}$$

$$y_{1,1}(t) = \frac{1}{2} L \sin \omega t, \tag{7.8b}$$

$$z_{1,1}(t) = 0, \tag{7.8c}$$

L is the total length of the undeformed rod, and $\omega = 10$rpm. The location of the middle node on the first rod that falls on the joint is kept fixed with time to avoid rigid body motion. Due to these fixed degrees of freedom, the first rod rotates about the z-axis with a prescribed angular velocity ω. Also, because of the coupling of bending between two rods at the joint, the second rod also rotates about the z-axis at the same angular velocity.

7.3.2 Initial Boundary from the Draping Method

Three target shapes – hemisphere, paraboloid, and hemi-ellipsoid shapes – are used as examples to demonstrate the form-finding process of gridshell structures. The physical parameters are: rod length $s = 1.2$m, rod radius $r_0 = 1$mm (and, therefore, second mo-

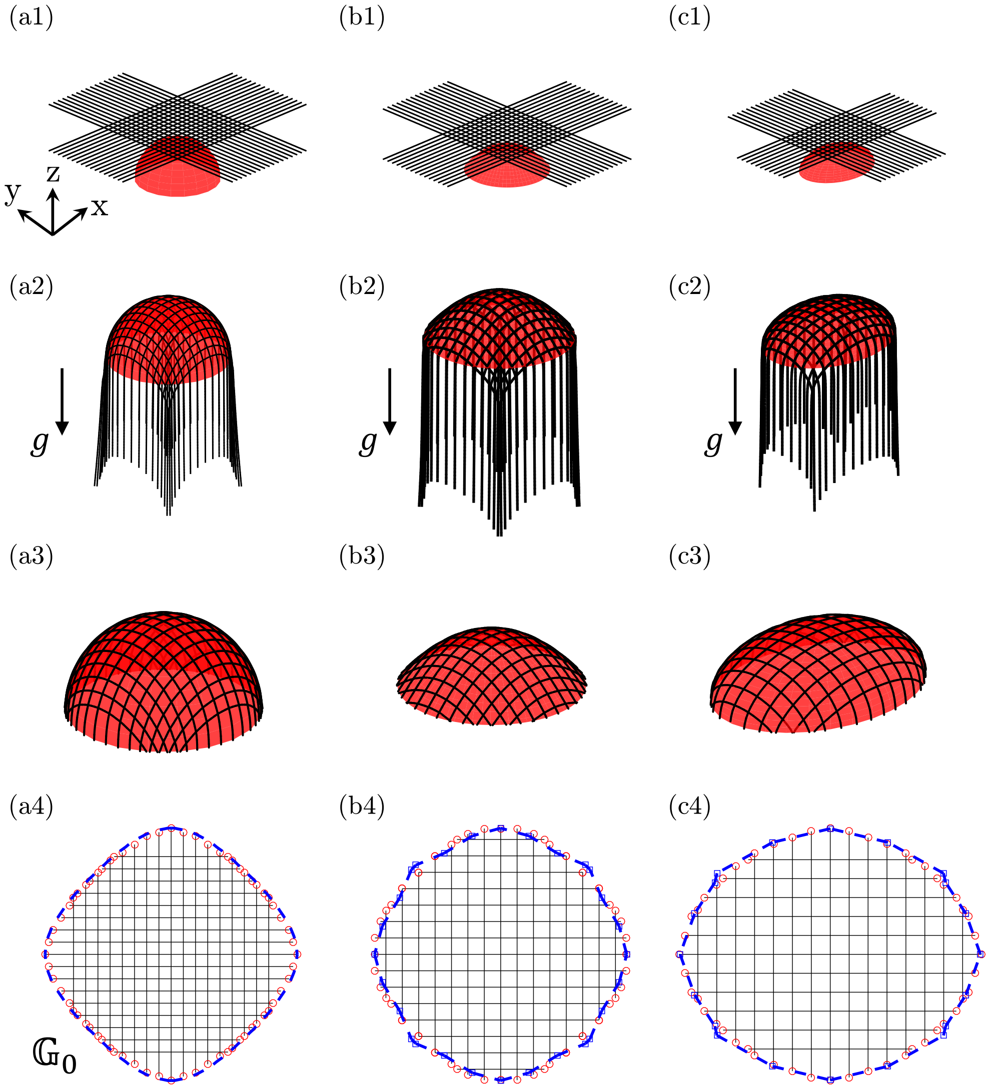

Figure 7.5: Form-finding process of gridshells: (a) hemisphere; (b) paraboloid; and (c) hemi-ellipsoid. (1) Initial setup of planar gridshells and target 3D surfaces. (2) Deformed configuration of the gridshells on the rigid surfaces. (3) Gridshells after trimming. (4) Initial planar shapes after mapping the trimmed gridshell onto the undeformed planar shape. The dashed line in (a4) is the analytical solution [17], and the ones in (b4) and (c4) are from the genetic algorithm-based optimization in Ref. [124].

ment of inertia, $I = \pi r_0^4/4$, polar moment of inertia, $J = \pi r_0^4/2$, and cross sectional area $A = \pi r_0^2$), Young's modulus $E = 1$MPa, shear modulus $G = E/3$ (assuming incompressible material), material density $\rho = 1.0$g/cm^3, distance between two parallel rods $\Delta s = 3$cm, discrete edge length $\|\bar{\mathrm{e}}\| = 5$mm, and distance between planar X-shell and 3D surface top (choosing arbitrarily) is $H = 5$cm. As long as the rod can be assumed to be soft enough

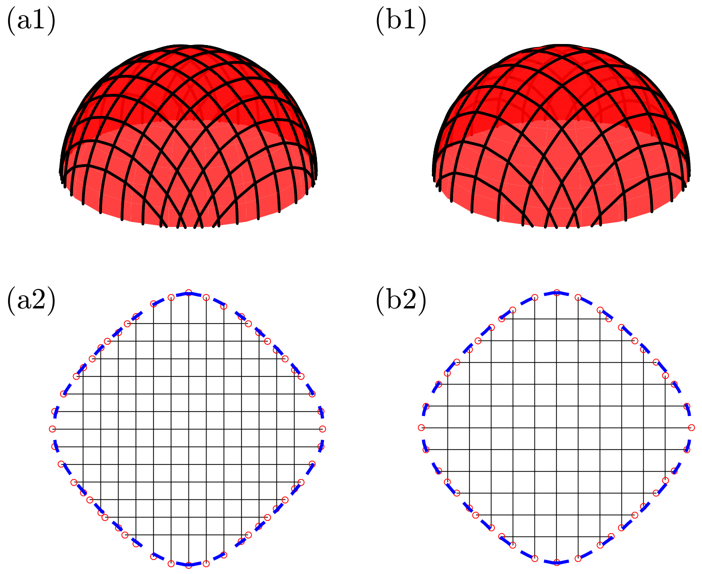

Figure 7.6: (a) Hemispherical gridshells with different grid spacing. (b) Their corresponding initial planar shapes. (1) hemispherical grid with $\Delta s = 4$cm; (2) hemispherical grid with $\Delta s = 5$cm.

and inextensible, these parameters do not significantly influence the actuated shape of the gridshell [17]. The geometries of the target surfaces are given by

$$\Gamma_1(x,y,z): \frac{x^2}{R_h^2} + \frac{y^2}{R_h^2} + \frac{z^2}{R_h^2} = 1, \text{ with } 0 \leqslant x^2 + y^2 \leqslant R_h^2 \text{ and } z \geqslant 0, \tag{7.9a}$$

$$\Gamma_2(x,y,z): \frac{x^2}{R_p^2} + \frac{y^2}{R_p^2} + \frac{z}{H_p} = 1, \text{ with } 0 \leqslant x^2 + y^2 \leqslant R_p^2 \text{ and } z \geqslant 0, \tag{7.9b}$$

$$\Gamma_3(x,y,z): \frac{x^2}{a_e^2} + \frac{y^2}{b_e^2} + \frac{z^2}{c_e^2} = 1, \text{ with } 0 \leqslant \frac{x^2}{a_e^2} + \frac{y^2}{b_e^2} \leqslant 1 \text{ and } z \geqslant 0, \tag{7.9c}$$

where $R_h = 0.2$m (for hemisphere); $R_p = 0.2$m and $H_p = 0.12$m (for paraboloid); $a_e = 0.2$m, $b_e = 0.15$m, and $c_e = 0.12$m (for hemi-ellipsoid).

In Fig. 7.5(a1-c1), the undeformed planar gridshells are located above the 3D rigid surfaces described by Eqs. (7.9). The elastic rods are symmetrically distributed about the x and y-axes in case of the hemisphere (17×17 grid) and the paraboloid (15×15 grid); for the hemi-ellipsoid, on the other hand, there are 11 rods along the x-axis and 15 along the y-axis. Note that the rod number for each case is determined by the size of the desired shapes, i.e., we want at least one node on each rod to contact the target surface. The planar gridshells are dropped under a gravity-type load that is large enough to drape the structure around the target rigid surface. In Fig. 7.5, gravitational acceleration of $g = 9.81$ m/s^2 was sufficient. Fig. 7.5(a2-c2) shows the deformed shapes of the gridshells. Parts of the gridshell are in contact with the rigid surface (located above the $x - y$ plane) and the other parts remain suspended under gravity below the $x - y$ plane. The suspended parts (i.e., nodes that fall below the minimum z-coordinate of the target rigid shape) are *trimmed* in Fig. 7.5(a3-c3) to obtain the new extremities (first and last nodes) on each elastic rod. This describes the final boundary $\mathbb{G}$ of the form-finding problem (also see Fig. 7.1). In Fig. 7.5(a4-d4), the extremities upon trimming are mapped back to the initial planar gridshell, i.e., the planar shape is also trimmed to get rid of the suspended portions. This gives the initial boundary, $\mathbb{G}_0$, of the gridshell. Then, the target 3D pattern described in Eqs. (7.9) can be obtained by moving the nodes on the extremities of the rods from the initial footprint, $\mathbb{G}_0$, to the final boundary, $\mathbb{G}$. As the gravitational force is more dominant compared with the bending force, the deformed shape of elastic gridshell predicted by the contact-based method does not vary a lot for joints with different stiffness.

The analytical solution to the initial boundary in case of a hemisphere [17] is also shown in Fig. 7.5(a4). For the cases of paraboloid and hemi-ellipsoid, the analytical solutions are not easy to derive and, therefore, we compare the planar boundaries obtained from the draping process and the ones found by genetic algorithm-based optimization [124] in Fig. 7.5(b4) and Fig. 7.5(c4). The good match indicates the correctness and the validity of the proposed method. Even when the solution from the process outlined in Fig. 7.5 is not accurate enough, it provides an excellent initial guess for conventional optimization algorithms.

For a physical understanding of this method, we consider the balance of forces. Each node in the simulation is balanced by three forces: (1) gravity, (2) contact force from the target rigid surface, and (3) elastic forces (primarily bending). This competition of forces yields a deformed shape that conforms to the target surface. On the other hand, in the "pop-up" fabrication process [17] of gridshell where the nodes on $\mathbb{G}_0$ are moved to $\mathbb{G}$, gravity and contact forces are replaced by forces acting on the extreme nodes (located

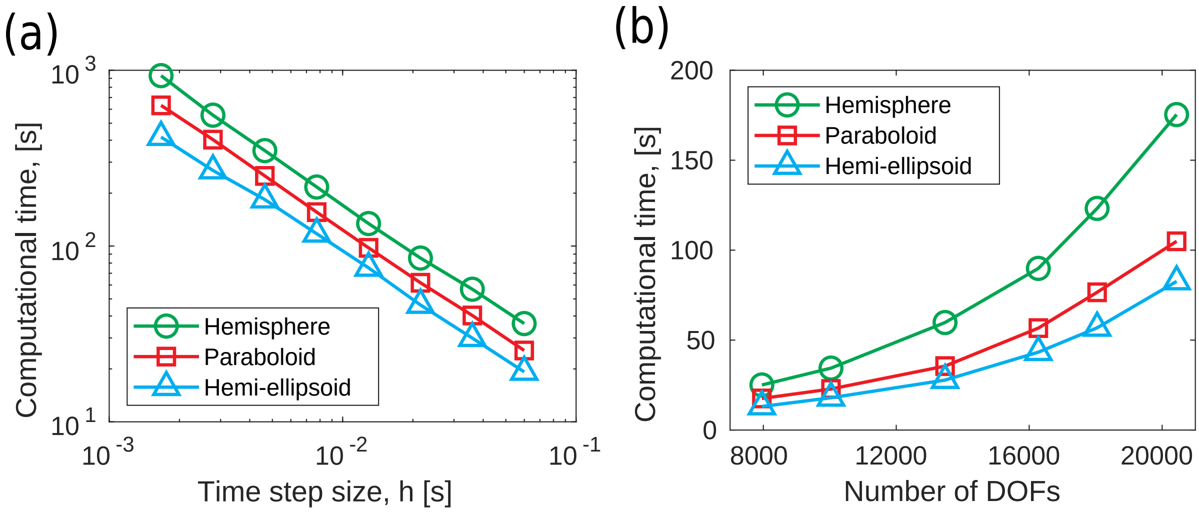

Figure 7.7: Computational time as a function of (a) time step size and (b) number of DOFs for three cases, (i) hemisphere, (ii) paraboloid, and (iii) hemi-ellipsoid.

on the boundary) by an external agent. Our results show that, surprisingly, the deformed shape remains almost the same despite substitution of gravity and contact with boundary conditions on a handful of nodes. Next, to demonstrate that the numerical method is robust against initial grid spacing, in Fig. 7.6(a) and (b), we show the hemispherical gridshell with different grid spacings. Here, the distance between two parallel rods are $\Delta s = 4$cm (for Fig. 7.6(a)) and $\Delta s = 5$cm (for Fig. 7.6(b)); the rod number is changed to 13×13 and 11×11, respectively, to ensure that each rod comes in contact with the target surface. As shown in Fig. 7.6(a2) and Fig. 7.6(b2), the initial planar grids match well with the analytical solution in both of these two cases.

7.3.3 Computational Time

Next, we highlight the computational efficiency of the presented contact-based numerical simulation in elastic gridshells. In Fig. 7.7(a), we plot the computational time as a function of time step size, h, for three different cases. Here, the DOFs number for all scenarios is fixed as ~ 8000. The total simulation times are 50s (for hemisphere), 30s (for paraboloid), and 20s (for hemi-ellipsoid), separately. On the other side, referring to Fig. 7.7(b), we show the reliance of the computational time on the number of DOFs. The time step size in this figure is set to be $h = 0.1$s. Unsurprising, computational time dramatically increases as the enlargement of the total DOFs. The simulations are performed on a single thread of Intel Core i7-6600U Processor @ 3.4 GHz. Overall, reasonable predictions can be obtained within one minute.

7.4 Summary and Outlook

We introduced a numerical framework for the simulation of gridshells and solved the form-finding problem directly, without any numerical optimization. For the forward physical simulation, we first decomposed the gridshell as well as its joints into multiple elastic rods, such that each component can be treated using the well-established DER method. For the inverse problem of form-finding, we formulated a modified version of the discrete gridshell simulation algorithm by coupling it with the modified mass method to account for the contact between an elastic gridshell and the target rigid 3D surface. We showed that the gridshell, upon draping around the target shape, can be simply trimmed to directly get the initial planar boundary. A good match between the analytical solution and the contact-based result in case of a hemispherical target shape indicates the potential use of our method in form finding problems. Here, we limited ourselves within the convex surfaces with analytical solutions. The shape construction for arbitrary surfaces may need to introduce the frictional contact between the stretchable gridshells and target surfaces. We hope that our results and methodology will instigate future work on buckling induced mechanically guided assembly in physical systems (e.g., pop-up actuation of a planar grid to a target shape) from macro scale (e.g., domes in architecture) to micro scale (e.g., controlled buckling of slender rods for stretchable electronics).

CHAPTER 8

Shear Induced Supercritical Pitchfork Bifurcation of Pre-buckled Bands

We combine discrete differential geometry (DDG)-based models and desktop experiments to study the supercritical pitchfork and bifurcation phenomena of a pre-compressed elastic plate under lateral end translation, with a focus on its width effect. Based on the ratio among length, width, and thickness, the elastic structures in our study fall into three different structural categories: rods, ribbons, and plates. In order to numerically simulate the mechanical response of these structures, we employ two DDG-based numerical frameworks – Discrete Anisotropic Rods method and Discrete Elastic Plates method. Even though the multi-stability and bifurcation of a narrow strip can be precisely captured by a naive one dimensional rod model, it fails to match with experiments as the ribbon increases in width. A two dimensional approach using a plate model, on the other hand, accurately predicts the geometrically nonlinear deformations and the supercritical pitchfork points for plates even when the width is as large as half of the length. Exploiting the efficiency and robustness of the simulator, we perform a systematic parameter sweep on plate size and lateral displacement to build a phase diagram of different configurations of the elastic plates. We find that the deformed configuration of the nearly developable strips can be described, up to a very good approximation, using the bending and twisting of the centerline. This indicates that a one dimensional energy model for the simulation of nearly developable strips can potentially be developed in the future. The results can serve as a benchmark for future numerical investigations into modeling of ribbons. Our study can also provide guidelines on the choice of the appropriate structural model – rod vs. ribbon vs. plate – in simulation of thin elastic structures.

We introduce the underlying motivation and relevant literatures in § 8.1. The experimental setup is detailed in § 8.2, then followed by the numerical simulation procedure § 8.3. Next, we discuss the results in § 8.4. The summary is presented in § 8.5. The content of this chapter has appeared in Ref. [126].

8.1 Motivation

Thin elastic structures, e.g., narrow rods and wide plates, can perform complex mechanical response when subjected to simple boundary conditions or moderate external forces. The behavior is in the geometrically nonlinear regime, like buckling instability, which makes these structures suitable for the design of advanced metamaterials and intelligent systems [127]. Specifically, snapping and bifurcation, i.e., a swift transformation process between multiple phases in response to external loading, exist in both artificial and natural systems, including slap bracelet [128], Venus flytrap [129], toy poppers [130], and robotics [5]. Previous investigations of snap buckling mainly focused on one dimensional rod or ribbon-like system under different loading and boundary conditions, e.g., asymmetrical constraints [131, 132], stretching [133, 134], twisting [135], shearing [136], and out-of-plane compression [137, 138]. Even though the buckling instability and post-buckling behavior in two dimensional curved surfaces, such as cylinder [139, 140] and sphere/hemisphere [139, 141], have previously been studied, the mechanics behind the transverse shear induced bifurcation in wide strips remains uncovered, i.e., the gap between narrow strips and wide plates has not yet been systematically investigated [136]. This chapter presents a general point of view on the shear induced bifurcations of prebuckled plates, from narrow to wide. Here, we consider the following definitions: a rod is a one dimensional object; a ribbon is a narrow two dimensional developable surface; a plate is a two dimensional surface that allows both bending and stretching. In Fig. 8.1, we provide some snapshots of elastic plates in different topologies from both desktop experiments and numerical simulations. We start with a narrow strip (length $L \gg$ width W $\gg$ thickness b), then gradually increase its width that satisfies $L \sim W \gg b$ to reveal the relations between one dimensional anisotropic Kirchhoff rod model and two dimensional

Föppl-von Kármán plate equations, for a fundamental understanding of the mechanics of a class of thin elastic structures.

A straightforward approach to study the narrow strip is by a one dimensional Kirchhoff rod model [136], and there are much prior investigations on Kirchhoff equations, e.g., Antman [142, 143], Maddocks [144], Nizette and Goriely [145], and Ameline et al. [146]. Moreover, previous analytical, numerical, and experimental studies showed different deformed configurations of one dimensional rod-like structures in both isotropic cross section [147] and anisotropic cross section [136, 135]. However, a strip with developable surface assumption would behave fundamentally differently compared with a naive rod model [148]. Sadowsky first derived an one dimensional energy functional for a narrow ribbon ($L \gg W \gg b$) [21], and his work was later generalized by Wunderlich to account for finite width [22]. Their dimensional reduction was made possible by focusing on developable configurations of the ribbon, which are preferred energetically in the thin width limit. Developable surfaces are special cases of ruled surfaces, i.e., they are spanned by a set of straight lines called generatrices or rulings: the one dimensional elastic energy functional in Wunderlich's formulation is based on a reconstruction of the surface of the ribbon in terms of its centerline, and of the angle between the generatrices and the centerline tangent [19]. Next, the equilibrium problem of ribbon structures can be solved by principle of virtual work and variational method. Starostin and van der Heijden found the equilibrium equations for naturally flat rectangular ribbons [148], and later extended to helical shapes [133]. Dias et al. summarized developable ribbon model into a generalized energy functional, with the consideration of non-zero curvatures in both out-of-plane and in-plane (geodesic) directions, such that the same model can describe both a rectangular ribbon and an annular ribbon [19]. Their analytical work treated the ribbon as a special case of a thin rod, with an internal parameter and kinematic constraints, and these specificities could be incorporated naturally into the classical theory of thin rods [1]. However, all these investigations are under the assumption that the surface is developable, such that the stretching energy is forbidden during the deformed process. A two dimensional approach, on the other hand, allows the stretching strain in the middle surface of plate,

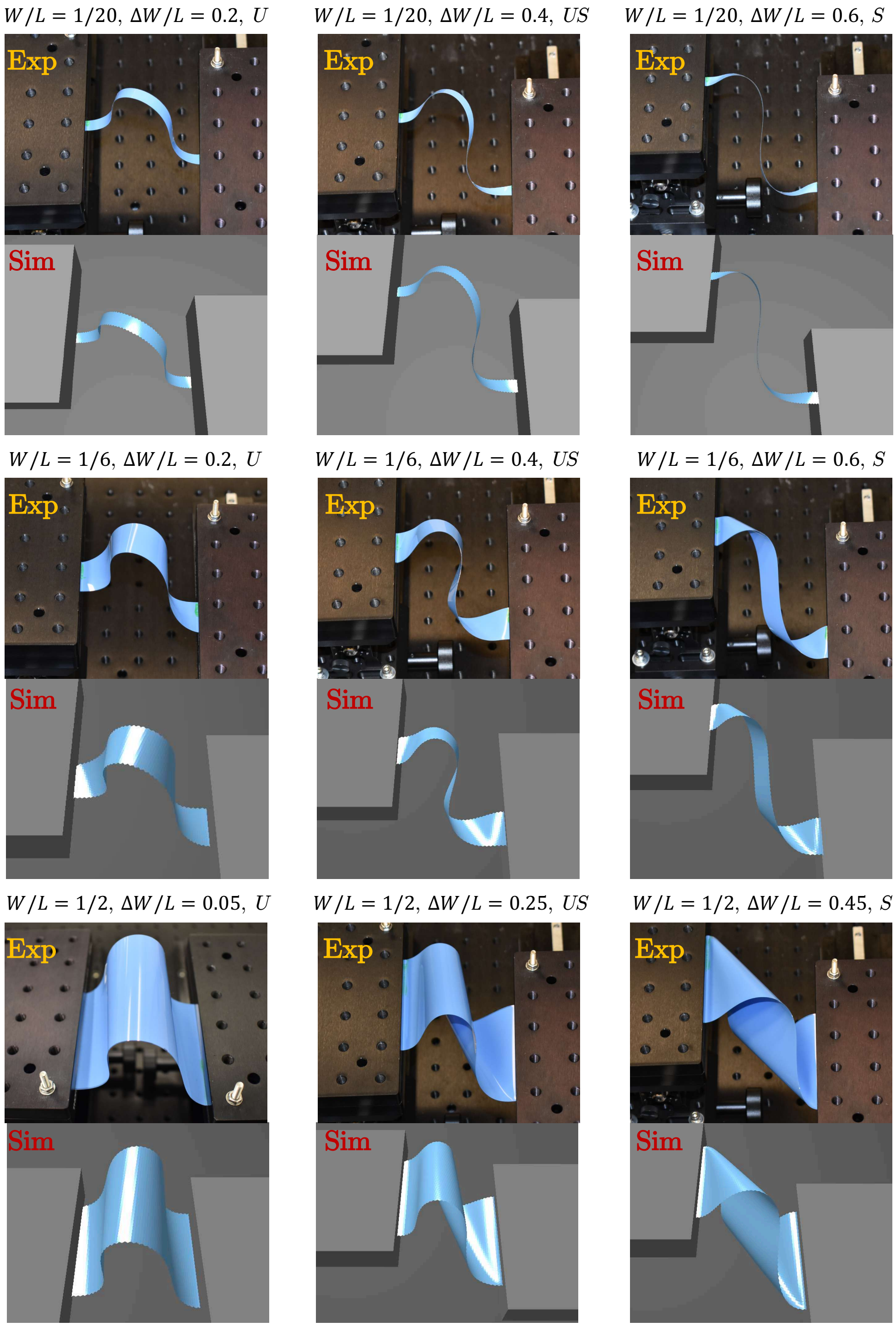

$W/L = 1/20$, $\Delta W/L = 0.2$, U

$W/L = 1/20$, $\Delta W/L = 0.4$, US

$W/L = 1/20$, $\Delta W/L = 0.6$, S

$W/L = 1/6$, $\Delta W/L = 0.2$, U

$W/L = 1/6$, $\Delta W/L = 0.4$, US

$W/L = 1/6$, $\Delta W/L = 0.6$, S

$W/L = 1/2$, $\Delta W/L = 0.05$, U

$W/L = 1/2$, $\Delta W/L = 0.25$, US

$W/L = 1/2$, $\Delta W/L = 0.45$, S

Figure 8.1: Snapshots of elastic plates in different topologies (U, S, US) from both desktop experiments and numerical simulations. Here, the pre-compressed distance is $\Delta L/L = 1/2$.

and is preferred when studying the typology of Möbius strip [149] and patterns in helical ribbon [150, 151], whose stretching energies are no longer trivial compared with bending energies.

Here, we combine tabletop experiments with DDG-based simulations to study the effect of width on the mechanical response of a pre-compressed (i.e., longitudinally displaced) elastic plates under lateral displacement (i.e., transverse shear). We aim to quantify the transition of the mechanics of these plates from a rod-like behavior to a plate-like response, as the width increases. Towards that end, we employ two DDG-based numerical frameworks: Discrete Anisotropic Rods (DAR) that simulates a rod based on the deformation of the one-dimensional centerline and Discrete Elastic Plates (DEP) that models the two-dimensional plate. Side by side with simulations, we record the deformation of a number of plates of varying widths under prescribed longitudinal displacement and transverse shear. Longitudinal displacement is first applied to buckle the plates and this pre-buckled plates is then subjected to lateral displacement (i.e., transverse shear), resulting in a number of qualitatively distinct deformed shapes. Excellent agreement is found between DEP simulations and desktop experiments. In addition to the rod and plate simulations, we also implement a discrete Sadowsky model for narrow developable ribbon. Interestingly, in our numerical framework based on balance of forces at each degree of freedom, the Sadowsky model does not capture the shear induced supercritical pitchfork in the pre-stressed narrow ribbons. However, both one dimensional rod model and two dimensional plate simulation can give reasonable predictions compared with experimental observations. On the other side, the Sadowsky model does give a reasonable prediction if an initial solution is provided, where this initial solution can be obtained from the rod or plate simulation. Not so surprisingly, we observe that the curvatures computed by the Sadowsky model are discontinuous at the inflection points where the bending curvatures are zero.

8.2 Experimental Setup

In Fig. 8.2, we show the experimental setup and boundary conditions used in the current study. The setup is similar to a recently published study [136]. The span between two slide

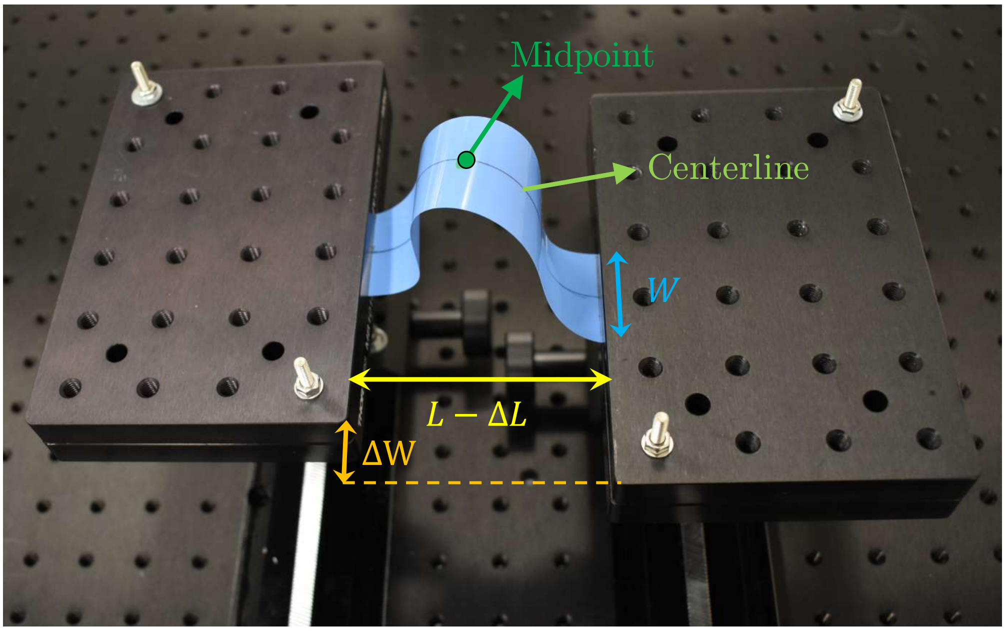

Figure 8.2: Experimental setup. A rectangular plate of width W and length L is symmetrically clamped. The longitude compression is ΔL and the transverse displacement is ΔW.

rails is fixed at $L - \Delta L = 75$mm for convenience, where $L \in \{100, 150\}$mm is the length of the plates and ΔL is the transverse displacement to pre-compress the structure. The inclined angle of clamped end is a constant, $\psi = 0.0°$. The plates were cut from polyester shim stock (Artus Corp., Englewood, NJ) with a thickness of $b = 0.127 \pm 0.013$mm [136], such that the length to thickness ratio is $L/b \in \{787, 1181\}$. A variety of specimens were prepared with different lengths and widths such that $\Delta L/L \in \{1/2, 1/4\}$ and $W/L \in \{1/2, 1/3, 1/6, 1/12, 1/20\}$. In the anisotropic rod model, we describe the plates in terms of its centerline, which is most suitable for narrow strip, while quite distinct from the description of the wide plates – a surface in two dimension. The height of structural midpoint, marked as green dot in Fig. 8.2, is used to quantify the deformed configurations in elastic strip. The experimental data point is extracted using ImageJ, a Java-based image processing program. A strip with finite width has a shear limit that imposes an upper bound on the lateral displacement, $\Delta W_{\max}$. As a result, we maintain $\Delta W \in [0, \Delta W_{\max}]$ in both experiments and simulations to avoid damage to the plates as well as numerical convergence issues. Since this is a geometry dependent problem, the material parameter

(Young's modulus) does not play any role. In our simulations, the Young's modulus was set to $Y = 100\text{GPa}$.

8.3 Numerical Simulation of Elastic Plates

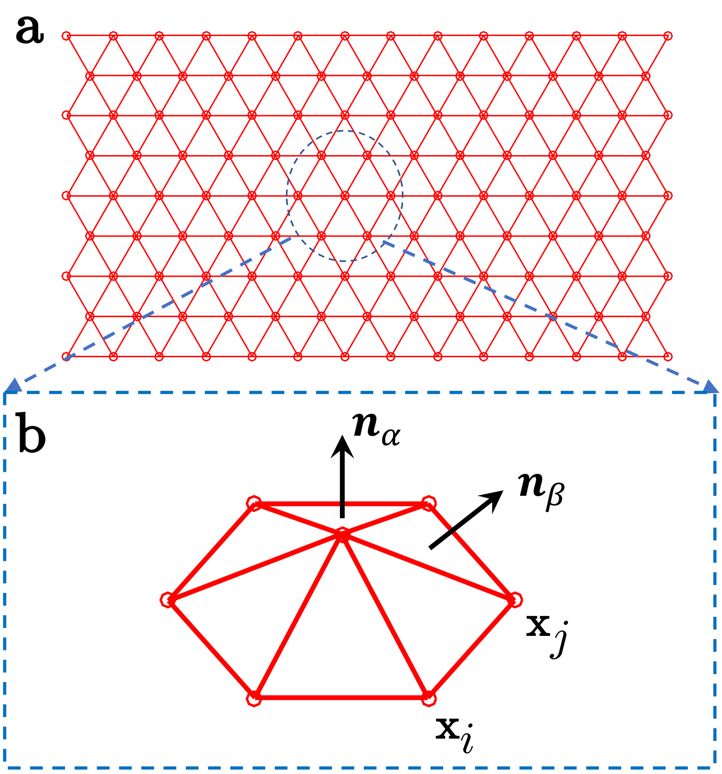

Figure 8.3: (a) Discretization of a two dimensional plate. (b) Notations used in discrete elastic plate model. Surface normal of α-th equilateral triangle mesh is $\mathbf{n}_\alpha$.

Here, we introduce a DDG-based simulation of two dimensional elastic plate. We treat the elastic plate as a mass spring system, with lumped masses at the vertices. A discrete elastic energy is associated with each vertex. In Fig. 8.3(a), the two dimensional plate is discretized into N nodes and N_{mesh} equilateral triangular faces, such that the degree of freedom vector has a size of $3N$,

$$\mathbf{q}^{\text{plate}} = [\mathbf{x}_0, \mathbf{x}_1, ..., \mathbf{x}_{N-1}] \,. \tag{8.1}$$

The total potential in two dimensional plate is the sum of the elastic stretching and bending energies [152],

$$E_{\text{s}}^{\text{plate}} = \frac{\sqrt{3}}{4} Y b \sum_{ij}^{N_{\text{edge}}} \left(\|\mathbf{e}^{ij}\| - \|\bar{\mathbf{e}}^{ij}\| \right)^2 \tag{8.2a}$$

$$E_{\text{b}}^{\text{plate}} = \frac{1}{\sqrt{3}} \frac{Y b^3}{12} \sum_{\alpha\beta}^{N_{\text{pair}}} \left(\mathbf{n}_\alpha - \mathbf{n}_\beta \right)^2 , \tag{8.2b}$$

where Y is the Young's modulus, b is the plate thickness, $\mathbf{e}^{ij} = \mathbf{x}_i - \mathbf{x}_j$ is the edge vector between i-th and j-th nodes, $\|\bar{\mathbf{e}}^{ij}\|$ is its undeformed length, N_{edge} is the total edge number in discrete plate model, N_{pair} is the total bending pairs of discrete plate (a bending pair is comprised of two neighboring triangular faces), and $\mathbf{n}_\alpha$ (and $\mathbf{n}_\beta$) is the surface normal of the α-th (and β-th) triangular face, as shown in Fig. 8.3(b). This discrete representation of the energy functional presented above has been shown to converge to the continuum limit of Föppl-von Kármán equations used to describe the nonlinear mechanics of thin plates [153, 154, 152]. The time marching scheme in elastic plate model is similar to the rod simulation, i.e., the equations of motion from time step t_k to $t_{k+1} = t_k + h$ (h is the time step size) is obtained through implicit Euler approach, and $(\mathbf{F}^{\text{int}})^{\text{plate}} = -\partial(E_{\text{s}}^{\text{plate}} + E_{\text{b}}^{\text{plate}})/\partial \mathbf{q}^{\text{plate}}$ is the internal elastic force vector in plate model. The Jacobian matrix of plate simulation is sparse but non-banded, and, as such, we cannot achieve $O(N)$ time complexity. The difference in computation between rod vs. plate simulation becomes more and more significant as the number of nodes increases. Naturally, whenever possible, a rod model is favorable over a plate model.

8.4 Results

In this section, we study the shear induced bifurcations of pre-buckled plates. We present the numerical results from both anisotropic rod model and plate model, and compare them with experimental data. We use $M = 100$ nodes for rod simulation and $N_{\text{mesh}} \approx 2000$ in plate model. In one dimensional rod model, 14 DOFs, $\left[\mathbf{x}_0, \theta^0, \mathbf{x}_1, \mathbf{x}_{M-2}, \theta^{M-2}, \mathbf{x}_{M-1}\right]$, are constrained. These DOFs correspond to the location, tangent, and rotation at two ends; this boundary condition emulates the clamped boundary at two ends. All other nodes and

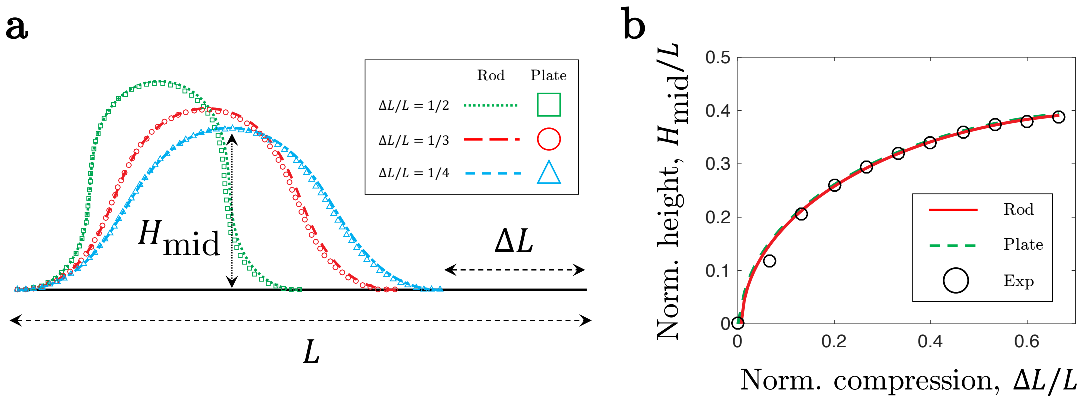

Figure 8.4: (a) Pre-buckled configurations of elastic strips obtained from (i) rod model (line) and (ii) plate model (symbolic). (b) normalized midpoint height, H_{mid}/L, as a function of actuated distance, $\Delta L/L$, from (i) rod simulation, (ii) plate simulation, and (iii) experimental data.

edges are free to evolve based on the balance of forces. For plate simulation, the nodes in the first two and last two “columns" are constrained to impose an equivalent clamped boundary condition. We briefly review the Euler buckling of elastic strip and then discuss in detail the shear induced bifurcations of the pre-buckled plate, from narrow to wide. The influence of gravity on these systems is generally weak and negligible [136], such that we keep gravity out of our frameworks. However, the effect of gravity can be easily accounted for in the discrete model as an external force.

8.4.1 Euler Elastica

The thin elastic strip would undergo buckling instability when the uniaxial compressive force exceeds a threshold; this has been studied since the days of the elastica theory of Euler in the 18th century. We review the buckled configuration of an elastic strip, and compare the simulation results from rod (DAR) and plate (DEP) models with experimental data.

Referring to the solid black line in Fig. 8.4(a), we consider a strip of length L along the x-axis. The arclength parameter of the centerline is $s \in [0, L]$. One end at $s = 0$ is fixed, and the another extremity at $s = L$ is longitudinally displaced, i.e., compressed, from $x = L$ to $x = L - \Delta L$ to induce buckling. Due to inextensibility of thin elastic strip, its midpoint height, $H_{\rm mid}$, is independent of the material properties and only related to the compressive distance ΔL, i.e., the system can be described by a naive geometric model. In simulations, the compression speed of clamped end is set to be $\Delta v_L = 1{\rm mm/s}$ to ensure quasistatic response of the structure and avoid higher order modes of dynamic buckling. In Fig. 8.4(a), we show the deformed configurations of elastic strips at different actuated distances, $\Delta L/L \in \{1/2, 1/3, 1/4\}$, from both one dimensional rod model (line) and two dimensional plate simulation (symbols). A good agreement can be found between rod and plate models, as the transverse direction (width effect) of elastic strip does not matter in this simple case of out-of-plane deformation. In Fig. 8.4(b), for a quantitative comparison between experiments and simulations, we measure the normalized midpoint height, $H_{\rm mid}/L$, as a function of the normalized compressive distance, $\Delta L/L$, from (i) rod model; (ii) plate model; and (iii) experimental data. A good match indicates the accuracy of our presented discrete models in the planar buckling case, which is a prerequisite for further investigations into 3D scenarios involving shear induced bifurcations of pre-buckled strips.

8.4.2 Maximum Shear

The shearing process tends towards limiting states, past which the sheet cannot deform without stretching somewhere [136]. In Fig. 8.5(a), we show folded strip model to represent a limiting S-like pattern, where the red dashed line indicates the incipient conical singularities forming near the clamps, the corresponding deformed configurations from experiment and simulation are in Fig. 8.5b. In the limit, these cones share a single straight line generator formed from a plate diagonal that sets the limiting shear to [136]

$$\Delta W_{\rm max} = \sqrt{L^2 + W^2 - (L - \Delta L)^2} - W. \tag{8.3}$$

8.4.3 Shear Induced Snapping of Pre-Stressed Bands

With the numerical frameworks and pre-buckled elastic strip constructed beforehand, we now turn to the main contribution of the current study and systematically investigate its supercritical pitchfork under lateral end translations. In both experiments and simulations

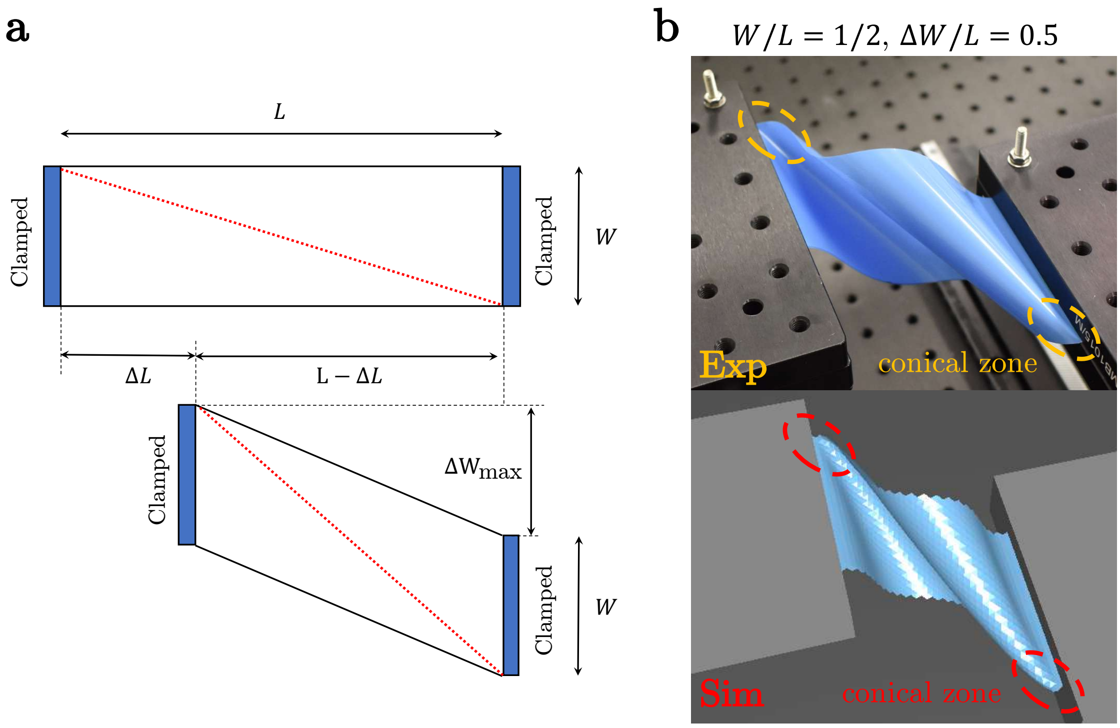

Figure 8.5: (a) Schematic diagram of the shear limit in S pattern. (b) Configurations of plate under maximum transverse shear, $W/L = 1/2, \Delta L/L = 1/2, \Delta W/L = 1/2$, from desktop experiment and numerical simulation.

(Fig. 8.1), we found that the pre-stressed U shaped strips first transitions into US configuration after the supercritical pitchfork point, next shifts to S patterns when transverse shear goes beyond the second threshold. Regarding the nomenclature of the patterns, we follow Yu and Hanna [136]. The same authors studied, using experiments and theory, the bifurcation phenomenon at the first critical translation point and reported two symmetric US ($US+$ and $US-$) patterns that later transform into S ($S+$ and $S-$) patterns [136].

We first quantitively study the shear induced bifurcations of elastic plates at a pre-compression parameter of $\Delta L/L = 1/2$. Similar to the previous trial, the transverse speed in both the rod and plate simulations is set to be $\Delta v_W = 1\text{mm/s}$ to ensure quasistatic response of structures. In Fig. 8.6, we present the evolution of the normalized midpoint height, H_{mid}/L, with the normalized transverse shear, $\Delta W/L$, at different length to width ratio, $W/L \in \{1/20, 1/12, 1/6, 1/2\}$, of the plates. When the strip is narrow, e.g., $W/L = 1/20$ in Fig. 8.6(a), the difference between anisotropic rod model and plate

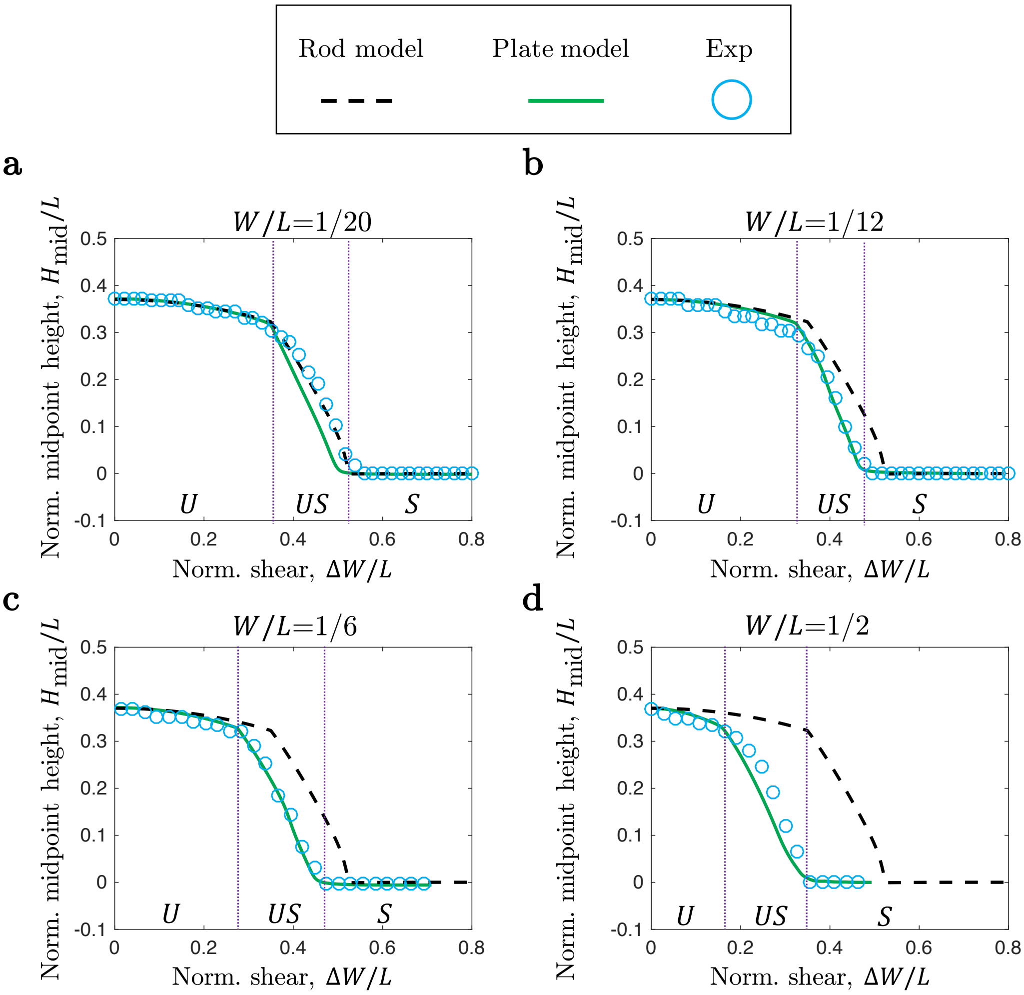

Figure 8.6: Relations between normalized midpoint height, H_{mid}/L, and normalized transverse shear, $\Delta W/L$, for plates with different width, $W/L \in \{1/20, 1/12, 1/6, 1/2\}$. Here the pre-compressed distance is $\Delta L/L = 1/2$.

framework is small, and both of them match well with experimental data. The U shaped configuration of narrow strip first goes into US configuration at $\Delta W_1/L \approx 0.36$, next transitions to S pattern after $\Delta W_2/L \approx 0.52$. These observations match previous experimental observations on extremely narrow plates, $W/L = 1/80$ [136]. As the width of the plate increases, e.g., $W/L = 1/12$ in Fig. 8.6(b), the critical values of $\Delta W/L$ at the two critical points decrease. The plate simulation matches well with experiments, while the rod model starts to show deviation from the experimental data. Nonetheless, the difference is still trivial and, given the computational efficiency of DAR, it can be the preferred simulation tool in practice at this W/L ratio. Noteworthy is the performance of the simple Kirchhoff rod model in simulating structures ($W \gg b, L \sim 10W$) that are physically different from a rod.

Width effects start to appear as the width is increased beyond $W/L = 1/12$ in Figs. 8.6(c-d). For plates with larger length to width ratio, $W/L \in \{1/6, 1/2\}$, the first critical threshold drops to approximately $\Delta W_1/L = 0.27$ and $\Delta W_1/L = 0.17$. In this regime, the rod simulations can not give accurate predictions; the two dimensional plate framework, on the other hand, successfully captures the shifts of critical points with the width in elastic strips.

The transitions between US pattern and S pattern exhibit a similar trend where the second threshold values, $\Delta W_2/L$, decreases with increasing width. This threshold value can be easily obtained from the plots of H_{mid}/L vs. $\Delta W/L$ in Fig. 8.6. Beyond this second critical point, the midpoint height of the plate remains almost unchanged with normalized shear. Representative configurations from experiments and simulations are provided in Fig. 8.1.

We next turn to another pre-stressed state of elastic plate at a lower value of the longitudinal displacement with $\Delta L/L = 1/4$. We again focus on the critical points for the transition from a rod-like to a plate-like behavior of the elastic plates. In Fig. 8.7, we present the evolution of the normalized midpoint height, H_{mid}/L, with the normalized transverse shear, $\Delta W/L$, at different values of length to width ratio, $W/L \in \{1/20, 1/12, 1/6, 1/2\}$. The first and second critical points for the narrow strip ($W/L = 1/20$, Fig. 8.7(a)) are $\Delta W_1/L = 0.23$ and $\Delta W_2/L = 0.37$, which are lower than the case of $\Delta L/L = 1/2$. As the width of the plate is increases in Figs. 8.7(b-d), the rod model starts to deviate from the plate simulation and experiments. The critical shear distance at which the plate transitions from U to US decreases by $15.8\%, 29.1\%$, and 65.6% (compared with the case of $W/L = 1/20$) as the width increases ($W/L \in \{1/12, 1/6, 1/2\}$). A similar trend is noted for the boundaries between US pattern and S pattern. Again, excellent agreement between plate simulations and experimental data is found in all cases, while the rod model overestimates the critical points ($\Delta W_1/L$ and $\Delta W_2/L$) when the plate are not narrow enough.

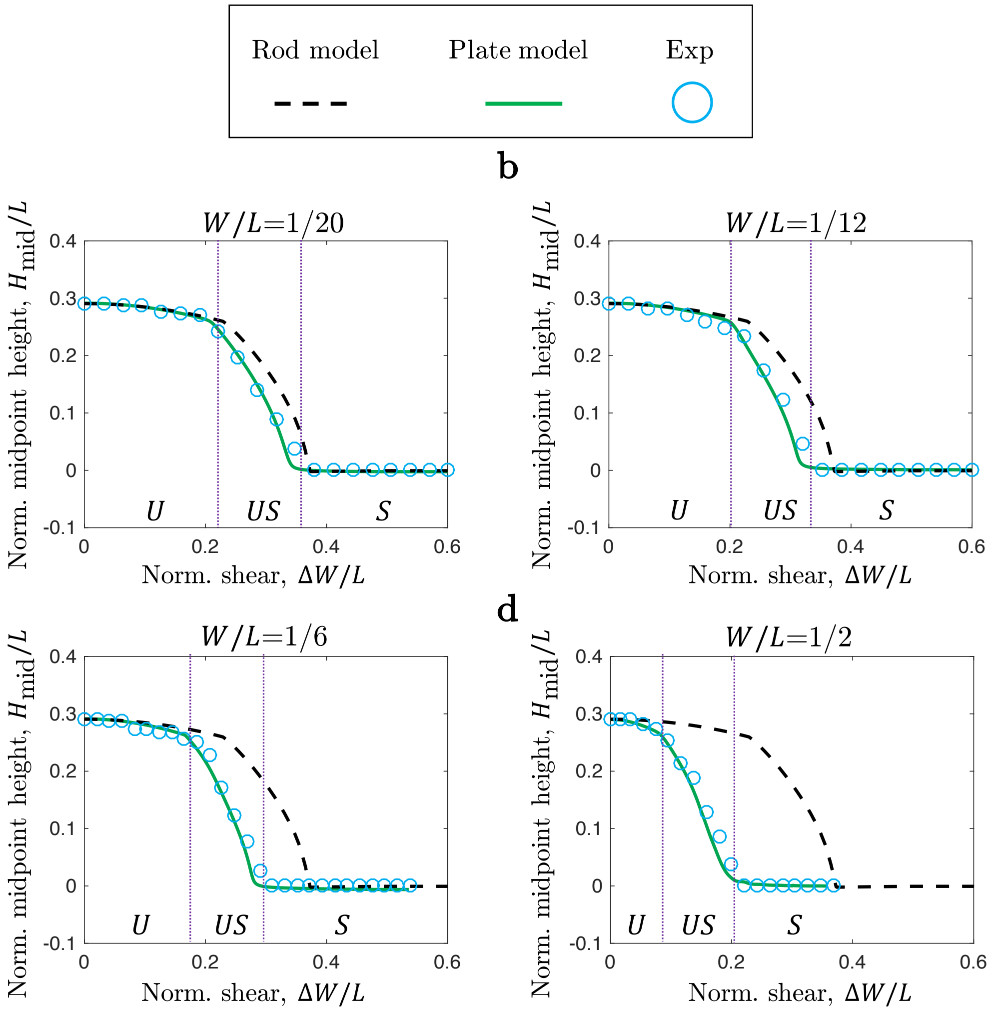

Figure 8.7: Relations between normalized midpoint height, H_{mid}/L, and normalized transverse shear, $\Delta W/L$, for plate with different width, $W/L \in \{1/20, 1/12, 1/6, 1/2\}$. The pre-compressed distance is $\Delta L/L = 1/4$.

Exploiting the efficiency and robustness of DDG-based simulators, in Fig. 8.8, we perform a two dimensional parameter sweep, by varying both length to width ratio, $L/W \in [2, 20]$, and normalized transverse shear, $\Delta W/L \in [0, \Delta W_{\mathrm{max}}/L]$, to show the phase diagrams of the elastic plates with two specific pre-buckled configurations, $\Delta L/L = 1/2$ (in Fig. 8.8(a)) and $\Delta L/L = 1/4$ (in Fig. 8.8(b)). Both first and second thresholds show an increasing trend as the width of the plate decreases. The boundaries in the phase diagram show good agreement between plate model and experiment. However, the predictions from anisotropic rod model remain unchanged and the phase boundaries from rod model in Fig. 8.8 are horizontal lines. Rod-based model is no longer reliable as the width of the

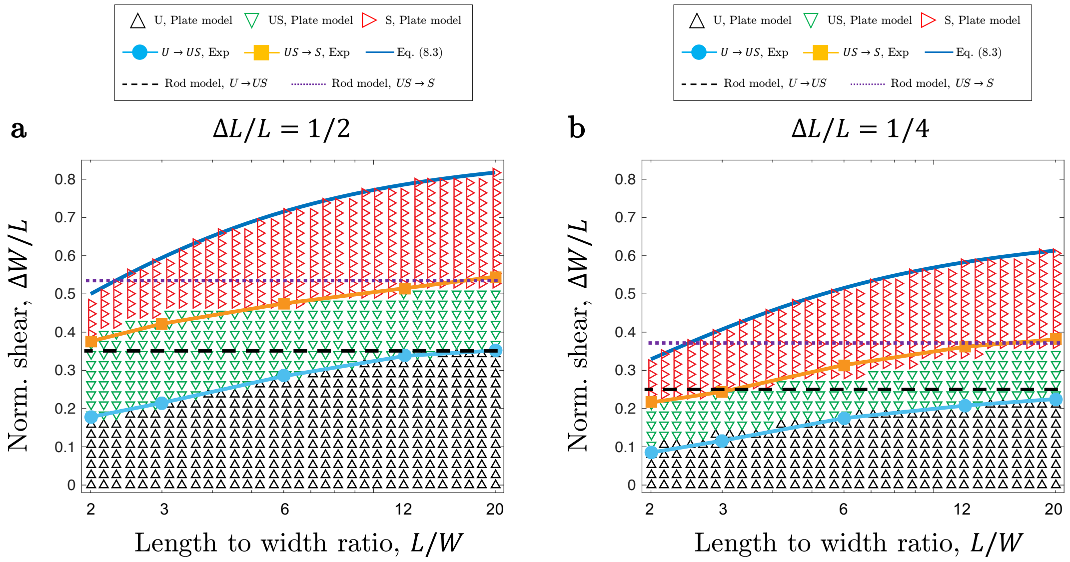

Figure 8.8: Phase diagrams of shear-induced deformed configurations in pre-buckled plates. (a) $\Delta L/L = 1/2$ and (b) $\Delta L/L = 1/4$.

plate grows, which emphasizes the width effect of elastic strip under transverse shear and the need of two dimensional plate approach. Also, as expected, the threshold boundaries (along $\Delta W/L$) in $\Delta L/L = 1/4$ are lower than the ones in $\Delta L/L = 1/2$.

8.4.4 Bifurcations in US and S Patterns

We found bifurcation phenomena when the strip translations from U to US configuration in both experiment and simulation side. After the supercritical pitchfork point, $\Delta W_1/L$, the unstable U configuration would transfer into two symmetric US patterns: $US+$ and $US-$. One can easily switch to another with a small transverse perturbation. Note that the $US+$ and $US-$ are mirror symmetric, e.g., $US-$ pattern is the same as $US+$ looked at from the other side. As the transverse shear increases, $US+$ would translation to $S+$ pattern, and the same is true for $US-$ and $S-$ configurations, as shown in Fig. 8.9.

8.4.5 Convergence Study

Our discrete models show good convergence with space discretization, i.e., number of nodes. In Fig. 8.10(a), we plot the normalized height of strip midpoint as a function of normalized transverse displacement for discrete anisotropic rod model; the final results

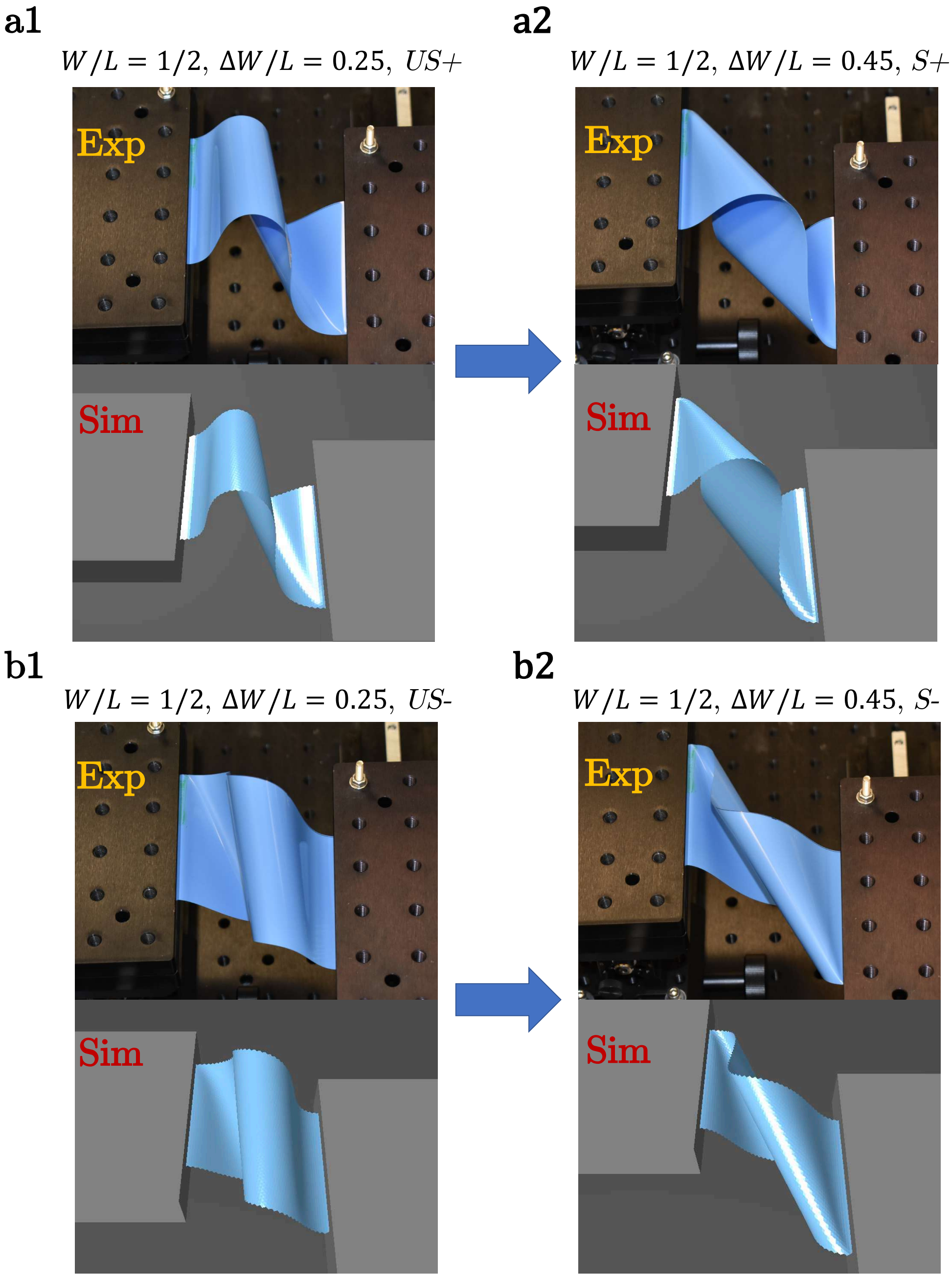

$W/L = 1/2$, $\Delta W/L = 0.25$, $US+$

$W/L = 1/2$, $\Delta W/L = 0.45$, $S+$

$W/L = 1/2$, $\Delta W/L = 0.25$, US-

$W/L = 1/2$, $\Delta W/L = 0.45$, S-

Figure 8.9: Bifurcations in US patterns and S patterns from desktop experiments and discrete plate simulations. (a1) $US+$ configuration; (a2) $S+$ configuration; (b1) $US-$ configuration; (b2) $S-$ configuration.

remain unchanged as the number of nodes, M, varies from 50 to 200. We show a similar plot in In Fig. 8.10(b) to demonstrate that the mechanical response of elastic plate ($\Delta L/L = 1/2$, $W/L = 1/6$) remains unchanged when the mesh number N_{mesh} in DEP varies from 896 to 3596. As we are focusing on the quasistatic response of elastic struc-

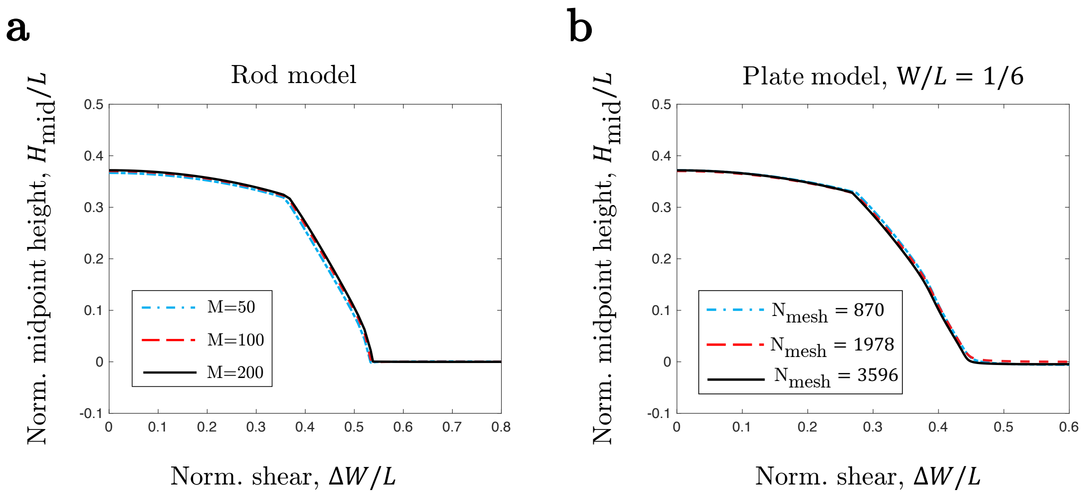

Figure 8.10: Convergence study for (a) rod model and (b) plate model.

tures, we omit the convergence with time discretization here.

8.4.6 Effect of Poisson Ratio

We demonstrate the effect of Poisson ratio on the anisotropic rod model is negligible [136, 135]. In Fig. 8.11, we plot the normalized midpoint height as a function of normalized transverse shear with a pre-stressed distance, $\Delta L/L = 1/2$, from the anisotropic rod model. We find negligible variation as Poisson ratio changes from 0.0 to 0.5. In the current study, we used $\nu = 0.0$.

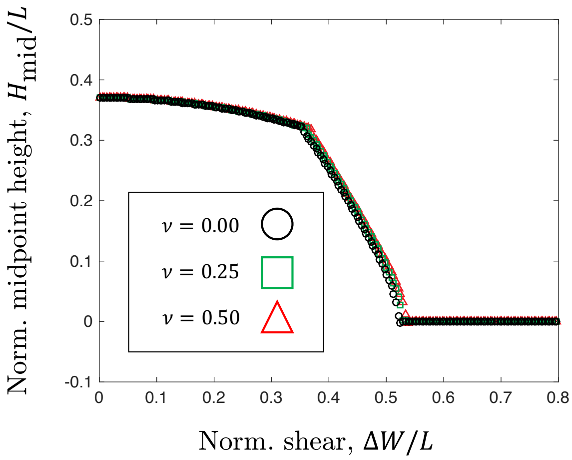

Figure 8.11: Effect of Poisson ratio in anisotropic rod simulation.

8.4.7 Issues in the Existing Ribbon Model

In this section, we discuss the issues in the existing one dimensional developable ribbon model. First, the original Kirchhoff elastic energy of a naturally straight inextensible rod, E^{rod}, is given by [1]

$$E^{\text{rod}} = \int_0^L \left[YI_1(\kappa^{(1)})^2 + YI_2(\kappa^{(2)})^2 + GJ(\tau)^2 \right] ds, \tag{8.4}$$

where $\kappa^{(1)}$ and $\kappa^{(2)}$ are the bending curvatures, τ is the twisting curvature, $YI_1 = Y\frac{1}{12}bW^3$ and $YI_2 = Y\frac{1}{12}Wb^3$ are the bending moduli of the two principal directions of the cross section, and $GJ = \frac{Y}{2(1+\nu)}\frac{1}{3}Wb^3$ is the twist modulus. Note that we can easily replace $GJ = 2YI_2$ when $\nu = 0$. For the narrow strip with anisotropic cross section, e.g., $YI_1 \gg YI_2$, the in-plane curvature is the geodesic curvature and remains unchanged, $\kappa^{(1)} \equiv \bar{\kappa}^{(1)}$, which is the case of the anisotropic rod model discussed in this chapter.

The one dimensional strip model proposed by van der Heijden and Starostin [155] treated the ribbon structure as a developable surface and considered its width effect,

$$E_1^{\text{ribbon}} = \int_0^L Y\frac{1}{12}Wb^3 \left\{ \left[\kappa^{(2)}(1+\eta^2) \right]^2 \frac{1}{W\eta'} \log\left(\frac{1 + W\eta'/2}{1 - W\eta'/2} \right) \right\} ds, \tag{8.5}$$

where $\eta = \tau/\kappa^{(2)}$. However, the solution of Eq. (8.5) is partitioned into multiple pieces by inflection points, such that we need to manually tune the simulations for desired results (see Appendix E of Ref. [136] as a reference). Also, the $\log$ barrier energy function in Eq. (8.5) would be infinite at the conical zones, resulting numerical singularities in discrete model.

In Ref. [156], Moore and Healey introduced an elliptic regularization parameter to the energy functional (see Eq. (89) of their original paper),

$$E_2^{\text{ribbon}} = \int_0^L Y\frac{1}{12}Wb^3 \left\{ \left[\kappa^{(2)}(1+\eta^2) \right]^2 \frac{1}{W\eta'} \log\left(\frac{1 + W\eta'/2}{1 - W\eta'/2} \right) \right\} ds + \int_0^L \frac{1}{2}K(\eta')^2 ds \tag{8.6}$$

to avoid the numerical difficulties, where the stiffness K performs like a stiff spring to prevent η' from going beyond a threshold so that the $\log$ term in Eq. (8.5) is far away from zero. The final results, obviously, would be sensitive to the choice of regularized parameter K [156]. If K is small, the simulator would still meet numerical issues; if K is large, the results would not be acceptable.

For the developable ribbon with small width, $L \gg W$, the Wunderlich's energy functional reduces to Sadowsky's limit [21],

$$E_3^{\text{ribbon}} = \int_0^L YI_2 \left[(\kappa^{(2)})^2 + 2(\tau)^2 + \frac{(\tau)^4}{(\kappa^{(2)})^2} \right] ds. \tag{8.7}$$

To avoid the numerical issues, a regularized parameter ζ is introduced in Eq. (8.7)

$$E_4^{\text{ribbon}} = \int_0^L \left[YI_1(\kappa^{(1)})^2 + YI_2(\kappa^{(2)})^2 + GJ(\tau)^2 \right] ds + \int_0^L YI_2 \left[\frac{(\tau)^4}{1/\zeta^2 + (\kappa^{(2)})^2} \right] ds, \tag{8.8}$$

We first implement the Sadowsky model in a discrete format by simply replacing the bending and twisting of a rod in Eq. (8.4) by the Sadowsky's energy in Eq. (8.8)). As expected, we found the final results show no variation with ζ when ζ is large enough, and we set ζ to be 10^8. In Fig. 8.12, we plot the numerical results from anisotropic rod model (Eq. (8.4)), plate simulation, and Sadowsky model (Eq. (8.8)) at different values of normalized width, W/L (cf. Fig. 8.6). Here, the pre-stressed distance is $\Delta L/L = 1/2$. In our simulations, we start with $\Delta W/L = 0$ and slowly increase the shear displacement. This “Direct-Sadowsky" model fails to capture the supercritical pitchfork point at $\Delta W/L = 0.36$ in Fig. 8.12(a) that was predicted by both rod model and plate simulations. This is because the Sadowsky model holds the developable surface assumption, i.e., the twisting curvature has to be zero where the bending curvature changes its direction. This assumption is too “rigid" to transition from U to US pattern. To overcome the energy barrier in the Sadowsky model at the inflection points, we implement the “DAR-Sadowsky" simulation, where the initial configuration of the structure is obtained from rod-based simulations and the Sadowsky model is then used to find the equilibrium configuration. Referring to Fig. 8.12, the DAR-Sadowsky model can reasonably capture the experimental observations.

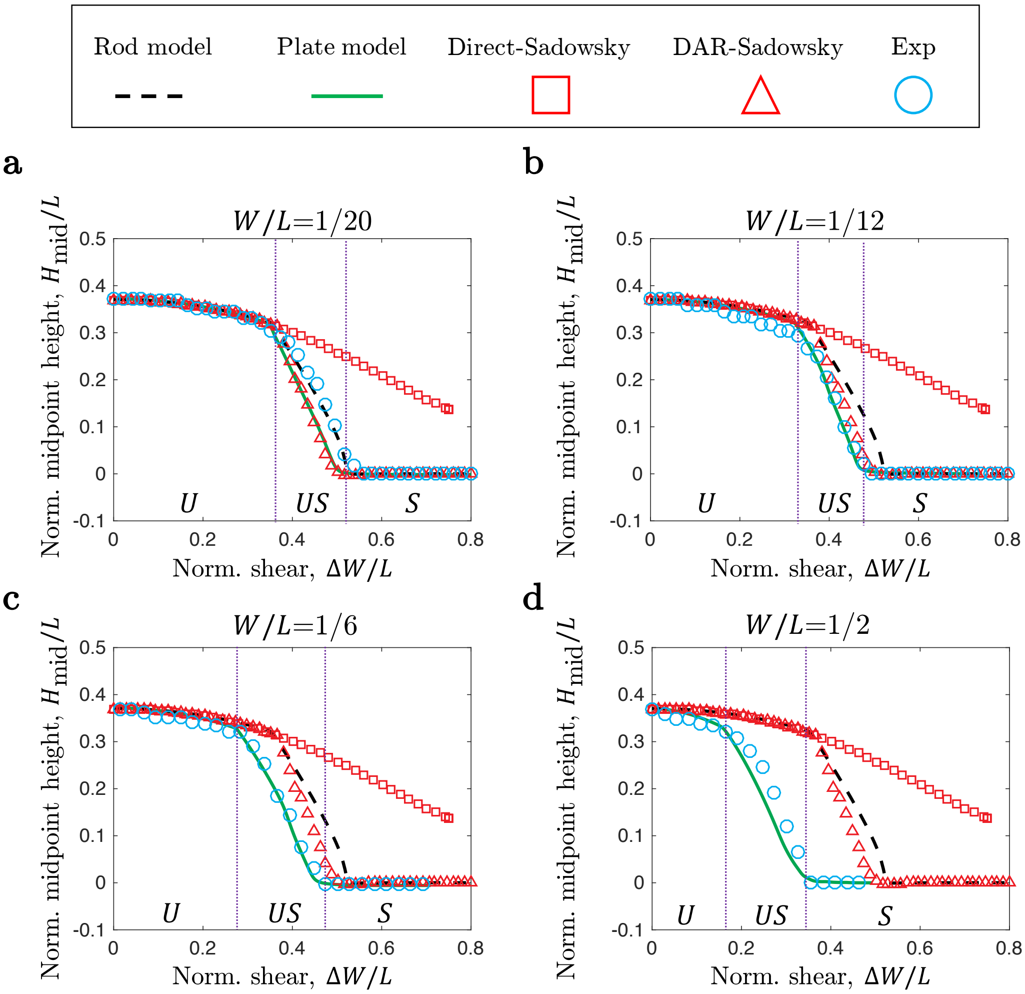

Figure 8.12: Normalized midpoint height, H_{mid}/L as a function of normalized transverse shear, $\Delta W/L$, from anisotropic rod model, plate model, and two Sadowsky models. Here the pre-compressed distance is $\Delta L/L = 1/2$.

However, unlike the plate model, it cannot capture the dependence on width.

Next, to better describe the issues at the inflection point, we plot the bending and twisting curvatures of the centerline in Fig. 8.13, from (i) DAR, (ii) Direct-Sadowsky, and (iii) DAR-Sadowsky. The curvatures predicted by rod model are smooth everywhere, while the curvatures in the Direct-Sadowsky and DAR-Sadowsky models are discontinuous at the inflection points when the bending curvature changes direction. Unsurprisingly, the number of inflection point does not change in the Direct-Sadowsky model owing to the energy barrier and the strip is always in U patterns.

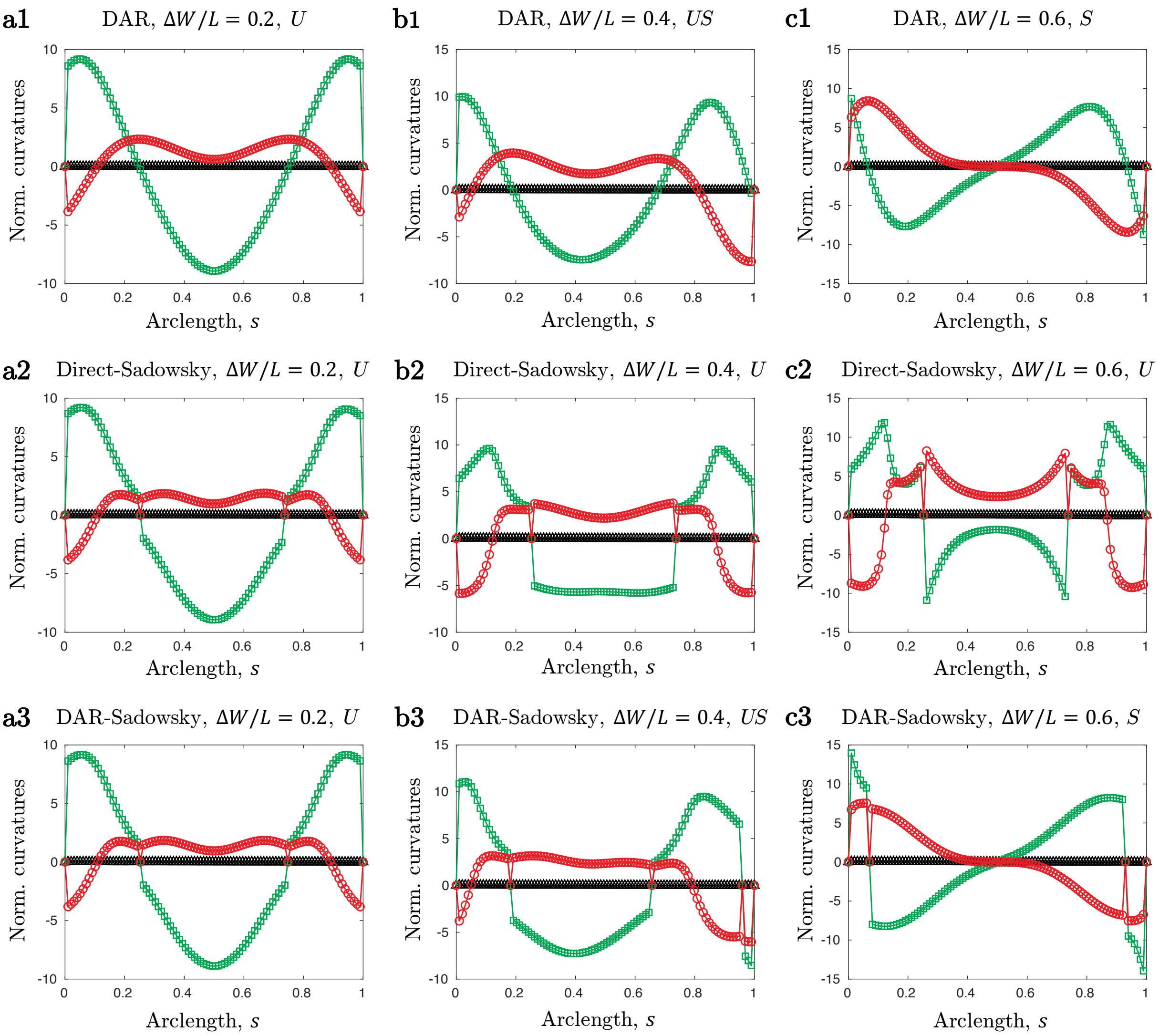

Figure 8.13: Normalized bending curvatures and twisting curvatures vary along strip arclength for (a1-c1) DAR; (a2-c2) direct-Sadowsky model; and (a3-c3) DAR-Sadowsky model. The green square is bending curvature $\kappa^{(2)}L$, the red dot is twisting curvature τL, and the black triangular is the geodesic (in-plane) curvature $\kappa^{(1)}$ L.

Finally, we turn to the plate model to better understand the curvatures at the inflection points. In Fig. 8.14, we plot the centerline curvatures along the arclength of a narrow plate ($W/L = 1/20$), with different thickness: (1) $L/b = 300$, (2) $L/b = 600$, and (c) $L/b = 1200$. At a relatively large plate thickness ($L/b = 300$), the twisting curvatures are smooth at the inflection points. As the plate becomes thinner, the twisting curvatures show hints of discontinuity when the bending curvature changes the direction. Keep in

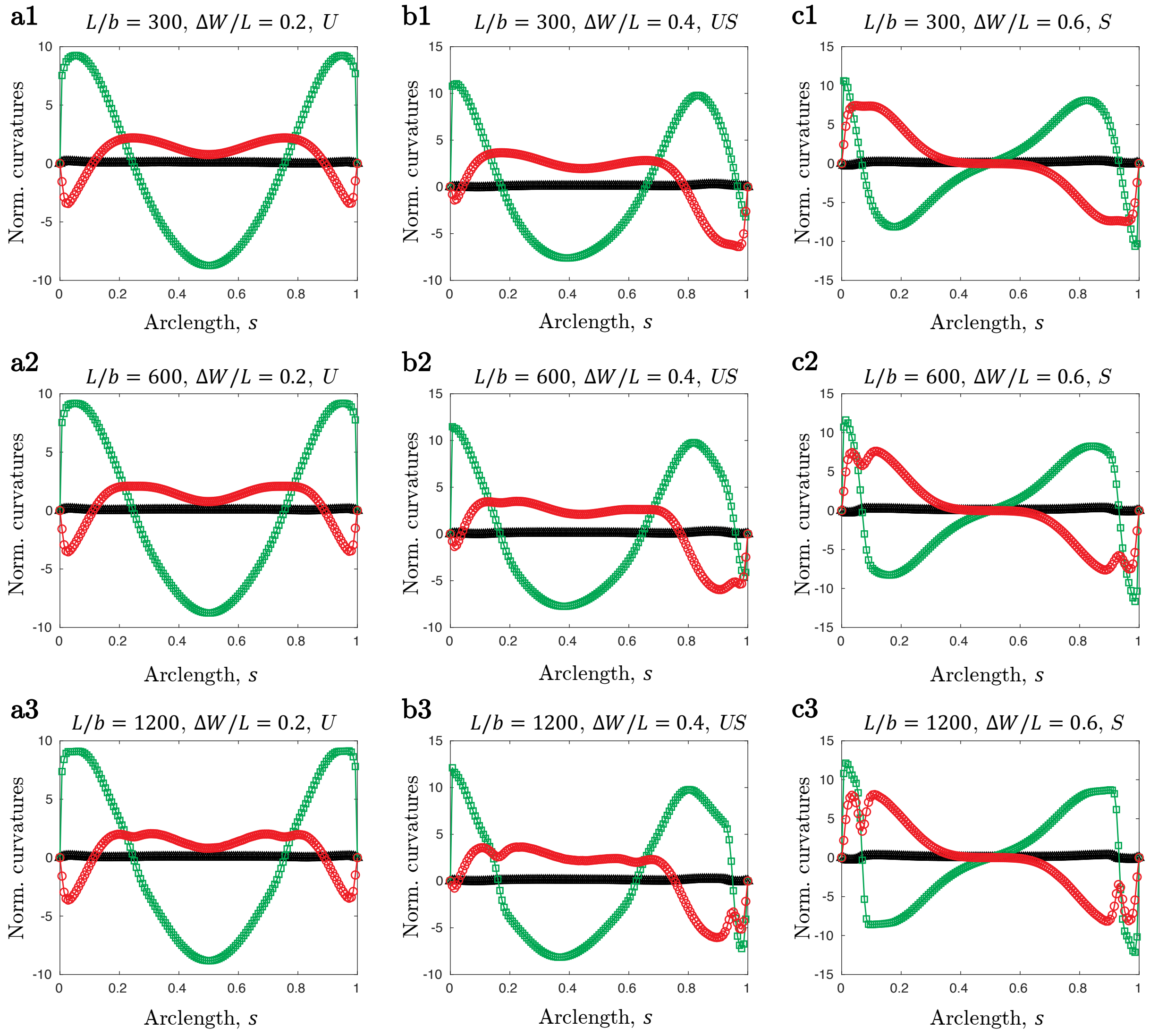

Figure 8.14: Normalized bending curvatures and twisting curvatures vary along narrow plate centerline for different thickness $L/b \in \{300, 600, 1200\}$. Here the width to length ratio is $W/L = 1/20$. The green square is bending curvature $\kappa^{(2)}L$, the red dot is twisting curvature τL, and the black triangular is the geodesic (in-plane) curvature $\kappa^{(1)}L$.

mind that stretching is energetically more expensive as the thickness decreases and the surface becomes more and more developable.

This effect of thickness is more obvious in Fig. 8.15 that shows the same data as Fig. 8.14 but for a wider plate with $W/L = 1/6$. Here, the twisting curvatures at the inflection points become closer and closer to zero as the plate thickness decreases and

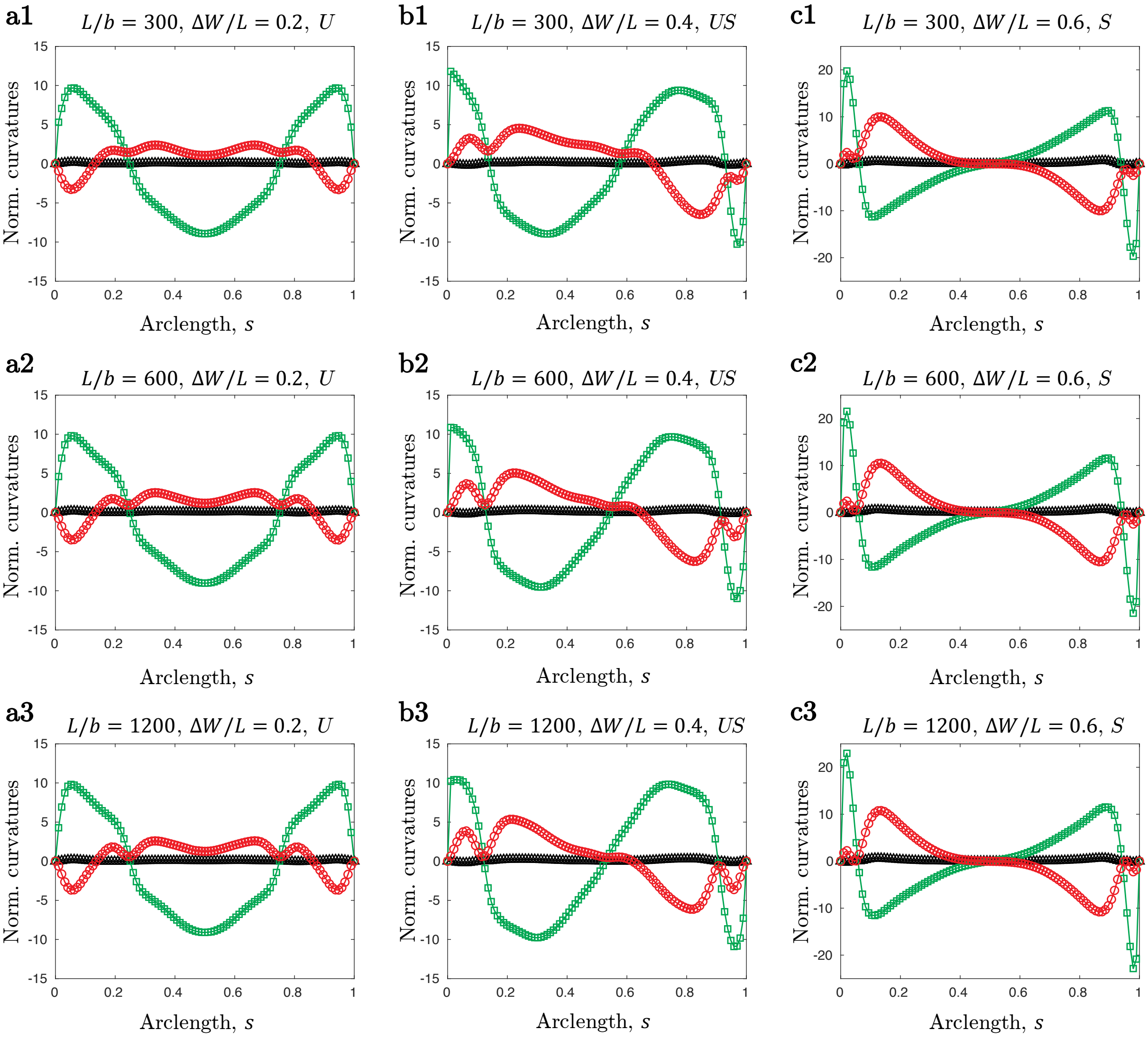

Figure 8.15: Normalized bending curvatures and twisting curvatures vary along wide plate centerline for different thickness $L/b \in \{300, 600, 1200\}$. Here the width to length ratio is $W/L = 1/6$. The green square is bending curvature $\kappa^{(2)}L$, the red dot is twisting curvature τL, and the black triangular is the geodesic (in-plane) curvature $\kappa^{(1)}L$.

the surfaces become more and more inextensible. Qualitatively speaking, the extreme case with zero thickness is the assumption behind the Sadowsky and Wunderlich models. For an ideal ribbon model (Sadowsky and Wunderlich models) with developable assumption, the stretching is totally forbidden, such that the curvature are discontinuous and, in our numerical framework, such model cannot capture the supercritical pitchfork. On the other hand, the two dimensional Föppl-von Kármán (FvK) plate model allows a small but nonzero stretching at the inflection points, and successfully captures the transition between U and US patterns.

8.4.8 Towards a 1D Extensible Ribbon Model

Recently, to avoid numerical singularity and allow the stretching of strip mid-surface during the bending and twisting deformations, Sano and Wada [135] introduced a width-depended regularized parameter to the denominator of Eq. (8.7) and set $\zeta^2 = (1 - \nu)W^4/60b^2$, where W is the width of the cross section, b is its thickness, and ν is the Poisson ratio, which has insensitive influence on structural response [135]. The formulation has been used in a study on the twist-induced snapping in a bent elastic rod and ribbon [135]. However, this one dimensional energy formulation fails to capture the width effect of elastic strip addressed in our study. In Ref. [135], they considered a structure with $L \gg W \sim b$, e.g., the longitudinal dimension is much larger than the width and thickness, and cross section is “weakly" anisotropic, from circular to elliptical then to the ribbon with small width to thickness ratio.

Even this model is not general, it can bridge the gap between anisotropic rod model and Sadowsky ribbon model. In Fig. 8.16, we plot the normalized bending and twisting curvatures along strip arc-length from rod model, extensible ribbon model, and Sadowsky model. Here, the width to length ratio is fixed as $W/L = 1/20$ and transverse shear is set to be $\Delta W/L = 0.2$; we vary the thickness b to bridge the gap between the anisotropic rod model and Sadowsky ribbon model. Extensible ribbon model with a cross-section related regularized parameter can successfully bridge the gap between the rod model and Sadowsky ribbon model. Overall, the key governing parameter is the ratio between L/W and W/b. On the one hand, if L/W is predominant than W/b, the structure is slender and would perform like an anisotropic rod, e.g., Eq. (8.8) reaches to Eq. (8.4); on the other hand, if W/b is predominant than L/W, the structure would look like a developable surface and Eq. (8.8) will converge to Eq. (8.7).

We next demonstrate that the deformation of an elastic strip with finite width can be reasonably represented only by the deformation of its centerline, e.g., the bending,

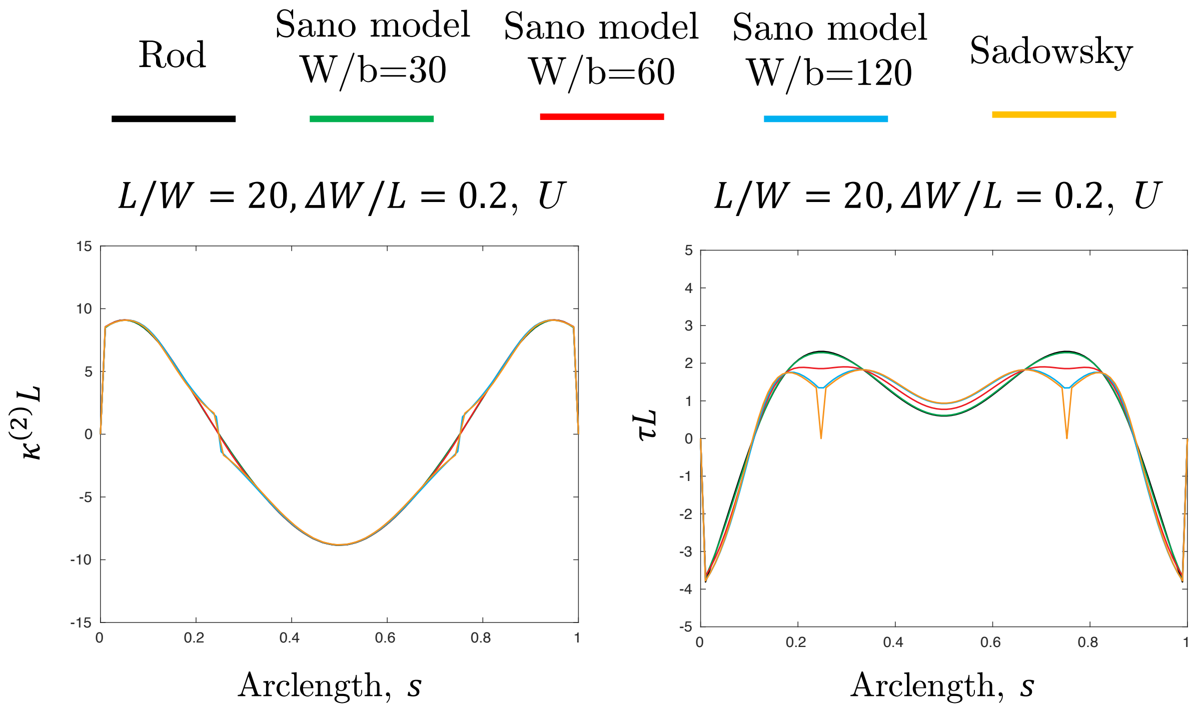

Figure 8.16: Normalized bending curvatures and twisting curvatures vary along strip arclength for rod model, extensible ribbon model, and Sadowsky model.

twisting, and stretching of a single framed curve. In Fig. 8.17(a), we plot the deformed strips with different size, $W/L \in \{1/20, 1/12, 1/6, 1/3\}$, and normalized transverse shear, $\Delta W/L \in \{0.3, 0.5\}$, from plate simulation (triangular mesh). The same figure also shows the configurations of the centerline (solid red line) that best approximates the deformed shape of the strip. In the following, we compare the topology of the structure from the centerline-based approximation with the actual configuration from plate simulation.

In this centerline-based approximation, each node can be represented using its location in (s, w) space, where $s \in [0, 1]$ is the normalized arc-length parameter and $w \in [-W/2, W/2]$ denotes the position along the width. Upon dividing the centerline into a number of nodes, the k-th node on the centerline, with $s = s_k$, can be used to make an approximation for the deformed position of any node on the plate with $s = s_k$ and $w \in [-W/2, W/2]$:

$$\mathbf{x}^c_{k,w} = \mathbf{x}^p_k + w\frac{(\bar{\mathbf{m}}^k_2 + \bar{\mathbf{m}}^{k-1}_2)}{2}, \tag{8.9}$$

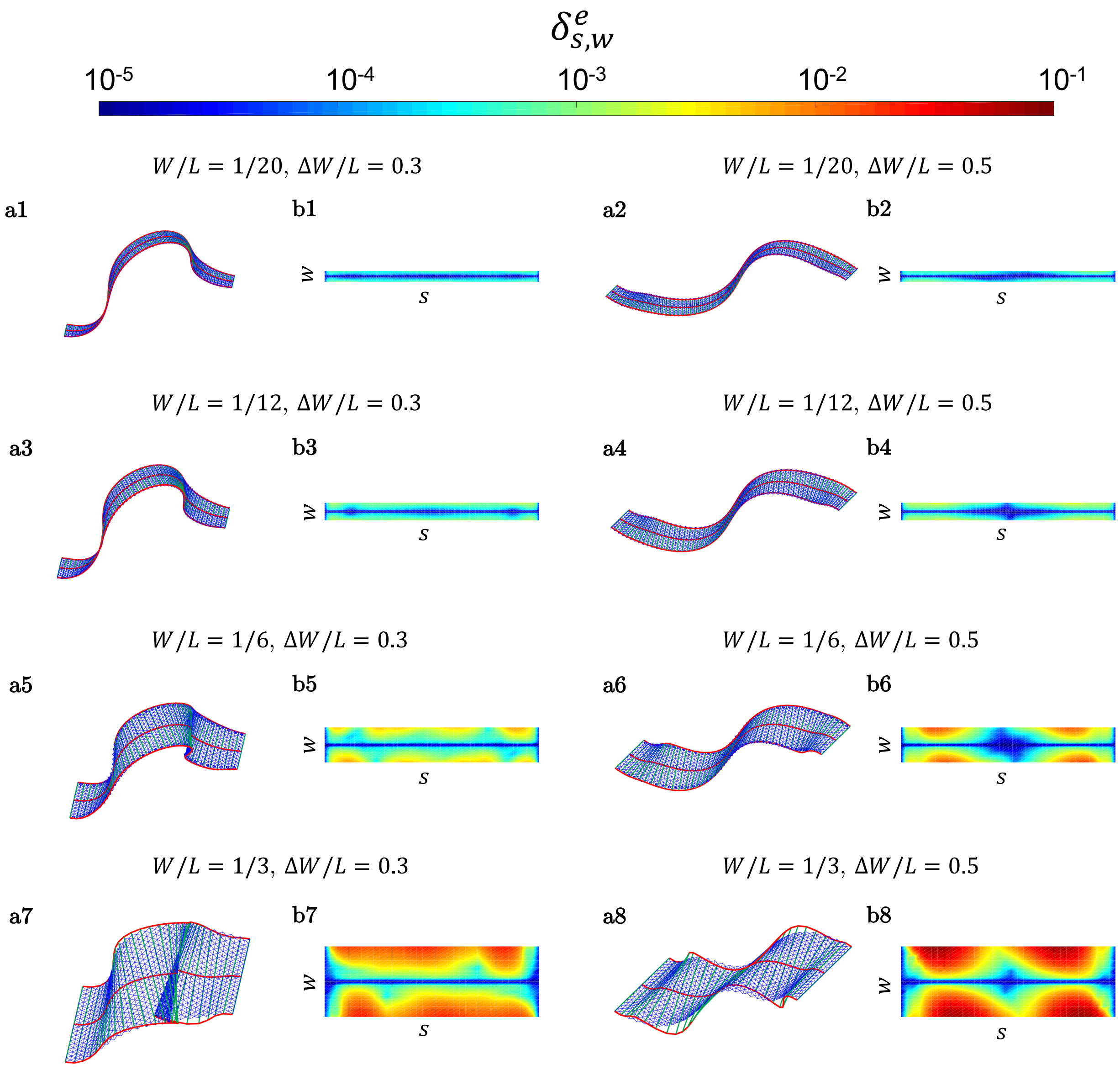

Figure 8.17: (a) Deformed configurations of plates with different length to width ratio and transverse shear evaluated from DEP simulations (blue triangular mesh) and centerline-based renderings (red lines). (b) Relative errors between plate simulations and centerline-based data.

where $\mathbf{x}^c_{k,w}$ is the location of a node in (s_k, w), $\mathbf{x}^p_k$ is the location of the k-th node on the centerline, and $\bar{\mathbf{m}}^k_2 = \bar{\mathbf{t}}^k \times \bar{\mathbf{m}}^k_1$ is the second material director on the edge vector between $s = s_{k+1}$ and $s = s_k$, $\bar{\mathbf{t}}^k$ is the tangent vector on the same edge, and $\bar{\mathbf{m}}^k_1$ is first material director, i.e., the surface normal. In other words, each node is related to the configuration of the centerline by only three curvature quantities. Here, the surface normal $\bar{\mathbf{m}}_1^k$ is obtained from the normal vector of triangular mesh on plate centerline; the second material director is then simply $\bar{\mathbf{m}}_2^k = \bar{\mathbf{t}}^k \times \bar{\mathbf{m}}_1^k$. We use an overbar to differentiate between the material frames from plate data and the ones in anisotropic rod model. In Fig. 8.17(b), we show the relative error, $\delta^e_{s,w}$, along the plate surface described by (s, w), where

$$\delta^e_{s,w} = \frac{\|\mathbf{x}^c_{k,w} - \mathbf{x}^p_{k,w}\|}{L} \tag{8.10}$$

is evaluated based on the distance between the deformed positions of the nodes obtained from the centerline-based approximation in Eq. (8.9) and the direct solution of the DEP simulation, $\mathbf{x}^p_{k,w}$. In all different cases described in Fig. 8.17, the relative error increases from the centerline ($w = 0$) towards the edge and from the clamped ends to the middle. The maximum errors occur close to the conical areas, details of conical areas can be found in Fig. 8.5. The relative error remains within the tolerance $\lesssim 2\%$ when the strips are narrow, e.g., $W/L \leq 1/6$; while a significant deviation can be observed for a wide strip undergoing large transverse shear in Fig. 8.18. In order to summarize the error from centerline-based approximation in Fig. 8.18, we show the average error, $\bar{\delta}^e = \sum^N \delta^e_{s,w}/N$ (here N is the total number of nodes in plate simulation) as a function length to width ratio, $L/W \in \{2, 3, 6, 12, 20\}$ at different values of transverse displacement, $\Delta W/L \in \{0.1, 0.3, 0.5\}$. This indicates that the centerline-based approximation is reasonable as long as $L/W > 6$ or $\Delta W/L < 0.3$.

Finally, we will discuss the research for future direction, e.g., the machine learning-assisted modeling for extensible ribbons. The 1D energy models in Eq. (8.4), Eq. (8.7), and Eq. (8.8) assumed the structural length L is much larger than its width W, such that the energy functionals can be given by the following format,

$$\hat{E} = f\left(\frac{W}{h}, \bar{\kappa}_2, \bar{\tau}\right), \tag{8.11}$$

where $\hat{E} = E/YWh$ is the normalized energy per unit length and $\bar{\kappa}_2 = \kappa^{(2)}h$ (and $\bar{\tau} = \tau h$) is the normalized bending (and twisting) curvatures. For example, the rod model in

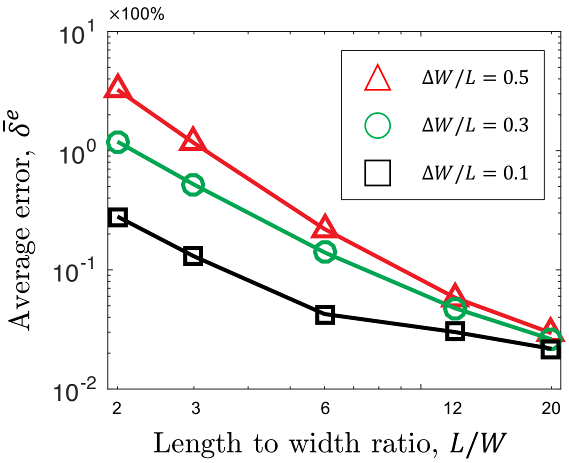

Figure 8.18: The relative errors between plate model and centerline-based data as a function plate size.

Eq. (8.4) can be rewritten into

$$\hat{E}^{\text{rod}} = \frac{1}{2}\frac{1}{12}\bar{\kappa}_2^2 + \frac{1}{2}\frac{1}{6}\bar{\tau}^2, \tag{8.12}$$

and the Possion ratio here is set to be $\nu = 0$. Due to the ratio between L/W and W/h, this type of energy functionals can bridge the gap between anisotropic rod model and developable Sadowsky ribbon model [157], as demonstrated before. However, all these 1D energy functionals fail to capture the experimental observations in Fig. 8.6 and Fig. 8.7, because the structure here is no longer slender, i.e., its length L and width W are in the same order of magnitude, rather than $L \gg W$, and, therefore, its energy density is not only related to the centerline curvature, but also related to its gradient,

$$\hat{E} = f\left(\frac{W}{h}, \bar{\kappa}_2, \bar{\tau}, \bar{\kappa}_2', \bar{\tau}', \bar{\kappa}_2'', \bar{\tau}'', ..., \bar{\kappa}_2^{(n)}, \bar{\tau}^{(n)}\right), \tag{8.13}$$

e.g., the Wunderlich model illustrated in Eq. (8.5).

Here, we want to use machine learning to fit a general 1D higher order extensible ribbon model from 2D elastic plate simulations. We first run some 2D elastic plate frameworks with arbitrary boundary conditions; next, we extract the key data from the simulations; specifically, the centerline curvatures and the energy density per unit length; finally, we want to utilize a neural network to express the relation between the 1D energy functional and the centerline curvatures, for the use of a general 1D higher order extensible ribbon model, referring to Eq. (8.13).

Unfortunately, we experience some difficulties during this machine learning-assisted modeling process. (i) We found that the energy per unit length may not be uniquely determined by the centerline curvatures. For example, the centerlines for both flat ribbon and a shallow cylindrical shell are straight lines, but we know for sure these two structures are fundamentally different. By simply running 2D plate simulation with arbitrary boundary conditions, the cross section of the strip may also deformed, such that only using the centerline data but ignoring the information along the transverse direction would not be possible [158]. (ii) For all the 1D models in Eq. (8.4), Eq. (8.7), and Eq. (8.8), we assume the geodesic curvatures $\kappa^{(1)}$ is totally constrained and always zero. However, in the 2D plate simulation, the geodesic curvature may not be ideal zero all the time, referring to Fig. 8.15, which may bring some errors and inaccuracies during the data training process. (iii) On the other side, we found it really hard to solve the energy functional with gradient-related terms by our well-established DDG-based numerical frameworks. In our discrete model, the structure is divided into multiple zig-zag lines instead of spline, and, as a result, the gradient-related information can only be computed from a finite difference method, which may not be as accurate as we expect, especially at the inflection points where curvatures change dramatically.

To deal with the issues in (i) and (ii), we may need more parameters in order to determine a unique NN-based energy functional, e.g., curvatures along the transverse direction [158]; or we can set some constraints in 2D plate simulations to ensure the strip is deformed into an expected pattern, instead of any arbitrary configurations. For example, the bending moment of inertia along the transverse direction can be sufficient large and perform like a Lagrange multiplier. For the issue (iii), we may need a higher order shape function instead of a linear straight line in traditional DER framework, such that the gradient-related terms can be directly derived in an analytical approach [159], rather than from a painstaking finite difference method.

8.5 Summary and Outlook

We studied supercritical pitchfork bifurcations of elastic plates with finite width subject to compression, shear, and symmetric clamping. For this purpose, two discrete different geometry (DDG)-based numerical frameworks – one dimensional Discrete Anisotropic Rods (DAR) model and two dimensional Discrete Elastic Plates (DEP) framework – were introduced in the current work to systematically study the width effect of pre-buckled plates under lateral end translations. We found that, the one dimensional Kirchhoff equations for perfectly anisotropic rods serve as a good guide to the behavior of narrow plates, while fails to give the accurate predictions as the width increases. The two dimensional approach, on the other hand, matches well with experimental observations for both narrow strips and wide plates. The critical points, as well as maximum transverse translations, showed a decreasing trend as the strip goes from narrow to wide; this raised the need for a two dimensional approach, instead of a one-dimensional Kirchhoff rod model, for investigation of elastic strips. We hope our findings can inspire the design of advanced structural systems and functional metamaterials, e.g., provide guidelines to avoid the instability in engineering settings. The limitations in existing ribbon models that often fail at the inflection points or necessitate choice of regularization parameters can be avoided by the presented two dimensional approach. Exploiting the efficiency and robustness of DDG-based numerical simulator, it would also be interesting to find a data-driven approach for the simulation of ribbon with undevelopable surface, i.e., using the numerical data from the general two dimensional plate model to train a neural network as a one-dimensional energy model for simulation of ribbon-like structures. We also discussed in details the current challenges and the future research directions for machine learning-assisted modeling in 1D extensible ribbons.

CHAPTER 9

Conclusion

We have presented investigations into several representative systems that involve the mechanics of slender structures and dynamics of soft robots. Compared with the traditional numerical methods in solid mechanics community that mainly focus on the linear regime in deformation, we use several cutting-edge computational tools ported from computer graphics for a geometrically nonlinear description of slender objects.

In Ch. 2, we studied the time marching scheme in Discrete Elastic Rods (DER) method. Traditional DER method considered a first order implicit Euler method for time interaction. We found that this numerical scheme would experience artificial energy dissipation during a long time period. We, therefore, used a second order symplectic Newmark-Beta method to overcome this numerical issue. The modified framework showed a better convergence with time step size, especially when the damping force is not included in the dynamic system. This extension can now allow DER to seamlessly capture inertia-dominated dynamic processes, e.g., dynamic process in soft robotic system.

In Ch. 3, we built a numerical framework to study the dynamics of articulated articulated soft robots. Our numerical simulation incorporates an implicit treatment of the elasticity of the limbs, structural inertia, elastic/inelastic collision between a soft body and rigid surface, and unilateral contact and Coulombic friction with an uneven surface. The final simulator can still run faster than real-time on a single thread of desktop processor In order to examine the accuracy and the robustness of our framework, locomotion experiments were performed on flat, inclined/declined, and wavy/undulating surfaces. In all cases, we found reasonable quantitative agreement between experiments and simulations, suggesting that our discrete approach can represent a promising step toward the ultimate goal of a computational framework for soft robotics engineering. A simply rolling ribbon and a soft jumper robot were later explored in the current study.

In Ch. 4, we started from the classical planar rod theory, with the consideration of a naive fluid-structure interaction model, for the use of the swimming simulation in soft underwater robots. A seastar-inspired soft robot was chosen as a demonstration. This soft swimming robot can cover a prescribed nonlinear trajectory by actuating its limbs through a specific sequence. The swimming efficiency of different actuating modes was also explored here. Moreover, the presented numerical framework was able to perform real-time simulations, which can be potentially used to generate optimal locomotion gaits that maximize range for a prescribed energy input.

In Ch. 5, we were motivated by a micron-sized system: locomotion of single flagellar bacteria. A flagella-inspired soft robot swimming in a viscous fluid was numerically investigated. Our discrete model incorporated three components: (i) Discrete Elastic Rods (DER) method to account for the elasticity of soft filament, (ii) Lighthill's Slender Body Theory (LSBT) for the long term hydrodynamic flow by helical flagellum, and (iii) Higdon's model for the hydrodynamics from spherical head. We found this simple uni-flagellar propulsor can follow a linear path when its angular velocity was lower than the threshold; however, a complex nonlinear trajectory was observed when its flagellum was spanning at a higher rate, during which the helical filament underwent buckling instability when interacting with viscous fluid. We then proposed a data-driven approach to develop a control algorithm such that our flagella-inspired robot can follow a prescribed trajectory only by changing its rotation frequency. Our results indicated that bacteria can utilize the structural instability to precisely control their swimming direction.

In Ch. 6, we numerically studied the bundling behavior between two helical rods rotating side-by-side in a viscous fluid. Three components were considered in our simulations: (i) Discrete Elastic Rods (DER) method, (ii) Regularized Stokeslet Segments (RSS) method, and (iii) a contact model for the non-penetration condition between two approaching rod segments. We first studied the mechanical response of a single helical rod undergoing rotation in low Reynolds environment and compared the results against an experimentally validated fluid-structure interaction model, LSBT. Next, we found that two rotating helical rods can attract each other and become closer because of the coupling flow field generated by each other, and the crossing behavior was related to their initial distance and rotating frequency. The propulsive force, on the other hand, shows a decreasing tendency as two flagella are brought closer to one another. The influence of helical geometry on bundling behavior was later addressed by sweeping geometric parameter space, helix pitch and helix radius. Our numerical investigations can motivate a fundamental understanding of the biophysics in microorganisms, as well as support modeling, design, and control of multi-flagellated soft robots.

In Ch. 7, we programmed a DER-based numerical method to investigate the geometrically nonlinear deformations in elastic gridshells, and then directly solve the inverse form-finding problem by a contact-based algorithm. For the forward physically-based simulation, we first decomposed the net-like structure into multiple rods and cross linker, and both of them can be individually updated through the standard DER method; the non-deviation constraint between two rods at the joint area was achieved by multiple stiffed springs, which can be simulated by a Lagrange multiplier method. For the inverse problem associated with form-finding (3D to 2D), we introduced a contact-based algorithm between the elastic gridshell and a rigid 3D surface, where the rigid surface describes the target shape of the gridshell upon actuation. This technique removed the need of several forward simulations associated with conventional optimization algorithm and provides a direct solution to the inverse problem.

In Ch. 8, we combined three discrete differential geometry-based simulations and table-top experiments to systematically study the shear induced supercritical pitchfork bifurcation of a pre-buckled bands, with a focusing on its width effect. Our discrete simulations were based on three classical models: Kirchhoff rod theory, Sadowsky ribbon model, and Föppl-von Kármán (FvK) plate framework. Even though the multi-stability and bifurcation of a narrow strip can be precisely captured by a naive one dimensional rod model, it fails to match with experiments as the ribbon increases in width. A two dimensional approach using a plate model, on the other hand, accurately predicts the geometrically nonlinear deformations and the supercritical pitchfork points for plate even when the width is as large as half of the length. Surprisingly, the classical Sadowsky ribbon model failed to predict the bifurcations observed in experiments. We discussed in detailed the issues of inflection points in developable ribbon model. Our study can also provide guidelines on the choice of the appropriate structural model - rod vs. ribbon vs. plate - in simulation of thin elastic structures.

REFERENCES

[1] Basile Audoly and Yves Pomeau. *Elasticity and geometry: from hair curls to the non-linear response of shells*. Oxford University Press, 2010.

[2] Pedro M Reis. A perspective on the revival of structural (in) stability with novel opportunities for function: from buckliphobia to buckliphilia. *Journal of Applied Mechanics*, 82(11), 2015.

[3] Mohammad K Jawed, Noor K Khouri, F Da, E Grinspun, and Pedro M Reis. Propulsion and instability of a flexible helical rod rotating in a viscous fluid. *Physical review letters*, 115(16):168101, 2015.

[4] Matheus C Fernandes, Joanna Aizenberg, James C Weaver, and Katia Bertoldi. Mechanically robust lattices inspired by deep-sea glass sponges. *Nature Materials*, pages 1–5, 2020.

[5] Tian Chen, Osama R Bilal, Kristina Shea, and Chiara Daraio. Harnessing bistability for directional propulsion of soft, untethered robots. *Proceedings of the National Academy of Sciences*, 115(22):5698–5702, 2018.

[6] Carmel Majidi. Soft robotics: a perspective-current trends and prospects for the future. *Soft Robotics*, 1(1):5–11, 2014.

[7] Christian Duriez. Control of elastic soft robots based on real-time finite element method. In *2013 IEEE International Conference on Robotics and Automation*, pages 3982–3987. IEEE, 2013.

[8] Jonathan Hiller and Hod Lipson. Dynamic simulation of soft multimaterial 3d-printed objects. *Soft robotics*, 1(1):88–101, 2014.

[9] Edward M Purcell. The efficiency of propulsion by a rotating flagellum. *Proceedings of the National Academy of Sciences*, 94(21):11307–11311, 1997.

[10] Robert M Macnab and May Kihara Ornston. Normal-to-curly flagellar transitions and their role in bacterial tumbling. stabilization of an alternative quaternary structure by mechanical force. *Journal of molecular biology*, 112(1):1–30, 1977.

[11] Kwangmin Son, Jeffrey S Guasto, and Roman Stocker. Bacteria can exploit a flagellar buckling instability to change direction. *Nature physics*, 9(8):494, 2013.

[12] Wanho Lee, Yongsam Kim, Boyce E Griffith, and Sookkyung Lim. Bacterial flagellar bundling and unbundling via polymorphic transformations. *Physical Review E*, 98(5):052405, 2018.

[13] Reinhard Vogel and Holger Stark. Motor-driven bacterial flagella and buckling instabilities. *The European Physical Journal E*, 35(2):15, 2012.

[14] Diego Lopez and Eric Lauga. Dynamics of swimming bacteria at complex interfaces. *Physics of Fluids*, 26(7):400–412, 2014.

[15] James Lighthill. Flagellar hydrodynamics. *SIAM review*, 18(2):161–230, 1976.

[16] Ricardo Cortez. Regularized stokeslet segments. *Journal of Computational Physics*, 375:783–796, 2018.

[17] Changyeob Baek, Andrew O Sageman-Furnas, Mohammad K Jawed, and Pedro M Reis. Form finding in elastic gridshells. *Proceedings of the National Academy of Sciences*, 115(1):75–80, 2018.

[18] Changyeob Baek and Pedro M Reis. Rigidity of hemispherical elastic gridshells under point load indentation. *Journal of the Mechanics and Physics of Solids*, 124:411–426, 2019.

[19] Marcelo A Dias and Basile Audoly. Wunderlich, meet Kirchhoff: A general and unified description of elastic ribbons and thin rods. *Journal of Elasticity*, 119(1-2):49–66, 2015.

[20] Gustav Kirchhoff. Ueber das gleichgewicht und die bewegung eines unendlich dünnen elastischen stabes. *Journal für die reine und angewandte Mathematik*, 1859(56):285–313, 1859.

[21] Michael Sadowsky. *Ein elementarer Beweis für die Existenz eines abwickelbaren Möbiusschen Bandes und Zurückführung des geometrischen Problems auf ein Variationsproblem*. 1930.

[22] Walter Wunderlich. Über ein abwickelbares möbiusband. *Monatshefte für Mathematik*, 66(3):276–289, 1962.

[23] August Föppl. *Vorlesungen über technische Mechanik*, volume 6. BG Teubner, 1910.

[24] Th V Kármán. Festigkeitsprobleme im maschinenbau. In *Mechanik*, pages 311–385. Springer, 1907.

[25] Leonhard Euler. *Methodus inveniendi lineas curvas maximi minimive proprietate gaudentes sive solutio problematis isoperimetrici latissimo sensu accepti*, volume 1. Springer Science & Business Media, 1952.

[26] Eugene Cosserat and François Cosserat. *Théorie des corps déformables*. A. Hermann et fils, 1909.

[27] Miklós Bergou, Max Wardetzky, Stephen Robinson, Basile Audoly, and Eitan Grinspun. Discrete elastic rods. *ACM transactions on graphics (TOG)*, 27(3):63, 2008.

[28] Miklós Bergou, Basile Audoly, Etienne Vouga, Max Wardetzky, and Eitan Grinspun. Discrete viscous threads. In *ACM Transactions on Graphics (TOG)*, volume 29, page 116. ACM, 2010.

[29] M Khalid Jawed, Alyssa Novelia, and Oliver M O'Reilly. *A primer on the kinematics of discrete elastic rods*. Springer, 2018.

[30] Weicheng Huang and Mohammad Khalid Jawed. Newmark-beta method in discrete elastic rods algorithm to avoid energy dissipation. *Journal of Applied Mechanics*, 86(8), 2019.

[31] Eitan Grinspun, Mathieu Desbrun, Konrad Polthier, Peter Schröder, and Ari Stern. Discrete differential geometry: an applied introduction. *ACM SIGGRAPH Course*, 7:1–139, 2006.

[32] Mohammad K Jawed, Fang Da, Jungseock Joo, Eitan Grinspun, and Pedro M Reis. Coiling of elastic rods on rigid substrates. *Proceedings of the National Academy of Sciences*, 111(41):14663–14668, 2014.

[33] Xiaonan Huang, Kitty Kumar, Mohammad K Jawed, Amir M Nasab, Zisheng Ye, Wanliang Shan, and Carmel Majidi. Chasing biomimetic locomotion speeds: Creating untethered soft robots with shape memory alloy actuators. *Science Robotics*, 3(25):eaau7557, 2018.

[34] Thomas JR Hughes. *The finite element method: linear static and dynamic finite element analysis*. Courier Corporation, 2012.

[35] Desai Chen, David IW Levin, Wojciech Matusik, and Danny M Kaufman. Dynamics-aware numerical coarsening for fabrication design. *ACM Transactions on Graphics (TOG)*, 36(4):84, 2017.

[36] GD Hahn. A modified euler method for dynamic analyses. *International Journal for Numerical Methods in Engineering*, 32(5):943–955, 1991.

[37] Weicheng Huang, Xiaonan Huang, Carmel Majidi, and M Khalid Jawed. Dynamic simulation of articulated soft robots. *Nature communications*, 11(1):1–9, 2020.

[38] Robert F Shepherd, Filip Ilievski, Wonjae Choi, Stephen A Morin, Adam A Stokes, Aaron D Mazzeo, Xin Chen, Michael Wang, and George M Whitesides. Multigait soft robot. *Proc. Natl. Acad. Sci.*, 108(51):20400–20403, 2011.

[39] Sangok Seok, Cagdas Denizel Onal, Kyu-Jin Cho, Robert J Wood, Daniela Rus, and Sangbae Kim. Meshworm: a peristaltic soft robot with antagonistic nickel titanium coil actuators. *IEEE/ASME Trans. Mechatronics*, 18(5):1485–1497, 2013.

[40] Huai-Ti Lin, Gary G Leisk, and Barry Trimmer. Goqbot: a caterpillar-inspired soft-bodied rolling robot. *Bioinspir. Biomim.*, 6(2):026007, 2011.

[41] Andrew D Marchese, Cagdas D Onal, and Daniela Rus. Autonomous soft robotic fish capable of escape maneuvers using fluidic elastomer actuators. *Soft Robot.*, 1(1):75–87, 2014.

[42] Gundula Runge and Annika Raatz. A framework for the automated design and modelling of soft robotic systems. *CIRP Annals*, 66(1):9–12, 2017.

[43] Nick Cheney, Josh Bongard, and Hod Lipson. Evolving soft robots in tight spaces. In *Proceedings of the 2015 annual conference on Genetic and Evolutionary Computation*, pages 935–942. ACM, 2015.

[44] Stanislao Grazioso, Giuseppe Di Gironimo, and Bruno Siciliano. A geometrically exact model for soft continuum robots: The finite element deformation space formulation. *Soft robotics*, 2018.

[45] Federico Renda, Francesco Giorgio-Serchi, Frederic Boyer, Cecilia Laschi, Jorge Dias, and Lakmal Seneviratne. A unified multi-soft-body dynamic model for underwater soft robots. *The International Journal of Robotics Research*, 37(6):648–666, 2018.

[46] Danny M Kaufman, Rasmus Tamstorf, Breannan Smith, Jean-Marie Aubry, and Eitan Grinspun. Adaptive nonlinearity for collisions in complex rod assemblies. *ACM Transactions on Graphics (TOG)*, 33(4):123, 2014.

[47] Zhongwei Shen, Jin Huang, Wei Chen, and Hujun Bao. Geometrically exact simulation of inextensible ribbon. In *Computer Graphics Forum*, volume 34, pages 145–154. Wiley Online Library, 2015.

[48] David Baraff and Andrew Witkin. Large steps in cloth simulation. In *Proceedings of the 25th annual conference on Computer graphics and interactive techniques*, pages 43–54. ACM, 1998.

[49] Eitan Grinspun, Anil N Hirani, Mathieu Desbrun, and Peter Schröder. Discrete shells. In *Proceedings of the 2003 ACM SIGGRAPH/Eurographics symposium on Computer animation*, pages 62–67. Eurographics Association, 2003.

[50] Basile Audoly, Nicolas Clauvelin, P-T Brun, Miklós Bergou, Eitan Grinspun, and Max Wardetzky. A discrete geometric approach for simulating the dynamics of thin viscous threads. *Journal of Computational Physics*, 253:18–49, 2013.

[51] Christopher Batty, Andres Uribe, Basile Audoly, and Eitan Grinspun. Discrete viscous sheets. *ACM Transactions on Graphics (TOG)*, 31(4):113, 2012.

[52] Nathaniel N Goldberg, Xiaonan Huang, Carmel Majidi, Alyssa Novelia, Oliver M O'Reilly, Derek A Paley, and William L Scott. On planar discrete elastic rod models for the locomotion of soft robots. *Soft robotics*, 2019.

[53] PS Raux, Pedro M Reis, JWM Bush, and Christophe Clanet. Rolling ribbons. *Physical review letters*, 105(4):044301, 2010.

[54] Xiaonan Huang, Kitty Kumar, Mohammad K Jawed, Amir Mohammadi Nasab, Zisheng Ye, Wanliang Shan, and Carmel Majidi. Highly dynamic shape memory alloy actuator for fast moving soft robots. *Advanced Materials Technologies*, page 1800540, 2019.

[55] Couro Kane, Jerrold E Marsden, Michael Ortiz, and Matthew West. Variational integrators and the newmark algorithm for conservative and dissipative mechanical systems. *International Journal for Numerical Methods in Engineering*, 49(10):1295–1325, 2000.

[56] Florence Bertails-Descoubes, Florent Cadoux, Gilles Daviet, and Vincent Acary. A nonsmooth newton solver for capturing exact coulomb friction in fiber assemblies. *ACM Transactions on Graphics (TOG)*, 30(1):6, 2011.

[57] Weicheng Huang, Zachary Patterson, Carmel Majidi, and M Khalid Jawed. Modeling soft swimming robots using discrete elastic rod method. In *Bioinspired Sensing, Actuation, and Control in Underwater Soft Robotic Systems*, pages 247–259. Springer, 2021.

[58] Steven I Rich, Robert J Wood, and Carmel Majidi. Untethered soft robotics. *Nat. Electron.*, 1(2):102, 2018.

[59] Robert K Katzschmann, Andrew D Marchese, and Daniela Rus. Hydraulic autonomous soft robotic fish for 3d swimming. In *Experimental Robotics*, pages 405–420. Springer, 2016.

[60] Xiaobo Tan, Drew Kim, Nathan Usher, Dan Laboy, Joel Jackson, Azra Kapetanovic, Jason Rapai, Beniamin Sabadus, and Xin Zhou. An autonomous robotic fish for mobile sensing. In *2006 IEEE/RSJ International Conference on Intelligent Robots and Systems*, pages 5424–5429. IEEE, 2006.

[61] Tiefeng Li, Guorui Li, Yiming Liang, Tingyu Cheng, Jing Dai, Xuxu Yang, Bangyuan Liu, Zedong Zeng, Zhilong Huang, Yingwu Luo, et al. Fast-moving soft electronic fish. *Science Advances*, 3(4):e1602045, 2017.

[62] Michael D Bartlett, Navid Kazem, Matthew J Powell-Palm, Xiaonan Huang, Wenhuan Sun, Jonathan A Malen, and Carmel Majidi. High thermal conductivity in soft elastomers with elongated liquid metal inclusions. *Proceedings of the National Academy of Sciences*, 114(9):2143–2148, 2017.

[63] Jean Chenevier, David González, J Vicente Aguado, Francisco Chinesta, and Elías Cueto. Reduced-order modeling of soft robots. *PloS one*, 13(2):e0192052, 2018.

[64] Li Zhang, Jake J Abbott, Lixin Dong, Kathrin E Peyer, Bradley E Kratochvil, Haixin Zhang, Christos Bergeles, and Bradley J Nelson. Characterizing the swimming properties of artificial bacterial flagella. *Nano letters*, 9(10):3663–3667, 2009.

[65] Y Modarres-Sadeghi, MP Païdoussis, and C Semler. A nonlinear model for an extensible slender flexible cylinder subjected to axial flow. *Journal of Fluids and Structures*, 21(5-7):609–627, 2005.

[66] Monalisa Mallick, A Kumar, N Tamboli, AB Kulkarni, P Sati, V Devi, and SS Chandar. Study on drag coefficient for the flow past a cylinder. *International Journal of Civil Engineering Research*, 5(4):301–306, 2014.

[67] Xiaonan Huang, Kitty Kumar, Mohammad Jawed, Zisheng Ye, and Carmel Majidi. Soft electrically actuated quadruped (SEAQ)-integrating a flex circuit board and elastomeric limbs for versatile mobility. *IEEE Robotics and Automation Letters*, 2019.

[68] Weicheng Huang and MK Jawed. Numerical exploration on buckling instability for directional control in flagellar propulsion. *Soft matter*, 16(3):604–613, 2020.

[69] MunJu Kim, James C Bird, Annemarie J Van Parys, Kenneth S Breuer, and Thomas R Powers. A macroscopic scale model of bacterial flagellar bundling. *Proceedings of the National Academy of Sciences*, 100(26):15481–15485, 2003.

[70] Yi Man, William Page, Robert J Poole, and Eric Lauga. Bundling of elastic filaments induced by hydrodynamic interactions. *Physical Review Fluids*, 2(12):123101, 2017.

[71] Nicholas C Darnton and Howard C Berg. Force-extension measurements on bacterial flagella: triggering polymorphic transformations. *Biophysical journal*, 92(6):2230–2236, 2007.

[72] Maira A Constantino, Mehdi Jabbarzadeh, Henry C Fu, Zeli Shen, James G Fox, Freddy Haesebrouck, Sara K Linden, and Rama Bansil. Bipolar lophotrichous helicobacter suis combine extended and wrapped flagella bundles to exhibit multiple modes of motility. *Scientific reports*, 8(1):14415, 2018.

[73] Emily E Riley, Debasish Das, and Eric Lauga. Swimming of peritrichous bacteria is enabled by an elastohydrodynamic instability. *Scientific reports*, 8:10728, 2018.

[74] Imke Spöring, Vincent A Martinez, Christian Hotz, Jana Schwarz-Linek, Keara L Grady, Josué M Nava-Sedeño, Teun Vissers, Hanna M Singer, Manfred Rohde, Carole Bourquin, et al. Hook length of the bacterial flagellum is optimized for maximal stability of the flagellar bundle. *PLoS biology*, 16(9):e2006989, 2018.

[75] Jon Edd, Sébastien Payen, Boris Rubinsky, Marshall L Stoller, and Metin Sitti. Biomimetic propulsion for a swimming surgical micro-robot. In *Intelligent Robots and Systems, 2003.(IROS 2003). Proceedings. 2003 IEEE/RSJ International Conference on*, volume 3, pages 2583–2588. IEEE, 2003.

[76] Ambarish Ghosh and Peer Fischer. Controlled propulsion of artificial magnetic nanostructured propellers. *Nano letters*, 9(6):2243–2245, 2009.

[77] Kathrin E Peyer, E Siringil, Li Zhang, and Bradley J Nelson. Magnetic polymer composite artificial bacterial flagella. *Bioinspiration & biomimetics*, 9(4):046014, 2014.

[78] Yoshihito Osada, Hidenori Okuzaki, and Hirofumi Hori. A polymer gel with electrically driven motility. *Nature*, 355(6357):242, 1992.

[79] Daniel Ahmed, Thierry Baasch, Bumjin Jang, Salvador Pane, JÃijrg Dual, and Bradley J Nelson. Artificial swimmers propelled by acoustically activated flagella. *Nano letters*, 16(8):4968–4974, 2016.

[80] Murat Kaynak, Adem Ozcelik, Amir Nourhani, Paul E Lammert, Vincent H Crespi, and Tony Jun Huang. Acoustic actuation of bioinspired microswimmers. *Lab on a Chip*, 17(3):395–400, 2017.

[81] Samuel Sánchez, Lluis Soler, and Jaideep Katuri. Chemically powered micro-and nanomotors. *Angewandte Chemie International Edition*, 54(5):1414–1444, 2015.

[82] Byungkyu Kim, Deok-Ho Kim, Jaehoon Jung, and Jong-Oh Park. A biomimetic undulatory tadpole robot using ionic polymer–metal composite actuators. *Smart materials and structures*, 14(6):1579, 2005.

[83] Gustav Kirchhoff. Uber das gleichgewicht und die bewegung eines unendlich dunnen elastischen stabes. *J. reine angew. Math.*, 56:285–313, 1859.

[84] Frank TM Nguyen and Michael D Graham. Buckling instabilities and complex trajectories in a simple model of uniflagellar bacteria. *Biophysical journal*, 112(5):1010–1022, 2017.

[85] Mehdi Jabbarzadeh and Henry Chien Fu. Dynamic instability in the hook-flagellum system that triggers bacterial flicks. *Physical Review E*, 97(1):012402, 2018.

[86] Akanksha Thawani and Mahesh S Tirumkudulu. Trajectory of a model bacterium. *Journal of Fluid Mechanics*, 835:252–270, 2018.

[87] JJL Higdon. A hydrodynamic analysis of flagellar propulsion. *Journal of Fluid Mechanics*, 90(4):685–711, 1979.

[88] Howard C Berg and Robert A Anderson. Bacteria swim by rotating their flagellar filaments. *Nature*, 245(5425):380, 1973.

[89] MK Jawed and Pedro M Reis. Dynamics of a flexible helical filament rotating in a viscous fluid near a rigid boundary. *Physical Review Fluids*, 2(3):034101, 2017.

[90] Allen T Chwang and T Yao-Tsu Wu. Hydromechanics of low-reynolds-number flow. part 2. singularity method for stokes flows. *Journal of Fluid Mechanics*, 67(4):787–815, 1975.

[91] JR Blake and AT Chwang. Fundamental singularities of viscous flow. *Journal of Engineering Mathematics*, 8(1):23–29, 1974.

[92] JD Martindale, M Jabbarzadeh, and HC Fu. Choice of computational method for swimming and pumping with nonslender helical filaments at low reynolds number. *Physics of Fluids*, 28(2):021901, 2016.

[93] Mohammad K Jawed and Pedro M Reis. Deformation of a soft helical filament in an axial flow at low reynolds number. *Soft matter*, 12(6):1898–1905, 2016.

[94] Weicheng Huang and MK Jawed. Numerical simulation of bundling of helical elastic rods in a viscous fluid. *Under review*.

[95] Einar Leifson, BJ Cosenza, R Murchelano, and RC Cleverdon. Motile marine bacteria i.: Techniques, ecology, and general characteristics. *Journal of Bacteriology*, 87(3):652–666, 1964.

[96] Yunyoung Park, Yongsam Kim, William Ko, and Sookkyung Lim. Instabilities of a rotating helical rod in a viscous fluid. *Physical Review E*, 95(2):022410, 2017.

[97] CR Calladine. Construction of bacterial flagella. *Nature*, 255(5504):121, 1975.

[98] Federico Renda, Francesco Giorgio-Serchi, Frederic Boyer, Cecilia Laschi, Jorge Dias, and Lakmal Seneviratne. A multi-soft-body dynamic model for underwater soft robots. In *Robotics Research*, pages 143–160. Springer, 2018.

[99] Jonas Spillmann and Matthias Teschner. An adaptive contact model for the robust simulation of knots. In *Computer Graphics Forum*, volume 27, pages 497–506. Wiley Online Library, 2008.

[100] Byoungwon Choe, Min Gyu Choi, and Hyeong-Seok Ko. Simulating complex hair with robust collision handling. In *Proceedings of the 2005 ACM SIGGRAPH/Eurographics symposium on Computer animation*, pages 153–160. ACM, 2005.

[101] Marc Gissler, Markus Becker, and Matthias Teschner. Local constraint methods for deformable objects. In *VRIPHYS*, pages 25–32, 2006.

[102] Jonas Spillmann, Markus Becker, and Matthias Teschner. Non-iterative computation of contact forces for deformable objects. 2007.

[103] Ricardo Cortez, Lisa Fauci, and Alexei Medovikov. The method of regularized stokeslets in three dimensions: analysis, validation, and application to helical swimming. *Physics of Fluids*, 17(3):031504, 2005.

[104] Christer Ericson. *Real-time collision detection*. CRC Press, 2004.

[105] Panpan Cai, Chandrasekaran Indhumathi, Yiyu Cai, Jianmin Zheng, Yi Gong, Teng Sam Lim, and Peng Wong. Collision detection using axis aligned bounding boxes. In *Simulations, Serious Games and Their Applications*, pages 1–14. Springer, 2014.

[106] Bruce Rodenborn, Chih-Hung Chen, Harry L Swinney, Bin Liu, and HP Zhang. Propulsion of microorganisms by a helical flagellum. *Proceedings of the National Academy of Sciences*, 110(5):E338–E347, 2013.

[107] Michael Silverman and Melvin I Simon. Bacterial flagella. *Annual review of microbiology*, 31(1):397–419, 1977.

[108] Weicheng Huang, Longhui Qin, and Mohammad Khalid Jawed. Numerical method for direct solution to form-finding problem in convex gridshell. *Journal of Applied Mechanics*, 88(2), 2021.

[109] Marzieh Ghiyasinasab, Nadia Lehoux, and Sylvain Ménard. Production phases and market for timber gridshell structures: A state-of-the-art review. *BioResources*, 12(4):9538–9555, 2017.

[110] Baptiste Lefevre, Cyril Douthe, and Olivier Baverel. Buckling of elastic gridshells. *Journal of the International Association for Shell and Spatial Structures*, 56(3):153–171, 2015.

[111] Sheng Xu, Zheng Yan, Kyung-In Jang, Wen Huang, Haoran Fu, Jeonghyun Kim, Zijun Wei, Matthew Flavin, Joselle McCracken, Renhan Wang, et al. Assembly of micro/nanomaterials into complex, three-dimensional architectures by compressive buckling. *Science*, 347(6218):154–159, 2015.

[112] Kyung-In Jang, Kan Li, Ha Uk Chung, Sheng Xu, Han Na Jung, Yiyuan Yang, Jean Won Kwak, Han Hee Jung, Juwon Song, Ce Yang, et al. Self-assembled three dimensional network designs for soft electronics. *Nature communications*, 8:15894, 2017.

[113] Zheng Xu, Zhichao Fan, Haoran Fu, Yuan Liu, Yanyang Zi, Yonggang Huang, and Yihui Zhang. Optimization-based approach for the inverse design of ribbon-shaped three-dimensional structures assembled through compressive buckling. *Physical Review Applied*, 11(5):054053, 2019.

[114] Julian Panetta, MINA Konaković-Luković, Florin Isvoranu, Etienne Bouleau, and Mark Pauly. X-shells: A new class of deployable beam structures. *ACM Transactions on Graphics (TOG)*, 38(4):83, 2019.

[115] Frédéric Tayeb, J-F Caron, Olivier Baverel, and Lionel Du Peloux. Stability and robustness of a 300 m2 composite gridshell structure. *Construction and Building Materials*, 49:926–938, 2013.

[116] Yuan Liu, Xueju Wang, Yameng Xu, Zhaoguo Xue, Yi Zhang, Xin Ning, Xu Cheng, Yeguang Xue, Di Lu, Qihui Zhang, et al. Harnessing the interface mechanics of hard films and soft substrates for 3d assembly by controlled buckling. *Proceedings of the National Academy of Sciences*, 116(31):15368–15377, 2019.

[117] Xuanhe Li, Weicheng Huang, and M Khalid Jawed. A discrete differential geometry-based approach to numerical simulation of timoshenko beam. *Extreme Mechanics Letters*, page 100622, 2019.

[118] Xuanhe Li, Weicheng Huang, and M Khalid Jawed. Discrete elasto-plastic rods. *Extreme Mechanics Letters*, page 100767, 2020.

[119] Jesús Pérez, Bernhard Thomaszewski, Stelian Coros, Bernd Bickel, José A Canabal, Robert Sumner, and Miguel A Otaduy. Design and fabrication of flexible rod meshes. *ACM Transactions on Graphics (TOG)*, 34(4):138, 2015.

[120] Haoran Fu, Kewang Nan, Paul Froeter, Wen Huang, Yuan Liu, Yiqi Wang, Juntong Wang, Zheng Yan, Haiwen Luan, Xiaogang Guo, et al. Mechanically-guided deterministic assembly of 3d mesostructures assisted by residual stresses. *small*, 13(24):1700151, 2017.

[121] Jason Valentine, Shuang Zhang, Thomas Zentgraf, Erick Ulin-Avila, Dentcho A Genov, Guy Bartal, and Xiang Zhang. Three-dimensional optical metamaterial with a negative refractive index. *nature*, 455(7211):376, 2008.

[122] Pedro M Reis, Francisco López Jiménez, and Joel Marthelot. Transforming architectures inspired by origami. *Proceedings of the National Academy of Sciences*, 112(40):12234–12235, 2015.

[123] Akash Garg, Andrew O Sageman-Furnas, Bailin Deng, Yonghao Yue, Eitan Grinspun, Mark Pauly, and Max Wardetzky. Wire mesh design. *ACM Transactions on Graphics*, 33(4), 2014.

[124] Longhui Qin, Weicheng Huang, Yayun Du, Luocheng Zheng, and Mohammad Khalid Jawed. Genetic algorithm-based inverse design of elastic gridshells. *Structural and Multidisciplinary Optimization*, pages 1–17, 2020.

[125] Lina Bouhaya, Olivier Baverel, and Jean-François Caron. Mapping two-way continuous elastic grid on an imposed surface: Application to grid shells. In *Symposium of the International Association for Shell and Spatial Structures (50th. 2009. Valencia). Evolution and Trends in Design, Analysis and Construction of Shell and Spatial Structures: Proceedings*. Editorial Universitat Politècnica de València, 2010.

[126] Weicheng Huang, Yunbo Wang, Xuanhe Li, and Mohammad K Jawed. Shear induced supercritical pitchfork bifurcation of pre-buckled bands, from narrow strips to wide plates. *Journal of the Mechanics and Physics of Solids*, 145:104168, 2020.

[127] Claire Lestringant, Basile Audoly, and Dennis M Kochmann. A discrete, geometrically exact method for simulating nonlinear, elastic and inelastic beams. *Computer Methods in Applied Mechanics and Engineering*, page 112741, 2019.

[128] E Kebadze, SD Guest, and S Pellegrino. Bistable prestressed shell structures. *International Journal of Solids and Structures*, 41(11-12):2801–2820, 2004.

[129] Yoël Forterre, Jan M Skotheim, Jacques Dumais, and Lakshminarayanan Mahadevan. How the venus flytrap snaps. *Nature*, 433(7024):421, 2005.

[130] Anupam Pandey, Derek E Moulton, Dominic Vella, and Douglas P Holmes. Dynamics of snapping beams and jumping poppers. *EPL (Europhysics Letters)*, 105(2):24001, 2014.

[131] Michael Gomez, Derek E Moulton, and Dominic Vella. Critical slowing down in purely elastic âĂŸsnap-throughâĂŹinstabilities. *Nature Physics*, 13(2):142, 2017.

[132] Tomohiko G Sano and Hirofumi Wada. Snap-buckling in asymmetrically constrained elastic strips. *Physical Review E*, 97(1):013002, 2018.

[133] EL Starostin and GHM van der Heijden. Tension-induced multistability in inextensible helical ribbons. *Physical review letters*, 101(8):084301, 2008.

[134] Yasuaki Morigaki, Hirofumi Wada, and Yoshimi Tanaka. Stretching an elastic loop: Crease, helicoid, and pop out. *Physical review letters*, 117(19):198003, 2016.

[135] Tomohiko G Sano and Hirofumi Wada. Twist-induced snapping in a bent elastic rod and ribbon. *Physical Review Letters*, 122(11):114301, 2019.

[136] Tian Yu and JA Hanna. Bifurcations of buckled, clamped anisotropic rods and thin bands under lateral end translations. *Journal of the Mechanics and Physics of Solids*, 122:657–685, 2019.

[137] Yingchao Zhang, Yang Jiao, Jian Wu, Yinji Ma, and Xue Feng. Configurations evolution of a buckled ribbon in response to out-of-plane loading. *Extreme Mechanics Letters*, page 100604, 2019.

[138] Guangchao Wan, Yin Liu, Zhe Xu, Congran Jin, Lin Dong, Xiaomin Han, John XJ Zhang, and Zi Chen. Tunable bistability of a clamped elastic beam. *Extreme Mechanics Letters*, page 100603, 2019.

[139] Nakul Prabhakar Bende, Arthur A Evans, Sarah Innes-Gold, Luis A Marin, Itai Cohen, Ryan C Hayward, and Christian D Santangelo. Geometrically controlled snapping transitions in shells with curved creases. *Proceedings of the National Academy of Sciences*, 112(36):11175–11180, 2015.

[140] Marko Lavrenčič and Boštjan Brank. Simulation of shell buckling by implicit dynamics and numerically dissipative schemes. *Thin-Walled Structures*, 132:682–699, 2018.

[141] Joel Marthelot, Francisco López Jiménez, Anna Lee, John W Hutchinson, and Pedro M Reis. Buckling of a pressurized hemispherical shell subjected to a probing force. *Journal of Applied Mechanics*, 84(12), 2017.

[142] Stuart S Antman and Charles S Kenney. Large buckled states of nonlinearly elastic rods under torsion, thrust, and gravity. *Archive for rational mechanics and analysis*, 76(4):289–338, 1981.

[143] Stuart S Antman and Kathleen B Jordan. 5.âĂŤqualitative aspects of the spatial deformation of non-linearly elastic rods. §. *Proceedings of the Royal Society of Edinburgh Section A: Mathematics*, 73:85–105, 1975.

[144] S Kehrbaum and JH Maddocks. Elastic rods, rigid bodies, quaternions and the last quadrature. In *Localization And Solitary Waves In Solid Mechanics*, pages 181–200. World Scientific, 1999.

[145] Michel Nizette and Alain Goriely. Towards a classification of euler–kirchhoff filaments. *Journal of mathematical physics*, 40(6):2830–2866, 1999.

[146] Olivier Ameline, Sinan Haliyo, Xingxi Huang, and Jean AH Cognet. Classifications of ideal 3d elastica shapes at equilibrium. *Journal of Mathematical Physics*, 58(6):062902, 2017.

[147] Sachin Goyal, Noel C Perkins, and Christopher L Lee. Nonlinear dynamics and loop formation in kirchhoff rods with implications to the mechanics of dna and cables. *Journal of Computational Physics*, 209(1):371–389, 2005.

[148] EL Starostin and GHM Van Der Heijden. The shape of a möbius strip. *Nature materials*, 6(8):563, 2007.

[149] David M Kleiman, Denis F Hinz, Yoichi Takato, and Eliot Fried. Influence of material stretchability on the equilibrium shape of a möbius band. *Soft matter*, 12(16):3750–3759, 2016.

[150] Rouzbeh Ghafouri and Robijn Bruinsma. Helicoid to spiral ribbon transition. *Physical review letters*, 94(13):138101, 2005.

[151] Shahaf Armon, Hillel Aharoni, Michael Moshe, and Eran Sharon. Shape selection in chiral ribbons: from seed pods to supramolecular assemblies. *Soft matter*, 10(16):2733–2740, 2014.

[152] Thierry Savin, Natasza A Kurpios, Amy E Shyer, Patricia Florescu, Haiyi Liang, L Mahadevan, and Clifford J Tabin. On the growth and form of the gut. *Nature*, 476(7358):57, 2011.

[153] Hyunjune Sebastian Seung and David R Nelson. Defects in flexible membranes with crystalline order. *Physical Review A*, 38(2):1005, 1988.

[154] Haiyi Liang and Lakshminarayanan Mahadevan. The shape of a long leaf. *Proceedings of the National Academy of Sciences*, 106(52):22049–22054, 2009.

[155] EL Starostin and GHM van der Heijden. Equilibrium shapes with stress localisation for inextensible elastic möbius and other strips. *Journal of Elasticity*, 119(1-2):67–112, 2015.

[156] Alexander Moore and Timothy J Healey. Computation of unconstrained elastic equilibria of complete möbius bands and their stability. *arXiv preprint arXiv:1509.00147*, 2015.

[157] Basile Audoly and Sébastien Neukirch. A one-dimensional model for elastic ribbons: a little stretching makes a big difference. 2021.

[158] Matteo Brunetti, Antonino Favata, and Stefano Vidoli. Enhanced models for the nonlinear bending of planar rods: localization phenomena and multistability. *Proceedings of the Royal Society A*, 476(2242):20200455, 2020.

[159] Raphaël Charrondière, Florence Bertails-Descoubes, Sébastien Neukirch, and Victor Romero. Numerical modeling of inextensible elastic ribbons with curvature-based elements. *Computer Methods in Applied Mechanics and Engineering*, 364:112922, 2020.